Novel Approaches for Spectral Unmixing of Hyperspectral Data

by

Bhatt Jignesh Shashikant

(200921006)

A Thesis Submitted in Partial Fulfilment of the Requirements for the Degree

of

Doctor of Philosophy

in

Information and Communication Technology

to

Dhirubhai Ambani Institute of Information and Communication Technology

NOVEMBER 2014

Declaration

This is to certify that

1. the thesis comprises my original work towards the degree of Doctor of Philosophy in Information and Communication Technology at DA-IICT and has not been submitted elsewhere for a degree,
2. due acknowledgment has been made in the text to all other material used.

Signature of Student

Certificate

This is to certify that the thesis work entitled "Novel Approaches for Spectral Unmixing of Hyperspectral Data" has been carried out by Bhatt Jignesh Shashikant (200921006) for the degree of Doctor of Philosophy in Information and Communication Technology at this Institute under my supervision.

Thesis Supervisor

Prof. Manjunath V. Joshi

Acknowledgments

First and above all, I praise God, the almighty for providing me this opportunity and granting me the capability to proceed successfully. Although the work described here was performed independently, I never would have been able to complete it if not for the support of many wonderful people. I would like to offer my sincere thanks to them.

I would like to express my sincere gratitude to my supervisor Prof. Manjunath V. Joshi with whom I have learned immensely and has had a strong influence in my development as a researcher. Thank you sir for the patience you had to supervise and direct my work, and for all the hard job of guidance, fruitful discussions, and helping me throughout all the different steps of my doctoral research endeavor for the past few years. I greatly appreciate the freedom and collegial respect you have given me. As my supervisor, Prof. Joshi has constantly forced me to remain focused on achieving my goal. His observations, guidance, and comments helped me to establish the overall direction of the research and to move forward with investigation in depth. Working with Prof. Joshi has enriched my life not only in the academic sense. His achievements, his work ethics, and his keen eye for every important detail have been an inspiration throughout all the years I have worked with him.

On a broader note, I wish to acknowledge all the professors of DA-IICT who have inspired me directly or indirectly. I would like to thank faculty members V. P. Sinha, Samaresh Chatterji, Sanjay Srivastava, Suman Mitra, Mehul Raval, Asim Banerjee and Aditya Tatu who have shaped my thinking about this research direction during the thesis work. It is always nice remembering the excellent times of the lessons by Prof. V. P. Sinha, Prof. Sanjay Srivastava, Prof. Suman Mitra, and specially Prof. Mehul Raval.

I express my gratitude to Director, Prof. N. Ramrao, former Director, Prof. S.C. Sahasrabudhe, Registrar, Dean-R&D, Dean-AP, and Convener-PGC who have helped me through-out my time at DA-IICT. I would like to thank administrative and technical staff members of DA-IICT who have been kind enough to advise and help me in their respective roles. My gratitude also extend to staff of DA-IICT resource-center.

I would like to express my gratitude to Prof. Subhasis Chaudhuri (Indian Institute of Technology, Bombay), Prof. N. Padmanabhan ((formerly) Scientist G, SAC, ISRO, Ahmedabad), and Prof. M. K. Arora ((formerly) Indian Institute of Technology, Roorkee) for all his technical support, valuable input and remarks at several occasions. I thank Prof. Antonio Plaza (University of Extremadura, Spain) for generously sharing the simulated data and materials that influenced the work and resulted in publications. I wish to acknowledge Dr. M. T. Eismann (Air Force Research Laboratory, USA), Prof. Lorenzo Bruzzone (University of Trento, Italy), Dr. Bormin Huang (University of Wisconsin-Madison, USA), Prof. A. A. Nielsen (DTU Space, National Space Institute, Denmark), and Prof. Natascha Oppelt (Kiel University, Germany) for the discussion on hyperspectral remote sensing at the SPIE conference. I extend my gratitude to Prof. Jocelyn Chanussot (Grenoble Institute of Technology, France) for his help on parameter estimation. I am grateful to Prof. Jose M. Bioucas-Dias (Instituto Superior Tecnico, Portugal) for always responding to our emails and sharing his knowledge in the area of his expertise. I would like to thank anonymous reviewers of our publications and the examiners of my thesis for their constructive suggestions that have greatly improved the publications and the thesis, respectively.

I made a lot of new friends at DA-IICT, who helped me in many steps of my study. I thank all of them for everything that they did for me. Thanks to Dr. Prakash P. Gajjar (Government Polytechnic, Surat) for many fruitful discussions.

I would love to cordially express my gratitude to my mother *Gita* whose compassion and determination helped me to become who I am, my father *Shashikant* whose understanding and help led me to where I am. I warmly thank my in-laws, my sister *Mala* and her family for their understanding and support in many aspects of my life.

And Finally, I know that you did not want to be named, my wife, *Jalpa*, without your supports and encouragements, I could not have finished this work, it was you who kept the fundamental of our family, and I understand it was difficult for you. I see myself unable to even express my feelings about the love and patience that I observed from you. I can just say thanks for everything and may God give you all the best in return. Special thanks to our angel daughter *Prishaa*, the true meaning of family. For the past six months, she gave up her most favorite toy, the laptop, in favor of completing the thesis and kept on reminding me saying: “Pappa, take this laptop and write your thesis”!

DA-IICT, Gandhinagar — Jignesh S. Bhatt
November, 2014 — 200921006

Abstract

This thesis addresses the problem of spectral unmixing of remotely sensed hyperspectral data. The spectral unmixing has the objective of quantifying the reflectance properties of different materials on the earth. Complete spectral unmixing includes estimating the number of constituent materials in the data, extracting their spectral signatures called *endmembers*, and estimating their contributing ground cover fractions called *abundances* from each location of the acquired scene. The need of spectral unmixing has been fostered with the development of powerful hyperspectral sensors in the field of remote sensing. These hyperspectral imagers acquire a set of co-registered images of a scene with hundreds of narrow and contiguous bands covering the visible, the near-infrared, and the mid-infrared wavelengths of the electromagnetic spectrum. Due to limited spatial (ground) resolution supported by the high altitude sensors, the materials are often spatially mixed. One can unmix them using algorithmic approaches without the need for spatial resolution enhancement. This thesis contributes new methodologies for decomposing the hyperspectral data into its constituent entities and also provides a unified framework for the complete spectral unmixing of the data. This kind of analysis yields myriad of data products in remote sensing, defense and military, agricultural development, urban planning, and in many other areas.

We begin by estimating the abundances considering cluttered endmembers that could happen in practice. Under linear mixing model, we consider an unmixing problem wherein given the extracted endmembers, the task is to estimate the abundances. This problem is solved using Tikhonov regularization within a total-least squares (TLS) framework that takes care of noise in both the data and endmembers. We discuss the role of regularization in the spectral unmixing, show the analysis of the regularized solution and compare it with a TLS-based direct inversion. The approach is experimentally tested on a synthetically generated hyperspectral data with different noise levels in both data and ground truth endmembers as well as validated on the real hyperspectral data. The performance comparison using different quantitative measures is done with the existing approaches based on the TLS framework.

We next consider the use of Huber-Markov random field (HMRF) prior on the abundances in order to improve their solution. Given the endmembers, we model the corre-

latedness among the abundances as the HMRF in the contiguous spectral space of the data. A maximum *a posteriori* (MAP) approach is used to solve for abundances using the fact that the abundances are dependent on the scene-contents and they represent mixing proportions of the endmembers over the scene area. The HMRF parameter is estimated from the data itself. For this we use an initial estimate of abundances that are estimated based on the matched-filter theory and thus derive a data-dependent or *data-driven* HMRF (*d*HMRF) prior. We present the theoretical analysis that shows the effectiveness of the proposed approach when compared to the state-of-art approaches. The proposed method has the following advantages: 1) The estimated abundances are resistant to noise since they are based on an initial estimate that has high signal-to-noise ratio (SNR). 2) The variance in the abundance maps is well preserved since the threshold in the *d*HMRF is derived from the data itself. The method is first evaluated on the simulated data for increasing noise levels and the sensitivity analysis is carried out for various parameters. The performance is also evaluated on a real hyperspectral imagery. The proposed approach outperforms the state-of-art methods when compared using different quantitative measures.

Accurate estimate of endmembers is important when we attempt to solve the complete spectral unmixing. Towards this end, we next propose a novel approach for endmember extraction which gives band-wise estimate of the endmembers in order to enhance the accuracy of the estimation. This approach explores the spatial, spectral as well as temporal characteristics of the data for endmember extraction. An overdetermined system of linear equations is set-up using the knowledge of abundances and the multi-temporal data, and a constrained least-squares solution is sought to recover the endmembers. The approach is experimentally tested on a set of simulated data synthesized using real hyperspectral signatures. The method not only improves the accuracy of endmember extraction but also results in reduced computational complexity.

Finally we provide a unified framework for the complete spectral unmixing in which we make use of the endmembers extracted using our band-wise endmember extraction algorithm. Inspired from the concept of bootstrapping in the field of linear electronics and by using the multitemporal data, we propose a novel approach for simultaneously identifying the number of endmembers, their signatures and carry out the unmixing without the need of additional information as used by other researchers. Here, the data reconstruction

error (DRE) is utilized as a positive feedback to vary the number of endmembers. The process of iterative bootstraping (IB) is continued until the DRE between the available and reconstructed reflectance is minimum, leading to an optimum solution in the least-squares sense. The entire IB process is further described using geometric illustration. The proposed approach works as a self-regulatory mechanism for the complete spectral unmixing. It can also serve as a basis to find the temporal changes in a hyperspectral scene based on variations in the estimated abundances over a period of time. The efficacy of the method is tested on the multitemporal data constructed using the U.S. Geological Survey (USGS) spectral library signatures. The comparison of the results is shown with the standard hyperspectral unmixing process chains for the increasing noise levels in the data. The sensitivity analysis is carried out to verify the number of spectrally distinct signatures present in the scene, and finally a cross-check is done to further validate the unmixing.

Keywords:

Abundance Estimation; Band-wise Endmember Extraction; Bootstrapping; Huber Function; Hyperspectral Imaging; Ill-Posed Inverse Problem; Markov Random Field; Maximum *a posteriori* (MAP) Estimation; Regularization; Spectral Unmixing.

Contents

List of Figures

List of Tables

Chapter 1

Introduction

1.1 Scope

Remote sensing involves acquiring data from the Earth's surface without physical contact with the area being sensed. Classically, the satellite based sensors capture the data in 4 to 6 different regions in the electromagnetic spectrum covering the visible, infrared and thermal infrared wavelength bands and are well-known as the multispectral sensors. Recently the hyperspectral imaging (imaging spectroscopy) has emerged as a powerful passive remote sensing technology. The hyperspectral imagers (also known as imaging spectrometers) acquire a set of co-registered images of a scene with relatively large instantaneous field-of-view (IFOV) (about $4m \times 4m$ to $20m \times 20m$) and much finer spectral resolution ($10nm$ within more than 200 contiguous wavelength bands). This has enabled quantitative analysis of an area within an IFOV of the sensor. The unprecedented capability of the hyperspectral sensors enables the remote acquisition of images where each pixel is a vector with the high spectral resolution that enables better analysis of contents in an area [1, 2, 3].

Majority of data processing and analysis research in hyperspectral imagery can be categorized as i) detect known and/or unknown targets in a given scene, ii) classify the given image into subregions where a material is predominant, iii) detect changes in a scene over a period of time, and iv) estimate the endmembers and their proportions within a pixel location, so-called spectral unmixing, in order to better understand the scene.

The spectral unmixing of remotely sensed hyperspectral data aims at quantifying the reflectance properties of different regions especially those which are physically inaccessible within an area of the earth. The quantification includes identifying number of spectrally distinct materials, estimating their spectral signatures, and respective abundance fractions [4]. Many times estimating the abundances at every location of the scene or generating the abundance maps of the scene is termed as *unmixing* in the remote sensing community [5]. The more general term *spectral unmixing* has ambitious objectives of updating the spectral library by identifying unknown materials, characterization and quantification of the materials, and to generate the abundance maps of materials found at various areas of the earth.

Apart from this, the spectral unmixing results in better analysis of remote sensing data and this is useful in various applications. To name a few, it includes better classification and segmentation of the scene [6, 7], detecting changes in the scene based on the variations in material reflectance over a period of time [8, 9, 10, 11], super-resolution of the hyperspectral images [12], and developing content-based hyperspectral image retrieval systems [13, 14]. Besides, it contributes in other areas as well which includes the agricultural product developments based on the remote sensing data [15, 16], in marine science, for example to analyze the spectral mixing in macroalgae found in the sea [17], and to analyze biochemical components in the vegetation process [18].

1.2 Hyperspectral Imaging

Hyperspectral imaging systems measure target reflectance in large number of contiguous narrow bands. This larger sampling of the electromagnetic spectrum provides a great increase in the information which is useful in different fields such as agriculture, geography, geology, mineral identification, urban planning, environmental monitoring, surveillance, target detection, and classification of the acquired data. Most hyperspectral imagers measure hundreds of spectral bands, however, the narrowness and contiguous nature of the measurements qualifies them as *hyper-spectral*.

The hyperspectral imaging systems are used to characterize the spectral properties of target depending on the scale of observation covering the visible, near-infrared, and shortwave infrared spectral bands. Table 1.1 briefly describes many hyperspectral imaging systems and their specifications.

Table 1.1: Hyperspectral imaging systems.

	AVIRIS [19]	HyDICE [20]	HyMAP [21]	AIMS [22]	Probe-1 [23]	Hyperion [24]	CHRIS [25]	HySI [26]
Introduction Year	1987	1995	1996	1997	1997	2000	2001	2008
Platform	airborne	airborne	airborne	airborne	airborne	spaceborne	spaceborne	spaceborne
Nominal Altitude (km)	20	6	5	3	2.5	705	550 - 670	100
Spatial Resolution (m)	20	3	10	2	5	30	17 & 34	80
Spectral Resolution (nm)	10	10	17	3	10	10	1.3 - 11.3	15
Spectral Range (μm)	0.4-2.5	0.4-2.5	0.4-2.5	0.4-0.88	0.4-2.5	0.4-2.5	0.415-1.05	0.4-0.95
Number of Spectral Channels	224	210	128	143	128	220	18 & 62	64
Swath Width (km)	12	0.9	6	3	3	7.7	0.13	20

1.2.1 Principles of Imaging Spectroscopy

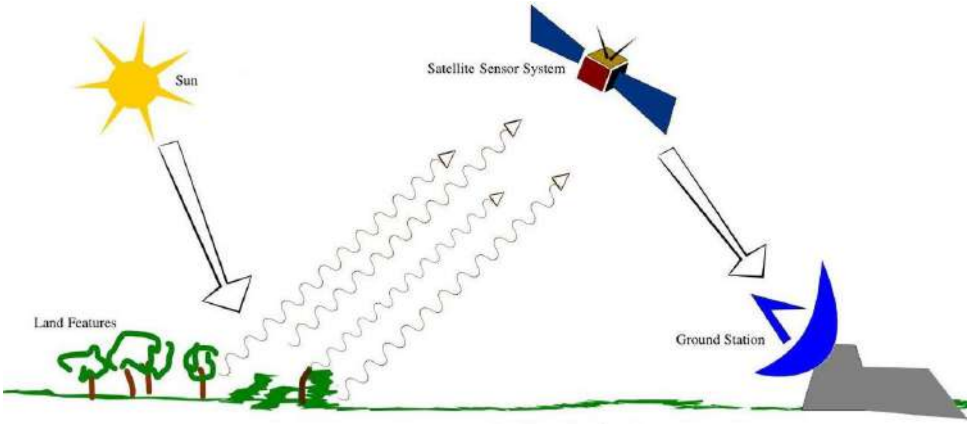

Figure 1.1: Passive remote sensing by satellite based sensors.

Spectroscopic analysis refers to the study of interaction between the materials and radiated energy using a laboratory spectrometer. Hyperspectral remote sensing combines imaging and the spectroscopy in a single system. The idea is to carry a spectrometer on-board the satellite or aircraft to remotely capture the data. This is done using the passive sensing (see Figure 1.1) wherein the light energy from the Sun strikes an object on the earth, and the reflected light is captured by the hyperspectral sensors. These sensors are equipped with a bank of filters designed for recording the data in various bands of the visible to infrared range. Thus the hyperspectral imaging provides a complete reflectance profile of various areas on the earth. This is depicted in Figure 1.2 for some of the pixel locations in an acquired scene data. The data acquired by these sensors is very large [28] and hence we need new methods for its processing and analysis. Hyperspectral imagery is typically collected and represented as a data cube or image cube with spatial information collected in the X-Y plane, and spectral information represented in the Z direction. Figure 1.3 illustrates an example of hyperspectral data cube which has images at different

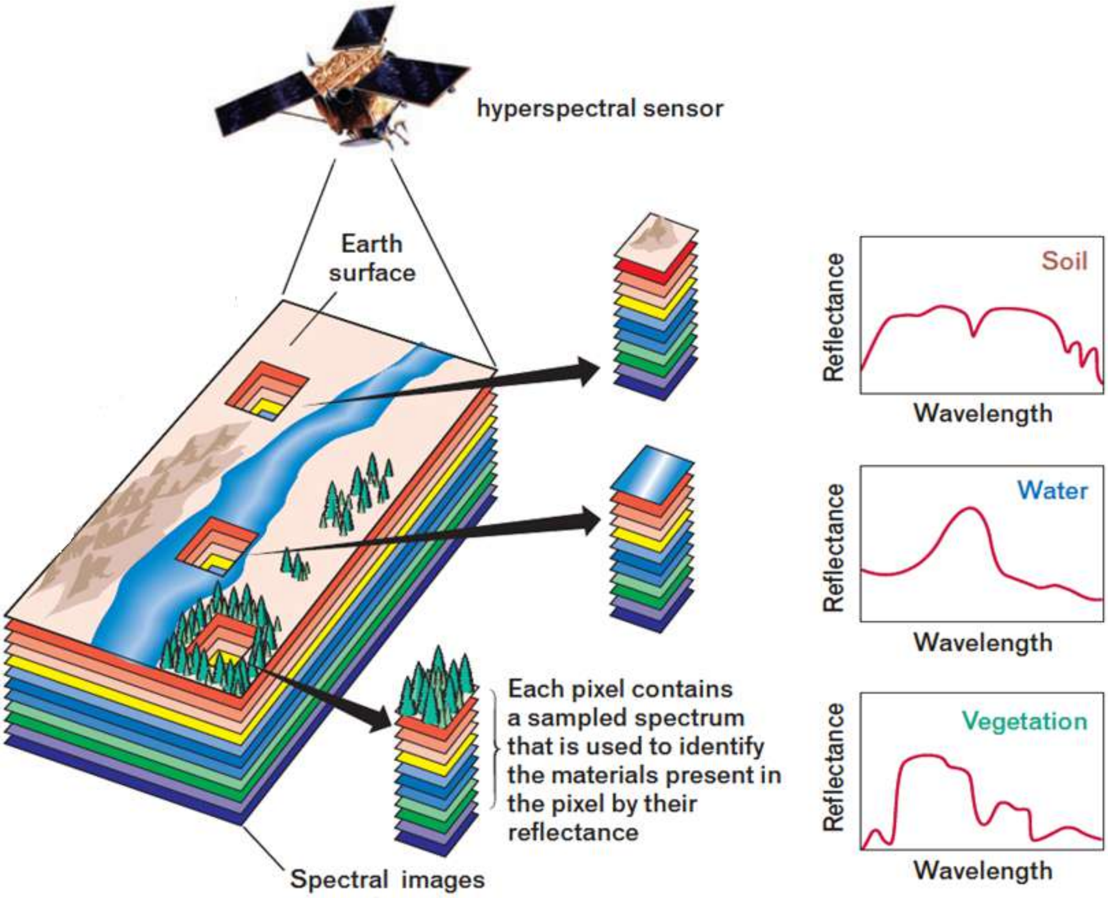

Figure 1.2: Principles of imaging spectroscopy [19, 27]. The plots are showing the bands versus reflectance at few pixel locations.

spectral bands shown in the X-Y plane, and the spectral band range is indicated in the Z-direction.

Figure 1.4 shows some of the real hyperspectral images captured by different sensors. Figure 1.4 (a) shows an image corresponding to band 50 collected by the airborne visible/infrared imaging spectrometer (AVIRIS) [19] by the National Aeronautics and Space Administration (NASA) over the well-known Cuprite mining site located at Nevada, USA. This site is considered as a benchmark for testing the algorithms on hyperspectral data. Figure 1.4 (b) is the French Frigate Shoals image as seen by the CHRIS Proba-1 by the European Space Agency (ESA). In the Figure 1.4 (c) we display the band-31 image of the moon captured by the hyperspectral imager (HySI) on-board the Chandrayaan-1 as a part of the first mission to Moon by the Indian Space Research Organization (ISRO).

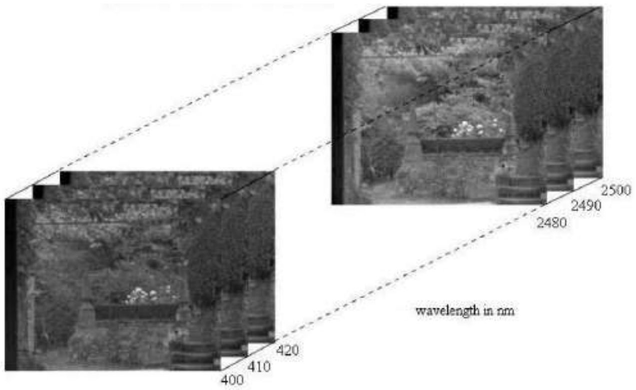

Figure 1.3: An exemplary hyperspectral data with the set of co-registered images acquired at different bands [29].

1.3 Linear Mixing Model

Researchers have attempted to solve the spectral unmixing problem by mathematical modeling of the hyperspectral image formation. However, this itself is a difficult issue since the sensor radiance due to the remote acquisition depends on many hidden parameters including material types, interaction of light intensity with the materials, the way in which they are mixed, scene topology, and the environmental effects. Both the linear and nonlinear modeling have been used for modeling the hyperspectral data [33, 34]. A general model can be considered as having a nonlinear relationship between the reflectance, i.e., pixel intensities, and the entities such as endmembers and corresponding abundances [35]. However, it is difficult to replicate the complete physical mixing phenomena in the generic nonlinear model. Besides, solving the spectral unmixing problem involving nonlinearity has many practical challenges. On the other hand, the linear mixing model presents the natural framework representing the hyperspectral data, and hence its use is prevalent in the remote sensing community. It is a balanced model having the representation accuracy and the mathematical tractability. It is also indicative of many of the real-world scenarios involving hyperspectral data analysis [33]. After analyzing many real hyperspectral datasets, majority of the researchers in the remote sensing community are using the linear mixing model for solving the problems related to hyperspectral data [36, 37]. Our approaches in this thesis are also based on the linear mixing model.

In the linear mixing model (LMM) [38], the data is considered as linear combinations of the endmembers that represent the pure spectra, i.e., spectra of the constituent mate-

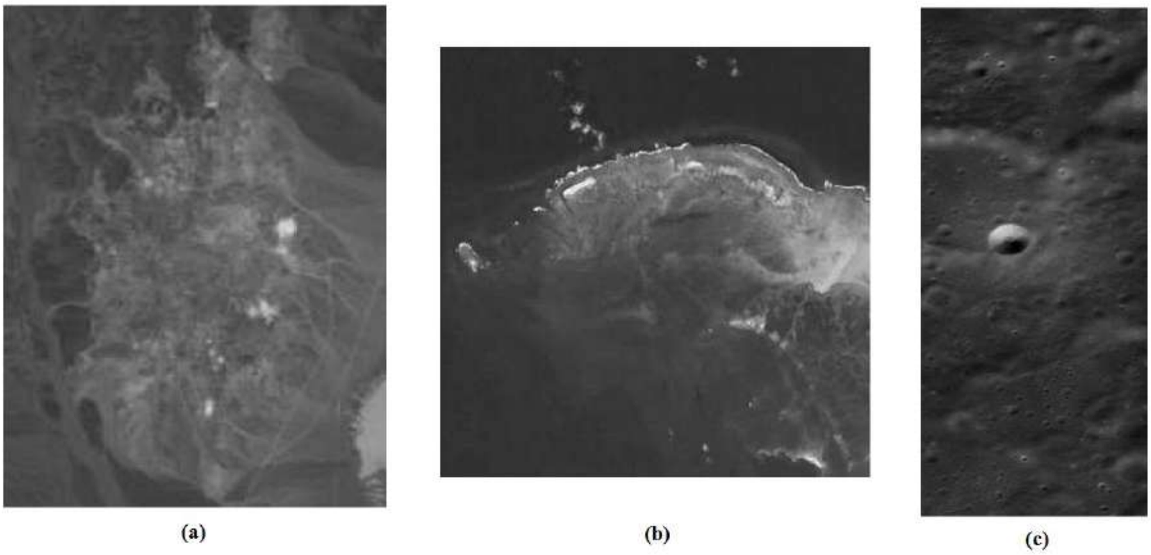

Figure 1.4: Hyperspectral images: (a) Cuprite band-50 acquired by AVIRIS (NASA) [30], (b) French Frigate Shoals by Proba-1 CHRIS (ESA) [31], and (c) a far side of moon band-31 as seen by HySI Chandrayaan-1 (ISRO) [32].

rials, found within the scene. The LMM provides a simple and mathematically tractable framework for solving the spectral unmixing problem [5]. In general, the available radiance data from the remote sensor is first converted to equivalent reflectance values. Then the reflectance data is processed for radiometric calibration, geometric corrections, and necessary atmospheric compensations [39]. Now, considering the LMM at each pixel location in the remotely acquired scene, one may write

$$\mathbf{r} = \mathbf{M}\boldsymbol{\alpha} + \mathbf{n}, \tag{1.1}$$

where $\mathbf{r}$ is the data (reflectance) vector at a location considering W number of bands, the size of which is $W \times 1$. Given e number of endmembers in the scene, $\mathbf{M}$ represents the endmember matrix of size $W \times e$. The corresponding abundances are represented as a vector $\boldsymbol{\alpha}$ of size $e \times 1$. Here, the $\mathbf{n}$ denotes independent and identically distributed Gaussian noise having same size as the $W \times 1$. There are various types of noise sources in the remotely sensed data. It includes the sensor noise due to limiting quality/aging of components, environmental noise, channel noise such as stripping noise and impulse noise, thermal noise present in the circuits, drifts & imperfections due to control mechanisms, etc. However, in general it is difficult to predict the amount and types of noises in the real data acquired by the hyperspectral sensors. By using the theory of Central Limit

Theorem, researchers often model it as additive white Gaussian noise (AWGN). Mostly the noise $\mathbf{n}$ in equation (1.1) includes background noise, instrument noise and can also include errors due to modeling inaccuracies. In order to handle the random nature of noise, it is a common practice in the spectral unmixing research community to carry out the noise sensitivity analysis on the synthetic hyperspectral data.

It can be seen that use of the equation (1.1) at every pixel of the hyperspectral data forms a vector space. Since the images are acquired using the principles of reflectance spectroscopy by the hyperspectral (passive) sensors, the resultant data lies in the W dimensional nonnegative real vector space. The endmember vectors representing the columns of $\mathbf{M}$ are the basis vectors that represent the pure spectra of the constituent materials. These vectors span the W dimensional vector space formed by the hyperspectral data in which the abundances correspond to the weights of the endmember vectors. The hyperspectral data inherently imposes the nonnegativity constraint on the endmembers while the abundance fractions are constrained by the nonnegativity as well as sum-to-one at each location due to the LMM on data.

The LMM can be easily illustrated using a noiseless scenario in the data. Let us consider a data vector $\mathbf{r} \in \mathbb{R}^{+W}$, where W is the available number of wavelength bands, is a linear combination of endmembers weighted by their abundances. Thus,

$$\mathbf{r} = \mathbf{M}\boldsymbol{\alpha},$$

where endmember matrix $\mathbf{M}$ represents the spectral signatures and it has the size of $W \times e$, with e being the number of endmembers. The corresponding abundances are denoted by e-dimensional vector $\boldsymbol{\alpha} = [\alpha_1, \alpha_2, ..., \alpha_e]^T$ where, α_i represents the fractional area covered by the i^{th} endmember.

Figure 1.5 represents the hyperspectral data vectors of a scene as points in the W dimensional Euclidean space. A convex hull is formed due to the data points representing the endmembers of the scene since the corresponding abundances are nonnegative and sum-to-one for each data point. As shown in the figure, all the data points lie within the polygon formed by the endmembers of the scene.

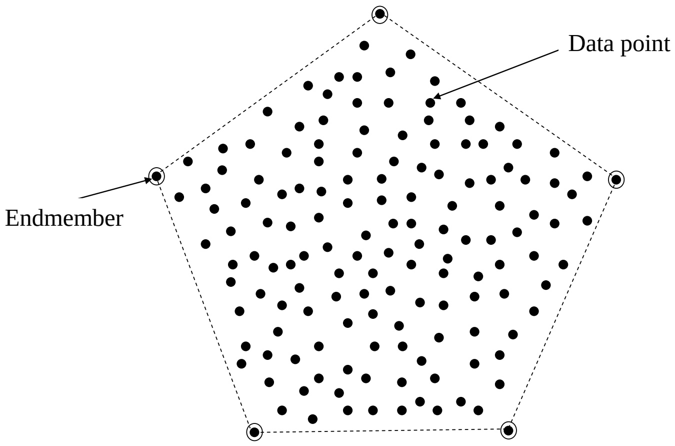

Figure 1.5: Linear mixing model representing data vectors as points in W-dimensional Euclidean space. Endmembers represent the vertices of the polygon comprising the data points. The physical constraints on the abundances lead to the convex hull representation.

1.3.1 Spectral Mixing in Hyperspectral Data

In general, the processing of remotely sensed imagery is a challenging task mainly due to limited resolution offered by high altitude satellite sensors [40]. The hyperspectral data is envisioned for recording material reflectance across the contiguous wavelength bands. A hyperspectral-pixel is a vector which constitutes reflectance across the bands within an IFOV, i.e., it represents spectral response at the IFOV. Pixel values within a band are dependent on many factors that include spatial resolution of camera, scene content, day/time of acquisition, ground area, etc. In order to avail the higher spectral resolution, the sensors offer relatively poor spatial resolution due to the technology trade-off and the hardware limitations. Thus one can consider the reflectance or pixel intensity values as mix of more than one material reflectance within a pixel location, in addition to the various parameters that contribute to its formation. This physical mixing among the spectral signatures is a function of wavelength (λ) and the radiance ρ sensed by the sensor can be simplified at each location of the scene as,

$$\rho = \frac{\int_{\mathbf{0}}^{\infty} \mathbf{B}(\lambda)\phi(\lambda)\mathbf{d}\lambda}{\int_{\mathbf{0}}^{\infty} \phi(\lambda)\mathbf{d}\lambda}, \tag{1.2}$$

where, $B(\lambda)$ is the Planck distribution function and $\phi(\lambda)$ is the spectral response of the detector within an IFOV. Hyperspectral imaging constitute data captured at large number of bands representing the radiance given in equation (1.2). Though (1.2) represents mixing using integration of product of two factors, in practice, this mixing phenomenon has been modeled as either linear or nonlinear mixture of finite number of spectral signatures of constituent materials called *endmembers* present in a scene. In the linear model, reflectance $\mathbf{r}$ is approximated as a linear combination of the endmember signatures constituted by the endmember matrix $\mathbf{M}$. It is conveniently expressed as the linear mixing model (LMM) (1.1) that includes the uncertainty inherent in the data acquisition.

1.3.2 Spectral Unmixing: An *Ill-posed* Inverse Problem

An inverse problem [41, 42, 43] can be considered as given the effects, find out the causes. This is *inverse*, because the effects are normally observed given the causes, which constitutes a forward or direct problem. The solution to an inverse problem allows us to know about the physical parameters that cannot be directly measured or observed. The inverse problems are challenging to solve because of the difficulties involved in inverting in order to get a unique solution. Inverse problems arise in many of the practical situations in the field of science and engineering that include imaging systems. An example of inverse problem is in the area of computer vision where the estimation of depths, i.e., distances of object points, is often of interest. Here, given a 2-D image, one has to estimate the unknown depths which is the third dimensional parameter. In order to solve such problems, the physical phenomena can be suitably represented by mathematical model. The linear model is generally preferred in many applications due to its mathematical tractability. Inverse problems using the linear model aim to estimate the model parameters, given the data. If we have $\mathbf{y} = \mathbf{A}\mathbf{x}$, where $\mathbf{y}$ is the observation vector, the issue in the linear inverse problem is to estimate matrix $\mathbf{A}$ and vector $\mathbf{x}$, given the $\mathbf{y}$. Estimating $\mathbf{x}$, given $\mathbf{y}$ and $\mathbf{A}$ is also an inverse problem. Several problems such as image restoration [44], image deconvolution [45] in the field of image processing, and the signal estimation [46] in the area of communications often use the linear model, and they solve the inverse problem in order to estimate the image or the signal.

The term *ill-posed* problem in mathematics is due to the definition given by Jacques Hadamard for a well-posed problem [47, 48]. Well-posed problems guarantee the following:

1. Existence: a solution exists.
2. Uniqueness: the solution is unique.
3. Stability: the solution is consistent with changes in the input conditions.

As an example consider the $\mathbf{y} = \mathbf{A}\mathbf{x}$, where $\mathbf{y}$ is observed and the $\mathbf{x}$ has to estimated. If $\mathbf{A}$ is a square matrix and if its inverse exist, i.e., $\mathbf{A}$ is well-conditioned matrix, then one can obtain the $\mathbf{x} = \mathbf{A}^{-\mathbf{1}}\mathbf{y}$ which is the unique solution. If any one of the above mentioned properties is not satisfied, then it becomes difficult to invert in order to get the solution. A situation may arise when one does not have a solution at all. In this case, the equations are inconsistent. For example, consider a linear system with two variables x and y, i.e., $x + y = 2$ and $x + y = 3$, which are inconsistent and hence do not have a solution. Many times one may have multiple solutions and it is difficult to decide which is the correct answer. Let's say, an equation $x + y = 2$ which has infinite solutions. Such problems are not well-posed and are termed as *ill-posed* problems in the context of the Hadamard definition.

A problem can also be ill-posed when the transformation matrix $\mathbf{A}$ is ill-conditioned. In this case, a small error in the data can result in much larger errors in the solution. Returning to the linear system $\mathbf{y} = \mathbf{A}\mathbf{x}$, with the matrix $\mathbf{A}$ given in [49]:

$$\mathbf{A} = \begin{bmatrix} 1 & 1 \\ 1 & 1.0001 \end{bmatrix} \therefore \ \det(\mathbf{A}) = \mathbf{1.0000e^{-004}}, \text{ and } \operatorname{cond}(\mathbf{A}) = \mathbf{4.0002e^{+004}}. \tag{1.3}$$

Here, $\det(\mathbf{A})$ and $\operatorname{cond}(\mathbf{A})$ represent the determinant and condition number of the $\mathbf{A}$, respectively. In this case one can see that although the determinant exists, the eigenvalues of $\mathbf{A}$, i.e., $\lambda_1 = 10^{-4}/2$ and $\lambda_2 = 2$, result in a high condition number. Thus, $\mathbf{A}$ becomes nearly singular matrix. Hence, a slight change in the observation $\mathbf{y}$ can drastically change the solution $\mathbf{x}$. This leads to a severe ill-posedness.

It is observed that the inverse problems are generally ill-posed in nature. Hence, it is very difficult to obtain a unique solution. One has to impose certain constraints on the solution in order to obtain a better solution. In practice, the observations are often noisy, i.e., $\mathbf{y} = \mathbf{A}\mathbf{x} + \mathbf{n}$, where $\mathbf{n}$ represents the noise. This effectively avoids the constrained minimization and one may go for unconstraint minimization where prior information about the solution is used in order to arrive at a better solution. The minimization is carried out without imposing the strict constraint. The method of solving an ill-posed problem using the prior is known as *regularization*. This can also be done by using the Bayesian perspective [50, 51, 52]. One can include number of priors as constraints on the solution in order to better restrict the solution space that helps in making the problem well-posed.

Solving for the spectral unmixing using the mathematical model as given in equation (1.1) is an ill-posed inverse problem. First of all the noise and outliers are inherent in the remote sensing data acquisition. Apart from them, there are three different inverse problems involved while performing the complete spectral unmixing. In the hyperspectral data, the number of endmembers e is found to be significantly less than the available bands W. This is similar to pigeon-hole problems wherein the pigeons, i.e., number of endmembers, are far less than the holes, i.e., spectral bands. This leads to multiple solutions and hence it is hard to determine the exact value of e from the available data. Looking at (1.1) we see that there are less number of knowns, i.e., reflectance. The endmembers extracted from the data need to be linearly independent since they correspond to distinct constituent spectra with their values in each band satisfying the nonnegativity constraint due to the passive remote sensing. Finally, the abundances must be constrained by both nonnegativity and sum-to-one. This leads to solving an overdetermined system of equations satisfying the number of physical constraints. Hence, solving for the complete spectral unmixing or solving for any of the single entity is difficult since it results in *ill-posed* inverse problem due to reasons mentioned above.

In this thesis, we propose different approaches for solving the *ill-posed* inverse problem of spectral unmixing. Our approaches are novel and inspired from the Bayesian inference and the regularization frameworks.

1.3.3 Mixed Pixels in Hyperspectral Imagery

The hyperspectral sensors have a high spectral resolution, but they have limited spatial resolution. This results in mixed-pixels in the hyperspectral imagery, i.e., presence of multiple spectral sources within a pixel location. Figure 1.6 illustrates the concept of the mixed pixels considering the data as linear combinations of the endmembers or spectral signatures that represent the pure spectra found within the scene. Pixels corresponding to a single spectral signature are called pure pixels. Note that the reflectance corresponding to such a pixel location indicate the presence of one of the endmembers at that pixel. Mixed pixels are inherently found at almost every location of the scene due to the relatively poor spatial resolution of hyperspectral image. However, one may also find mixed pixels in the data even when the spatial resolution is high [6]. A part of an exemplary scene shown in Figure 1.6 having a spatial resolution of $3m \times 3m$ has such mixed pixels with three endmembers, viz, grass, tree and soil. A pixel marked with the thick borders has the mixing proportions (abundances) as given in the box.

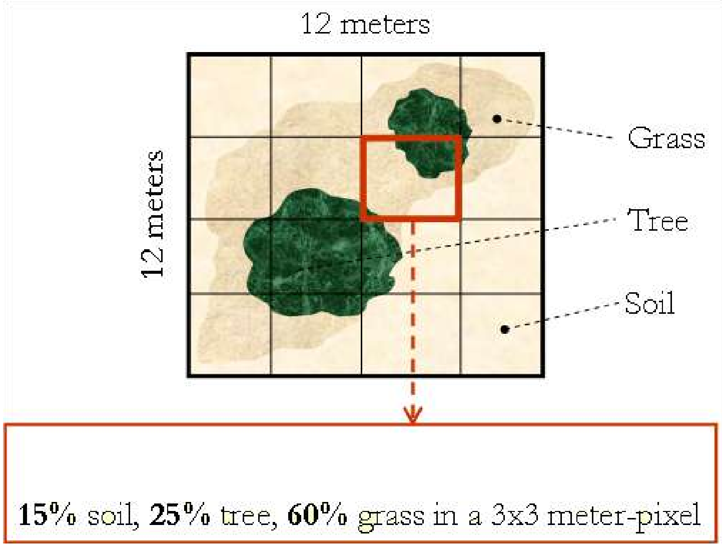

Figure 1.6: Existence of mixed pixels in hyperspectral imagery [53].

Our work in this thesis involves estimating the abundances given the other two unknowns, i.e., number of endmembers and their signatures, and to extract the endmembers, given the abundnaces and number of endmembers. Finally, we solve the complete spectral unmixing problem in which we estimate all the three entities, given the data. This is similar to the blind source separation problem for which different methods and frameworks including the independent component analysis (ICA) have been proposed [54, 55, 56, 57, 58, 59]. However, most of these methods/frameworks can not be applied for solving spectral unmixing because of the severe ill-posedness in the problem. Since the sources are actually dependent in the hyperspectral data, the ICA based techniques are not suitable to perform the spectral unmixing [60, 61].

1.4 Thesis Contributions

This section summarizes the topics addressed in the thesis and our main contributions. We begin by estimating the abundances considering the cluttered endmembers. Next problem considers the abundance estimation given the true endmembers of the scene. Then the problem of endmember extraction is addressed. Finally, number of endmembers, their signatures and corresponding abundances are simultaneously estimated in a single algorithm that is we perform blind decomposition of the given data. We call this as the complete spectral unmixing of the hyperspectral data.

Towards this end, we first discuss the linear mixing model (LMM) for the remotely acquired hyperspectral data. The LMM accounts for modeling the general degradations found in hyperspectral data including the instrument noise. We then review the literature on our works estimating each of the three entities in the spectral unmixing, i.e., estimating the number of endmembers, their signatures and corresponding abundances, as well as works involving joint estimation of more than one entity. Finally, approaches incorporating the usage of multitemporal data for change detection and unmixing are also reviewed. Our thesis contribution include following:

- To begin with, we consider an unmixing problem wherein given the noisy data and the corrupted endmembers, we estimate the corresponding abundances. We propose a regularization based approach within a total least-squares (TLS) framework for recovering the underlying abundance maps. The ill-posedness is handled by considering a Tikhonov prior on the abundances. The formulated objective function is minimized using gradient based method. A theoretical analysis is carried out to show the effectiveness of the regularization for restricting the solution space in order to arrive at a better solution. We also analyze the role of regularization in solving the unmixing problem. The experiments are conducted on synthetically generated data constructed using the USGS library signatures with increasing levels of noise in the data. After verifying consistency in the spatial abundance patterns within the estimated abundance maps, the results are quantitatively compared using different measures with the existing TLS-based approaches. The performance of the proposed approach is also tested on the real AVIRIS Indian Pines data. The results are validated for the consistency in the spatial patterns in the maps and then the quantification of the unmixing errors is done in terms of the data reconstruction error. Our algorithm outperforms the existing TLS-based approaches.

- The hyperspectral signatures representing the endmembers are strongly correlated due to nature of the data. This leads to an ill-conditioned endmember matrix. The underlying abundances of the scene are either smoothly varying or have sudden variations depending upon the mixture of the signatures at a location. The inevitable presence of noise and outliers in the data adds the uncertainty while solving the unmixing problem. Hence, estimating the abundances is a challenging problem even with the ground truth endmembers. To this end, we next propose a new data-driven prior and the same is used to take care of the ill-posedness in the unmixing. For this, we develop a two-step Bayesian method in which the dependencies in the abundances are estimated in the first step to yield a data-dependent Huber-Markov random field (*d*HMRF) model for the abundances. The posterior probability is then maximized in the second step using particle swarm optimization (PSO) which is guaranteed to converge. The MAP optimization is initialized by particles drawn from Dirichlet distribution enforcing the required physical constraints on the solution. The proposed method uses only the available data to estimate the necessary parameters and hence effectively avoids the learning of the parameters from the large datasets. A theoretical analysis along with the geometric illustration is carried out to show the competency of the method. The experiments are conducted on synthetically generated scene having different mixing proportions. The noise sensitivity analysis is then carried out and the results are compared with the existing state-of-art methods using different quantitative measures. The processing time of the proposed algorithm is also compared with the other approaches. Finally the abundance maps of the real AVIRIS Cuprite data are estimated using the proposed approach. The results are first validated for the visual consistency of the maps with the existing state-of-art algorithms and then the quantification of the unmixing errors is done in terms of the data reconstruction error. Our algorithm outperforms the existing state-of-art approaches.
- The hyperspectral data is composed of the endmembers and their distribution representing the abundances over the scene. Hence, given the endmembers, the corre-

sponding abundances can be estimated; and given the abundances, the endmembers can also be estimated since these two together form the reflectance values. Hence, after the work on abundance estimation, a novel approach for estimating endmembers of the scene is developed in this thesis. This method integrates the spatial, spectral as well as temporal characteristics of a scene to better constrain the endmember values in each band. An overdetermined set of equations are formulated using the multi-temporal data and the knowledge of estimated abundances. The formulated objective function is minimized using the nonnegative constrained least-squares framework. Our approach is validated by conducting experiments on the simulated data and comparing our results with the state-of-art approaches. The proposed algorithm competes with the current state-of-art approaches, yet it has much lower processing time as well as computational complexity. This algorithm requires the availability of the abundances, and the same is overcome in our next contribution.

- Finally, given the multitemporal data, we solve the complete spectral unmixing problem which is a blind decomposition of the data. We develop a completely new framework for simultaneous estimation of number of endmembers, their signatures and abundances. This method provides the complete solution in a single algorithm. The framework is inspired from the principles of bootstrapping used in the theory of linear electronics. To carry out this work, we use our endmember extraction algorithm. Data reconstruction error (DRE) is used as a feedback to obtain the complete spectral unmixing iteratively. This is a self-regulatory mechanism which converges in the least squares sense. The experimentation is carried out using the multitemporal data synthesized using the real hyperspectral signatures of the USGS spectral library. First the algorithm is tested for the correctness of number of endmembers and the final results are compared with the existing approaches. Error analysis is carried out and the time complexity is calculated. To the best of our knowledge, this is the first method which solves for all the three unknowns in a single algorithm. Hence, in order to compare our results, we combine the state-of-art approaches for each of the unknowns in a chain. The proposed framework outperforms the standard chains of spectral unmixing comprising of the current state-of-art approaches.

All our algorithms are run on a Desktop PC with Intel® Core^{TM} i5-3210M CPU at 2.5 GHz with 4 GB of RAM. These algorithms are implemented in MATLAB® running on a 64-bit operating system.

1.5 Thesis Organization

The organization of the thesis mentioning the contribution is shown in Figure 1.7 showing flow of the work. It begins with an introductory chapter on the orientation of the problem with the linear mixing model. Subsequently, each of the work is arranged as an individual chapter (see Figure 1.7). Finally, the thesis provides the concluding remarks and future research lines.

The thesis is organized as follows. Chapter 1 discusses the principles of imaging spectroscopy, spectral unmixing problem and linear mixing model. Chapter 2 reviews the research work carried out in the area of spectral unmixing. The TLS-Tikhonov regularization method for estimating the abundances, given the data and perturbed endmembers is presented in Chapter 3. In Chapter 4 we discuss the MAP-*d*HMRF based data-driven stochastic approach to unmix the hyperspectral data. A new approach for endmember extraction is discussed in Chapter 5 in which we show how the accuracy of endmembers is improved by using the multi-temporal data. Chapter 6 presents a novel framework for a blind estimation of number of endmembers, their signatures and abundances, called Iterative Bootstrapping (IB). Finally in Chapter 7 we conclude the thesis by summarizing the main contributions and by listing out future research directions.

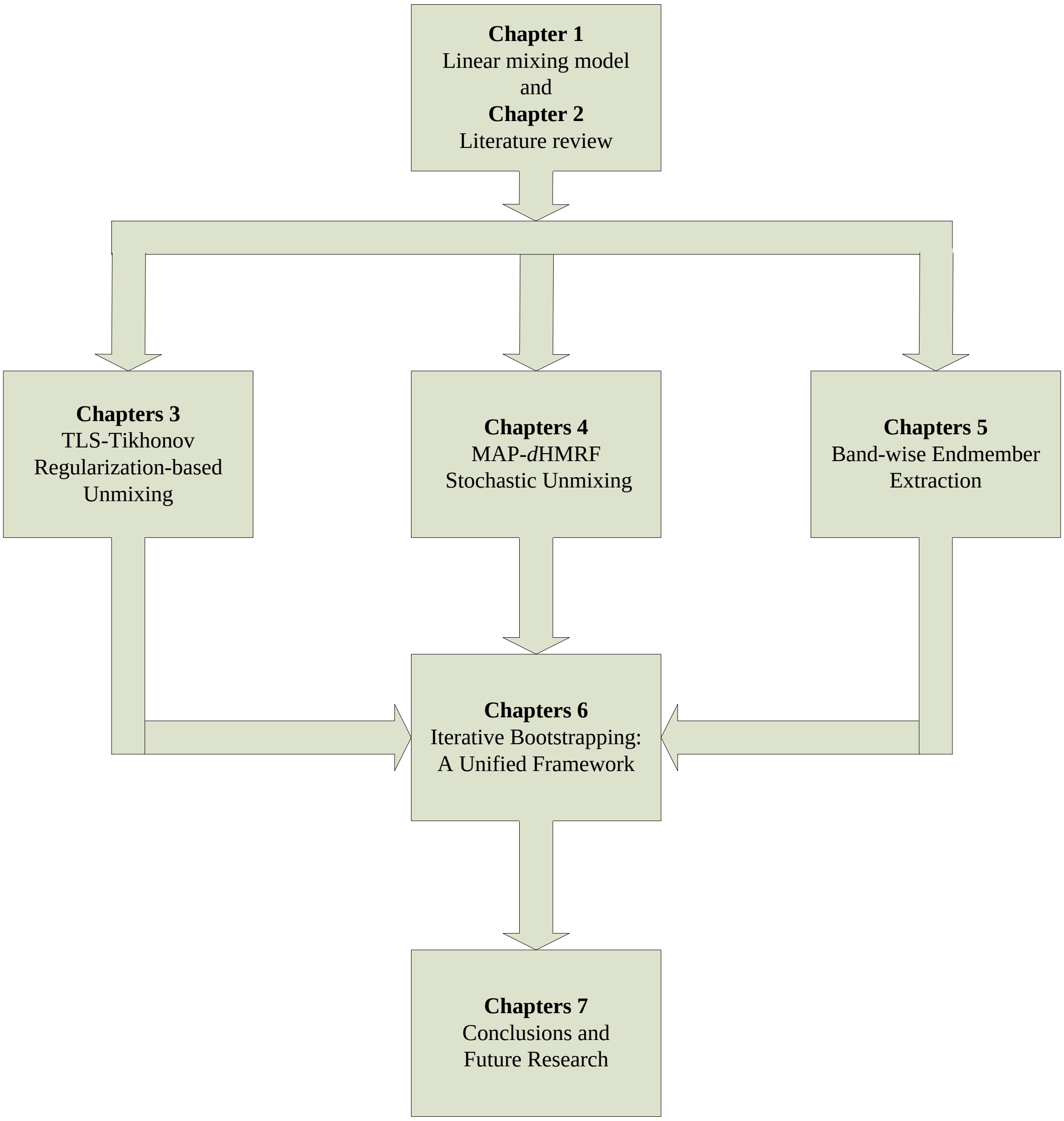

Figure 1.7: Thesis Organization.

Chapter 2

Literature Review

Spectral unmixing of hyperspectral data is actively researched since over three decades. Goetz *et al.* [1] has introduced this idea of decomposing the hyperspectral data into its constituent components back in 1985. Since then many researchers have worked on this problem that has resulted in various approaches. Given the data, complete spectral unmixing solves for the three unknowns, i.e., it starts by identifying number of spectrally distinct materials in the data followed by extracting their spectral signatures called *endmembers* and finally estimating the corresponding ground cover fractions called *abundances*. Solving this inverse ill-posed problem poses major challenges primarily due to the existence of mixed pixels in the data, variations in atmospheric conditions, sensor noise, material decomposition, location, and unknown background. The researchers have attempted to solve the problem using mathematical modeling of the hyperspectral data.

A very first model for analyzing the spectral reflectance was proposed in the year 1979 for the mars data [62]. In the year 1981, the well-known *Hapke*'s model was proposed [35]. This model being a nonlinear mixing model was more difficult to handle. There are several challenges involved in using the nonlinear model including number of parameters, their interrelationships, methods of estimation, obtaining a fast solution, etc. More recently, the nonlinear unmixing methods have been reviewed in [63]. It should be noted that the use of the nonlinear mixing models are mainly application-dependent [64, 65, 66]. In [67] a geometric distance based method is proposed for the nonlinear unmixing of the hyperspectral data. This method could serve as a generalized framework for the nonlinear unmixing methods.

In the year 1983, Johnson *et al.* [68] proposed a linear version of the *Hapke*'s model

[35] to unmix binary minerals mixtures. Linear mixing model (LMM) provides a better framework to represent the hyperspectral data using convex and affine geometry concepts [38] and, hence this model is prevalent in the remote sensing research community [69, 5, 33]. In 1997, authors in [70] proposed a linear stochastic mixing model (SMM) by integrating the principles of spectral clustering with the LMM, and its convergence issues are discussed in [71]. The SMM is also a linear model since it assumes that the data is linear combinations of the endmembers, however, it considers the probabilistic model where both the data and endmember signatures are modeled in probabilistic sense rather than as deterministic spectra as in LMM. Though SMM offers the generalization, it has to handle an additional challenge of estimating the model parameters while solving for the spectral unmixing [72]. In this thesis, we have used the LMM to solve the problems related to the hyperspectral unmixing.

Traditionally, the problem of spectral unmixing has been attempted by the researchers to solve for the three entities separately within a standard hyperspectral unmixing chain [73, 4, 74, 5]. Figure 2.1 depicts a complete spectral unmixing chain including an illustration using an exemplary data. We assume here that the reflectance in the data cube is preprocessed for radiometric, geometric and atmospheric corrections. As shown in the figure, the analysis starts by first identifying the subspace of the W dimensional data vector space. This is also known as finding the number of spectrally distinct signatures in the data or model order selection for representing the data. The next task is to extract the spectral signatures from available data and form an endmember matrix $\mathbf{M}$ for the scene. Finally, the abundances $\boldsymbol{\alpha}$ corresponding to the each endmember are estimated at every pixel location for the entire scene. Note that the nature of these three problems involved in the complete spectral unmixing is entirely different. However, they are inter-related and hence can be conveniently processed in a chain wherein given an entity, the unknown can be estimated. The efficacy of the algorithm can be assessed by checking the error between the available reflectance and the reflectance reconstructed using estimated unmixed components [75].

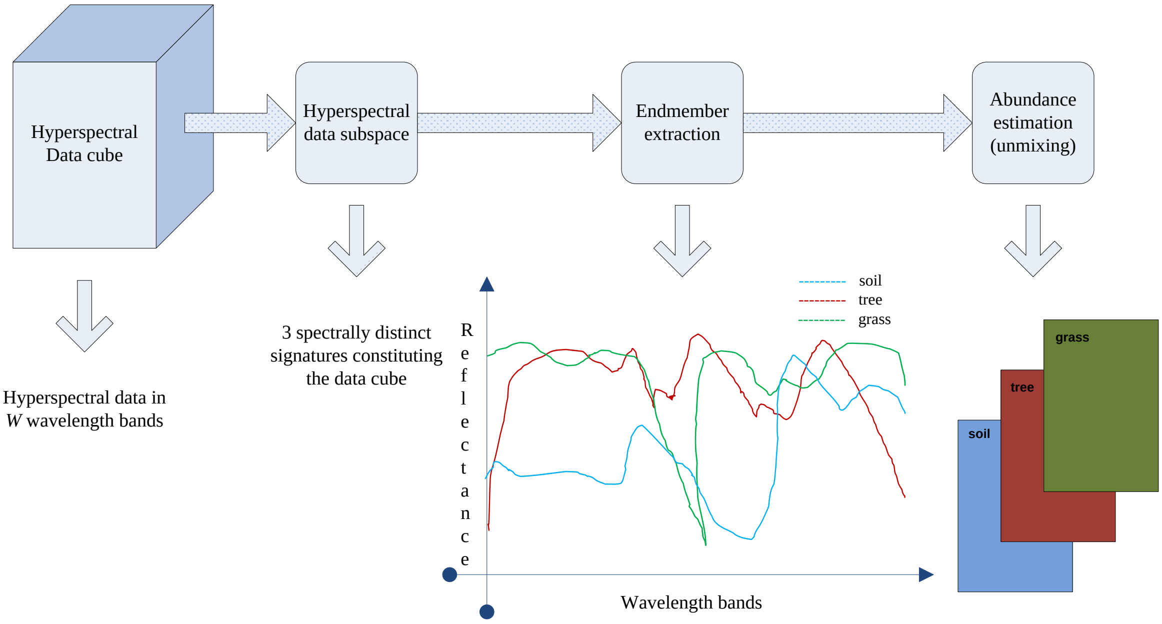

Figure 2.1: Illustration of complete spectral unmixing chain for hyperspectral data. The spectral signature plots corresponding to three constituent endmembers and their abundance maps are also shown. The data is assumed to be preprocessed for necessary geometric and radiometric corrections including atmospheric compensations.

2.0.1 Hyperspectral Data Subspace

Given the data, first step is to find the corresponding subspace of the data, i.e., to find the number of endmembers in the given data. This often requires the knowledge of experts and/or ground survey. Considering a model representing the data, this problem has a similarity with the model-order selection problem [76] formulated in the communication systems. The task becomes difficult for physically inaccessible areas on the earth. Comparing the hyperspectral imaging with the pigeon-hole principle, the number of endmembers is found to be significantly less than the available bands. Hence, in general, it is difficult to estimate the number of endmembers exactly and a reasonable estimate can be obtained based on trial-and-error criterion [77, 78]. To this end, few algorithms have been developed. In [79], the researchers have tried to determine the dimension of subspace by using the concept of virtual dimensionality (VD) of the data. A binary hypothesis is formulated by the eigenvalues of data correlations and covariance matrices to recover the subspace dimension of the data. The method considers the noise covariance while estimating the number of spectrally distinct signatures.

An eigen decomposition of estimated correlation matrices of the data and Gaussian noise for finding the number of endmembers is proposed in [80]. This method is well-known as HySime and it estimates the subspace of the data in the minimum mean-squared sense. Authors in [81] have generalized the existing approaches for identifying the subspace of the data. A method based on maximum orthogonal subspace projection approach has been derived for estimating the number of spectrally distinct sources in the data [82]. Recently, a greedy algorithm has been developed using the concepts of convex hull geometry in [83]. More recently, equivalence between the greedy pursuit algorithms and the pure pixel based approaches is established and the same is used for identifying the number of endmembers in the data [84]. This is based on the sparse regression formulation used in the area of spectral unmixing.

2.0.2 Endmember Extraction

In many instances the spectral signatures for the materials, i.e., entities of the $\mathbf{M}$ matrix, are available in the spectral library [85]. They can also be extracted from the data using various algorithms [5, 86, 87, 88, 89]. Many of these approaches assume the presence of at least one pure pixel-vector belonging an endmember in the data. These are called pure pixels based approaches. The assumption that the pure pixels are found in a scene is quite reasonable considering the resolution of the data. In the earlier days, approaches based on geometric concepts that consider the noiseless situations were developed [90, 91]. Subsequently, many algorithms have been developed considering the noisy scenarios, and nowadays the focus is more towards the methods based on optimization which explore the different characteristics of the data in order to further improve the solution [33].

Algorithms for the endmember extraction mainly explore the spectral space of the data to estimate the signatures. These algorithms are based on the convex analysis which is based on pixel purity index (PPI) of the data [92]. A faster implementation of the PPI is proposed in [93], and is recently modified in [94] to include the uncertainty in the spectral signatures. A seminal work based on the minimum-volume transforms by Craig [95] has influenced many of the subsequent research works in the endmember extraction. It is based on the fact that the hyperspectral data can be considered to form the convex hull generated by the endmembers and the volume of this convex hull can be used to determine the constituent spectral signatures. Parallel to this, a method based on the concept of orthogonal subspace projection (OSP) is proposed in [96] and later described in detail [97]. OSP is based on the assumption that one may decompose the available data into desired and undesired set of spectral signatures. Using the available data and the number of endmembers, OSP proceeds by considering a data pixel-vector having largest norm as the first endmember. The remaining endmembers are determined iteratively by exploiting orthogonality with respect to the available signatures within the data. A novel approach to endmember extraction known as N-FINDR is proposed in [98]. The approach is based on finding the volume of the available data vectors by using an iterative search. However, it suffers from high computational complexities and is vulnerable to noise and outliers. In order to achieve a better solution, the idea of convex geometry has been generalized in [99] in which the authors have used probabilistic approach called as the iterative constrained endmembers (ICE). At the same time, considering a noiseless scenario, two more algorithms have been developed. One of them is the successive projections algorithm (SPA) [90] which is based on iteratively identifying the purity of the pixels in the data. The SPA can be considered as column pivoted Gram-Schmidt process [100]. The second approach was automatic target generation process (ATGP) [91] for the endmember extraction. By the time, the algorithms were still using the convex hull formulation by the endmembers as demonstrated in the N-FINDR algorithm [98]. Variants of the N-FINDR can be seen in [101]. The number of computations in the N-FINDR is then drastically reduced by incorporating the idea that the endmembers represent the vertices of a simplex form in the given data and it is well-known as vertex component analysis (VCA) [102]. The approach is based on the geometry and works on the property that affine transformation of a simplex is also a simplex.

In order to obtain a better solution, the research in the endmember extraction has progressed with the integration of the spatial information in addition to the use of spectral space of the data. There are several approaches of endmember extraction which use spatial adjacencies within the band along with the spectral measurements. These include automatic morphological endmember extraction (AMEE) [103], spatial spectral endmember extraction (SSEE) [104], and spatial preprocessing (SPP) [105]. Note that these methods invariably assume the presence of pure pixels within the acquired data. However, due to the noise and the other imperfections, the acquired data often has erroneous reflectance and it is difficult to accurately estimate the endmembers using the corrupted data. The state-of-art methods find the endmembers close to the ground truth in terms of geometrical [106, 107] or statistical distances [108].

A class of algorithms for the endmember extraction have been developed relaxing the assumption of pure pixels within the data [109]. The endmember extraction using the nonnegative matrix factorization (NMF) formulation was introduced in [110]. A method known as minimum volume constrained nonnegative matrix factorization (MVC-NMF) is proposed in [111] for highly mixed data without making any assumption on the purity of pixels. It introduces the minimum volume constraint in the regularization framework for restricting the solution space. A convex analysis component is added within the minimum-volume framework in [112]. On the other hand, a simplex volume maximization algorithm framework is explored in [113]. More recently, fast and recursive NMF algorithms are proposed for verifying the validity of such separable decompositions [114]. A method based on Dirichlet process is devised for endmember extraction in [115].

2.0.3 Abundance Estimation (Unmixing)

Knowing the endmembers, unmixing can be done by estimating the corresponding abundances at each location. The abundances represent the fractions (weights) of the endmembers and they are required to satisfy nonnegativity constraint due to the passive remote sensing. Apart from this, the abundances must sum-to-one at each pixel location in the scene. The problem of estimating the abundances is ill-posed.

A very first solution for the abundance estimation was derived using the concept of principal component analysis [116]. Since then the area is actively researched to obtain a better solution for abundances, and thus making it a better-posed. Various algorithms for unmixing are based on constrained-energy-minimization (CEM) [117, 118], unconstrained regularization [119] and maximum-likelihood estimation (ML) [120, 74, 121]. Among the other approaches, fully constrained least-squares (FCLS) [122] is a well-known method that represents generalization of the least-squares formulation. Recently, a simplex projection based FCLS method [123] presented geometrical equivalence of the FCLS. In [124, 125, 126] nonnegative solutions using the principles of maximum entropy have been proposed. Researchers have also attempted to solve the problem of abundance estimation by using regularization framework in which various priors on the abundances are used to obtain better solution. A Bayesian perspective is used in [127] by imposing a volume prior and the method is based on the nonnegative matrix factorization approach. For unmixing the data, i.e., estimating the abundances, the concept of endmember variability is considered in [128]. Authors in [129, 130] proposed unmixing based on total least squares (TLS) approach in which the solution space is restricted to yield physically constrained abundances. In our recent work [131], we proposed a regularization based approach for abundance estimation, in which a Tikhonov prior was used. Many of the methods use priors that model the spatial correlations among the abundances [132, 133, 134], without considering their dependencies across the spectral space. Recently, we proposed a Huber-Markov random field (HMRF) over the spectral space of the data in order to obtain better abundances [135].

The abundances are nonnegative and sum-to-one which is same as being sample functions of a Dirichlet process [136, 137]. This idea of using Dirichlet process is used in [138] for unmixing by modeling the mixtures as the Dirichlet components. Recently, a dynamic framework for unmixing is proposed [139] for an application in agriculture development and monitoring the growth in the plants. Methods based on using the neural network to unmix the highly mixed data can be found in [140, 141, 142]. Further, lattice structures have also been applied to unmix the hyperspectral data in [143].

Few researchers have also explored the possibility of using the compressed sensing (CS) theory [144, 145] to solve the unmixing problem. The theory of CS involves estimation of sparseness in the data. Authors in [146, 147, 148, 149, 150, 151] have formulated the problem of estimating the abundances as a linear sparse regression by making use of set of endmembers. Approaches based on learning the sparse codes have been proposed in [152, 153, 154]. Besides, wavelet based approaches have also applied for hyperspectral data analysis [155]. Considering the severity in the ill-posedness of the problem, recently the researchers have started to further explore the regularization-based algorithms in order to achieve better solution. A total variation regularization is formulated to unmix the hyperspectral data in [156]. More recently, we proposed a MAP-dHMRF based stochastic approach for abundance estimation that uses the *data-dependent* prior over the spectral space [157]. A suitable value of Huber threshold is derived from the available data and the resultant MAP solution overcomes the ill-posedness in the unmixing due to the noise and ill-conditioning of the endmember matrix due to the strong correlation among the spectral signatures. It is interesting to see that the estimated abundances can also be used for extracting the endmembers as demonstrated in [158].

2.0.4 Joint Estimation and Miscellaneous

Few of the researchers have worked on the joint estimation of more than one entity in the complete spectral unmixing. A joint estimation of the number of endmembers and abundances is proposed in [159], while the authors in [160, 111, 161] proposed joint estimation of the endmembers and abundances. A study on the impact of initial endmembers in searching the number of endmembers and finding their signatures has been carried out in [162]. In [159] a hierarchical Bayesian model is proposed for estimating abundances and number of endmembers in which the problem is formulated as constrained linear regression. Although the method simultaneously estimates the abundances and the number of endmembers, it requires the knowledge of endmembers.

Few researchers have attempted the joint estimation of the endmembers and corresponding abundance maps. Such a joint estimation is formulated as a biconvex optimization problem [160], and is heuristic. It is based on alternatively updating endmember and abundance matrices via projected subgradients. To this end, fully Bayesian hierarchical algorithm is proposed in [161] which uses a computationally expensive generalized Gibbs sampler. The method illustrates the nonuniqueness of the solution while attempting the joint estimation. To the best of our knowledge, methods based on single algorithm framework is not available in the literature for estimating all the three entities for the complete spectral unmixing.

In recent times, many researchers have started exploring unmixing using multi-temporal hyperspectral data. An FCLS-based unmixing is applied to multi-temporal hyperspectral data in [8] for the change detection. Their algorithm was tested on the data acquired using compact airborne spectrographic imager (CASI) in North Research Farm of Mississippi State University. An application of multi-temporal unmixing for finding the vegetation index is shown in [9]. An unmixing analysis using nonnegativity constraint least-squares has been demonstrated in [11] for Hyperion images captured over Guanica dry forest in Puerto Rico. These methods demonstrate their approaches by showing the changes in the scene due to the variations in abundances over a period of time. A limitation of these methods is that they require prior knowledge about the endmembers in a scene. An approach involving the spectral variability of the endmembers within the scenes while using the temporal data is proposed in [163]. However, no attempts have been made in the literature to solve for all the three entities in a single algorithm as attempted in this thesis.

Considering the advancements in high performance computing technology, researchers have now started to export the algorithms to facilitate the on-board processing of the hyperspectral data [164]. To this end, one has to fuse the programs on a specific hardware platform that requires either the modification of the existing algorithm or to develop entirely a new approach. Many times parallel processing of the high dimensional spectral data [165] can be employed for the fast processing. Authors in [166] implemented the N-FINDR algorithm on the field programmable gate arrays (FPGA). The graphics processing units (GPU) are also utilized for the parallel unmixing application in [167].

Chapter 3

A regularization based method for unmixing imaging spectrometer data

We begin our work with abundance estimation where the imaging spectrometer data is unmixed to yield underlying proportions (abundance maps) of the constituent materials. We consider a situation where the endmembers are perturbed or one has partial information about the endmembers. Given the perturbed endmembers and the data which is inherently noisy, the task is to estimate the abundances. This is a severely ill-posed problem, since the errors in the data as well as in the endmembers lead to deviations in the final solution while unmixing the data. In order to solve this, we adopt the regularization-based approach that restricts the solution space. For this purpose, we use Tikhonov regularization within the total least squares (TLS) estimation framework. An objective function is formed which is sum of the TLS data-term which takes care of the possible perturbations in both data and endmembers, and the Tikhonov prior on the abundances that imposes the smoothness constraint. The resultant function being convex is minimized by gradient descent optimization technique wherein the solution space is restricted to yield physically constrained abundances. A theoretical analysis of the regularized solution is carried out to show the effectiveness of the method. We also analyze the role of regularization in solving the unmixing problem. Experiments are conducted by using different noise levels in the simulated data and the results are compared with the TLS based approaches using different quantitative measures. The results are also compared for testing the consistency within spatial patterns of the estimated abundances. Finally the proposed approach is applied on the real AVIRIS Indian Pines data to obtain abundance maps of the constituent materials of the scene, and the results are verified with the published results.

3.1 Introduction

Over the past three decades, various geometrical, statistical and sparse-regression based unmixing approaches have been investigated [5, 87, 86]. The efficacy of an algorithm can be assessed by checking the error between the ground or the available reflectance and the reflectance reconstructed using the estimated unmixed components. This requires accurate estimation of endmembers as well as the abundances at each location of the remotely acquired scene, since together they yield a pixel value (reflectance) in the data. However, most of hyperspectral data processing are focused on either the least-squared error (LSE) and/or the spectral angle mapper (SAM) based error metrics as highlighted in [75], which consider the presence of noise, only in the data. The LSE based unmixing approaches are either based on the maximum-likelihood (ML) estimation framework or its variants [117, 119, 74, 121, 168]. Among the other approaches, fully constrained least-squares (FCLS) abundance estimation [122] is a well-known approach that represents generalization of the least-squares formulation. Recently, these classical unmixing approaches are compared to understand the adjacency phenomenon caused by the atmospheric scattering [169].

A more practical scenario is to consider the possible perturbations in the endmemebrs as well as in data while unmixing the scene. This motivates us to work forward in the total-least squares (TLS) framework for solving the critically ill-posed problem at hand. Authors in [129] proposed unmixing based on total least squares (TLS) approach which is an unconstrained solution. Considering the literature, we found that the regularization based approaches are nowadays getting more attention primarily due to their adaptability in handling the ill-conditioning. In the past, a truncated TLS solution for unmixing the data has been obtained by regularizing the eigenvalues of the endmember matrix in [130]. However, this lacks real time applications due to heavy computational cost. A constrained unmixing using the entropy of the solution as a prior has been proposed in [126] which is well-known as MaxEnt. A method based on total-variation spatial regularization for unmixing is proposed in [156]. A method using simulated annealing based spatial regularization is proposed for finding the abundance maps which in turn are utilized for hyperspectral image classification [6]. In [170, 171, 161, 172, 127] the approaches based on Markov chain Monte Carlo method have been investigated, however, they suffer from high computational complexity. Many of the methods proposed in the literature use different kind of priors for modeling the spatial correlation of the abundances [132, 133, 134]. Researchers also have explored the regularization framework to obtain a joint estimation of endmembers and abundances in [111] incorporating the concept of nonnegative matrix factorization (NMF). However, this suffers from getting stuck at a local minima due to nonconvexity of the objective function. A solution to this problem is provided using the graph based regularization to unmix the data in [173]. Recently, Tikhonov regularized version of the NMF is also proposed to overcome the problem of non-uniqueness in the NMF based spectral unmixing [174]. These approaches consider every band independently without considering dependencies across the spectral space.

In this chapter, we present a regularization-based approach to achieve the constrained unmixing, as recommended in [72, 175] to obtain better solution for an ill-posed problem. For this purpose, a Tikhonov regularization approach is formulated in the TLS framework for estimating the abundance maps. A theoretical analysis is carried out to further explain the significance of the proposed method. We also include the discussion on role of regularization in solving the unmixing problem.

3.2 Problem Formulation

In the linear model assumption, each measured spectrum of a scene is treated as a spectral data vector ($\mathbf{r}$) across the contiguous wavelength bands. It can be approximated as a linear combination of the endmembers ($\mathbf{M}$),

$$\mathbf{r} \approx \mathbf{M}\boldsymbol{\alpha}. \tag{3.1}$$

In the unmixing problem, the data $\mathbf{r}$ and endmember matrix $\mathbf{M}$ are known, and the task is to obtain abundance vector $\boldsymbol{\alpha}$ for every location in the hyperspectral data. In general, the linear model (3.1) can be rewritten as

$$\mathbf{r} = \mathbf{M}\boldsymbol{\alpha} + \mathbf{n}. \tag{3.2}$$

Here, $\mathbf{n}$ represents additive white Gaussian noise (AWGN). The spectral measurement $\mathbf{r} \in \mathrm{I\!R}^{+W}$ denote a W-dimensional column vector, where, W is total number the contiguous wavelength bands. The fractional abundances are expected to satisfy $\alpha_i \geq 0, i = 1, ..., e$ (nonnegatively constrained abundances) and $\sum_{i=1}^{e} \alpha_i = 1$ (sum-to-one constrained abundances). Therefore, the data cube is assumed to be in the $(e-1)$- simplex in $\mathrm{I\!R}^{+W}$.

It should be noted that if the spectral signature values (endmembers) are perturbed then the least squares estimate of $\boldsymbol{\alpha}$ is not accurate. Taking the singular-value decomposition of $\mathbf{M} = \mathbf{U\Sigma V^T} = \sum_{\mathbf{i=1}}^{\mathbf{k}} \mathbf{u_i}\sigma_\mathbf{i}\mathbf{v_i^T}$, where $k(\leq e)$ is the rank of the $\mathbf{M}$ matrix, the least squares estimates for (3.2) is shown to be

$$\hat{\boldsymbol{\alpha}}_{\mathbf{LS}} = \sum_{\mathbf{i=1}}^{\mathbf{k}} \frac{\mathbf{u_i^T r}}{\sigma_\mathbf{i}} \mathbf{v_i}. \tag{3.3}$$

It is observed from equation (3.3) that due to the perturbed $\mathbf{M}$ matrix, the LS estimates of $\boldsymbol{\alpha}$ are noisy. Hence, given the noisy data and the perturbed endmember matrix, finding the abundances is a severely ill-conditioned problem. Use of prior information on $\boldsymbol{\alpha}$ can improve the solution. Therefore, regularization framework for abundance estimation is used in this proposed technique.

3.3 Role of Regularization in Unmixing Hyperspectral Data

As discussed in Chapter 1, Section 1.3.2, the unmixing of hyperspectral data is an ill-posed inverse problem. This results in multiple solutions for the same problem and it becomes difficult to obtain a unique solution. When the problem is ill-posed, the regularization is an effective way to restrict the solution space. The use of regularization not only helps in better restricting the solution space but it also improves the solution under noisy situations [72, 175]. This can be achieved by introducing additional information about the final solution to handle the wide range of possible solutions. Such algorithms have been successfully attempted and implemented for various problems that use hyperspectral data. Since the hyperspectral imagery is represented as a data cube, the major issues in finding a regularized unmixing are, 1) deciding the domain of regularization, i.e., spatial or spectral, 2) the kind of prior information, i.e., choosing appropriate prior model to yield a better solution, and 3) finding the regularization parameter(s) without using the true entity which is to be estimated.

3.3.1 Spatial regularization

Considering a prior in the image-domain of the data cube can be considered as the spatial regularization. This assumes a prior on the entity to be estimated over each of the band images without considering the spectral coherence in the data. This is likely to occur under the fact that the abundances are similar in the neighborhood area of the scene, and hence the abundances have been mostly modeled in the spatial domain using various priors while unmixing the scene. Such methods include Gaussian prior [134], Gibbs prior [133], fuzzy model [132], and neural-network based approaches [176]. Recently, sparsity induced regularization approaches have been investigated using the fact that the number of spectrally distinct signatures is significantly lesser than the number of bands in the data [156]. However, it should be noted that all these methods use the least-squares (LS) as their data-term while regularizing with different priors in the spatial domain.

3.3.2 Spectral regularization

Spectral regularization is when a prior information is incorporated across the spectral space of the data. This is based on the fact that the hyperspectral data is been envisioned for recording a spectral signature of various materials found on the earth and/or other planetary objects such as the moon. The high-dimensional spectral data has a natural coherence in the spectral range of the reflectance. This enables the characterization and quantification of the materials found even in the physically inaccessible areas. The spectral regularization exploits these dependencies in the data by imposing a prior across the spectral space (may be at each location), unlike the spatial regularization over many nearby pixels in the scene.

In many of the cases in practical scenario, one has to perform the unmixing using perturbed endmembers and the cluttered data. This has been more often the case in target and/or anomaly detection in hyperspectral data [177, 178, 179]. Hence, there is a need to explore the TLS framework. Considering the severity in the ill-posedness of the problem, we investigate the spectral regularization within the TLS framework.

3.4 Unmixing Using Spectral Regularization Approach in TLS Framework

The problem of obtaining the unmixed images (abundance maps) from the noisy data cube can be better-posed by using Tikhonov regularization within the TLS framework. While solving for the $\boldsymbol{\alpha}$, TLS estimation for the linear model (3.2) can be formulated as

$$\begin{aligned} (\mathbf{r}+\mathbf{n}) &= (\mathbf{M}+\mathbf{N})\,\boldsymbol{\alpha} \\ \tilde{\mathbf{r}} &= \widehat{\mathbf{M}}\boldsymbol{\alpha}. \end{aligned} \tag{3.4}$$

Here $\mathbf{n}$ and $\mathbf{N}$ represent independent and identically distributed (IID) Gaussian noises. A basic TLS solution [180] is obtained by minimizing the following Frobenius norm

$$\arg\min_{\forall\boldsymbol{\alpha}} \left\| [\mathbf{M};\mathbf{r}] - \left[\widehat{\mathbf{M}};\tilde{\mathbf{r}}\right] \right\|_{\mathbf{F}}, \tag{3.5}$$

$$\textbf{s.t.:}\ \tilde{\mathbf{r}} = \widehat{\mathbf{M}}\boldsymbol{\alpha}.$$

The TLS is similar to finding the slope and intercept of a straight line, i.e., fitting a line $y = mx + c$, and the problem of TLS corresponds to estimating m and c considering that both the observation y and measurement x are in error. In our case, the TLS (3.5) takes care of the noise in both $\mathbf{r}$ and $\mathbf{M}$, and is equivalent to the minimum norm solution [181]. See that it does not consider any additional information on the unknown. However, the problem is still ill-posed mainly due to existence of multiple solutions for the abundances. Thus, the TLS equation (3.5) leads to noisy solution for abundance maps. Hence, we propose a solution based on the spectral regularization using the TLS with the Tikhonov prior term, i.e.

$$\hat{\boldsymbol{\alpha}}_{(\boldsymbol{i},\boldsymbol{j})} = \arg\min_{\forall \boldsymbol{\alpha}} \left[\underbrace{\left\| \left[\mathbf{M}; \mathbf{r}_{(i,j)}\right] - \left[\widehat{\mathbf{M}}; \widehat{\mathbf{M}}\boldsymbol{\alpha}_{(i,j)}\right] \right\|_F}_{\text{TLS data-term}} + \underbrace{\mu \left\| \mathbf{L}\boldsymbol{\alpha}_{(i,j)} \right\|_2}_{\text{Spectral prior}} \right], \forall\, i, j \tag{3.6}$$

where, μ is the regularization parameter, and $\mathbf{L}$ is matrix representation of the derivative operator. The data-term in the equation (3.6) accounts for the problem as formulated in (3.4), while the Tikhonov prior is regularizing the solution by imposing the smoothness requirement. Since the objective function in (3.6) is convex, it is conveniently minimized by gradient-descent optimization technique. The value of μ is set by using the empirical approach. While minimizing using (3.6), the $\hat{\boldsymbol{\alpha}}$ is restricted to lie between 0 and 1 to obtain physically acceptable abundances. It is clear that the estimation process is carried out for every pixel location using the respective spectral data vectors as indicated in (3.6). Finally, this process yields the estimated unmixed images for the given endmembers of the scene.

3.5 Theoretical Analysis of TLS-Tikhonov regularization approach

In this section, we theoretically analyze the proposed regularization-based approach and compare it with both TLS-based direct inversion used in [129] and the truncated TLS solution [182] in which the abundances are obtained by regularizing the eigenvalues of the endmember matrix.

With the $\tilde{\mathbf{r}}$ and $\widehat{\mathbf{M}}$ in (3.5), the combined matrix $[\widehat{\mathbf{M}}; \tilde{\mathbf{r}}]$ becomes *numerically* rank-deficient [100]. The singular-value decomposition results in $\widehat{\mathbf{M}} = \hat{\mathbf{U}}\hat{\boldsymbol{\Sigma}}\hat{\mathbf{V}}^{\mathbf{T}} = \sum_{\mathbf{i}=\mathbf{1}}^{\mathbf{k}} \hat{\mathbf{u}}_{\mathbf{i}}\hat{\sigma}_{\mathbf{i}}\hat{\mathbf{v}}_{\mathbf{i}}{}^{\mathbf{T}}$. Then the solution proposed in (3.6) regularizes the solution iteratively to [182]

$$\hat{\alpha} = \sum_{\mathbf{i}=\mathbf{1}}^{\mathbf{k}} \frac{\hat{\sigma}_{\mathbf{i}}{}^{\mathbf{2}}}{\hat{\sigma}_{\mathbf{i}}{}^{\mathbf{2}} + \mu^{\mathbf{2}}} \frac{\hat{\mathbf{u}}_{\mathbf{i}}{}^{\mathbf{T}}\tilde{\mathbf{r}}}{\hat{\sigma}_{\mathbf{i}}} \hat{\mathbf{v}}_{\mathbf{i}}. \tag{3.7}$$

Here, it can be seen from the equation that the regularization is suppressing the effects of smaller singular values in $[\widehat{\mathbf{M}}; \tilde{\mathbf{r}}]$. Hence, the proposed approach achieves a better solution when compared to the TLS formulation. Thus, this regularization approach improves the solution proposed in [129].

Now, if these smaller singular values are made zero than the numerically rank-deficient problem (with the rank $k+1$) can be converted into an exactly rank-deficient problem (with a rank $l < k+1$). The process of making the smaller singular values to zero leads to the truncated TLS solution [182]. But, the truncated TLS depends heavily on the number of singular values forcibly converted to zeros by trial & error method. Note that this truncated TLS solution is different from the proposed regularization approach, since the proposed approach depends on the choice of regularization parameter. It is iteratively minimizing the equation (3.6) and hence converges to the near optimal solution.

3.6 Experimental Analysis

The experiments are conducted on the simulated data constructed using the three spectral signatures of the US Geological Survey digital spectral library[1]. The results are compared with the existing approaches based on the TLS framework [129, 130]. Note that the comparison with the LS based approaches like FCLS [122] and MaxEnt [126] are avoided since they solve a different problem. Finally the abundance maps of the real data collected by the Airborne Visible/InfraRed Imaging Spectrometer (AVIRIS) over the Indian Pines are estimated and validated by computing the data reconstruction error at every location of the entire scene.

3.6.1 Experiments with simulated data

The reflectance spectra, representing the endmembers' signatures of Ammonioalunite NMNH145596, Brucite HS247.3B and Andradite WS487 from the USGS library database [85] are used to construct the 224-band simulated hyperspectral data. The signatures representing the vectors, yield a size of 224×3 for the $\mathbf{M}$ matrix. Using the $\mathbf{M}$ and known abundance vector ($\boldsymbol{\alpha}$) of size 3×1, a reflectance vector $\mathbf{r}$ of size 224×1 is constructed. Now, keeping the $\mathbf{M}$ fixed and for different known proportions of $\boldsymbol{\alpha}$, 224 images each of size 75×75 pixels are constructed. Figure 3.1 (a) shows the mean image of size 75×75 pixels of the simulated hyperspectral datacube ($75 \times 75 \times 224$). The locations corresponding to the endmembers (pure pixels) are marked with yellow dots over the

---

[1] `http://speclab.cr.usgs.gov/spectral-lib.html`

mean image while their signatures (i.e., endmember values in each band) are plotted in Figure 3.1 (b).

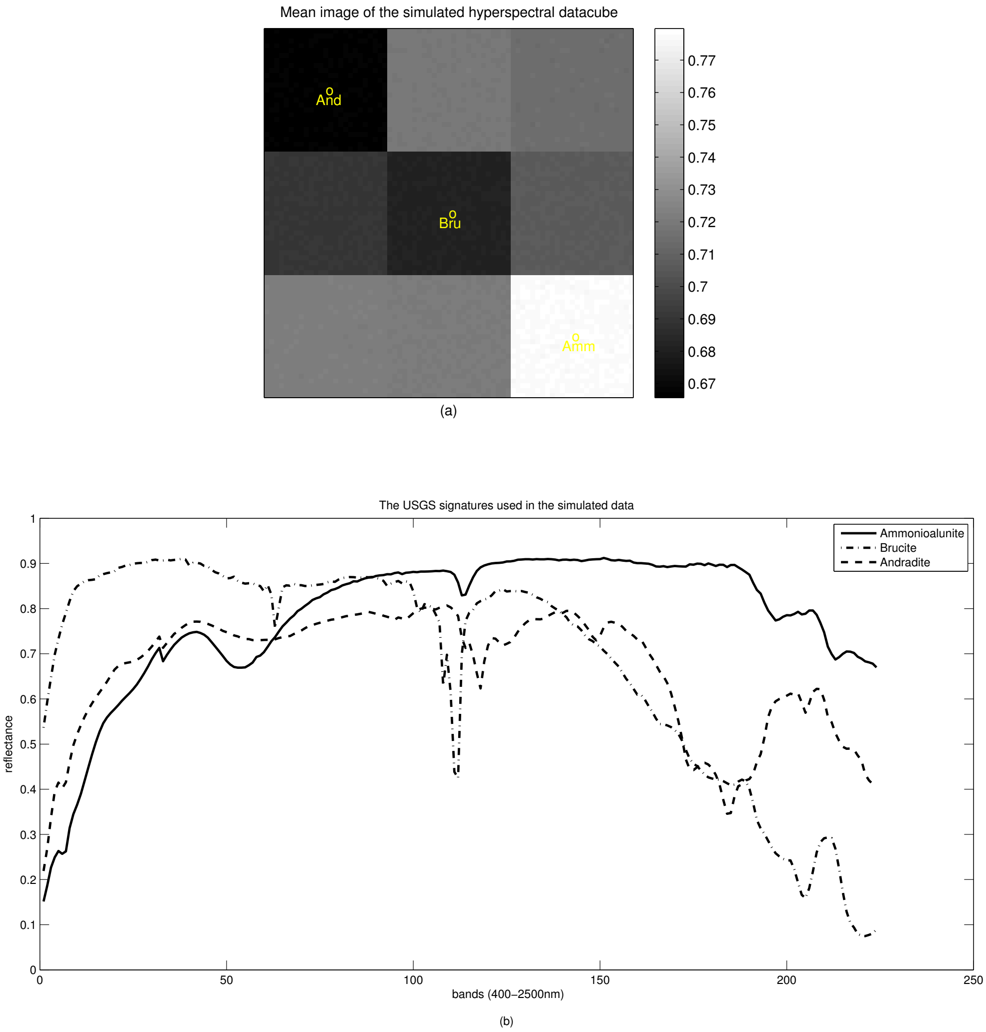

(a)

(b)

Figure 3.1: Simulated hyperspectral data: (a) mean image of the simulated datacube (‘And’, ‘Bru’ and ‘Amm’ stands for Andradite, Brucite and Ammonioalunite, respectively), and (b) the three spectral signatures used to construct the simulated data cube.

The ground truth abundance maps, each of size 75 × 75 pixels, for the three endmembers are shown in Figure 3.2 (a). Now, for the purpose of testing and comparison, the abundances are considered to be unknown; They are estimated for different values of the AWGN in both the $\mathbf{r}$ and $\mathbf{M}$, using the proposed regularization approach as well as using the TLS [129] and the restricted TLS (R-TLS) [130]. For acceptable unmixing, the amount of noise added to $\mathbf{M}$ is constrained such that the signal-to-noise ratio - spectral distortion (SNR-SD) for each of the spectral signatures of the resultant matrix $\widehat{\mathbf{M}}$ is satisfied [5]. First the consistency in the spatial abundance patterns in the estimated abundance maps are perceptually verified by comparing them with the ground truth abundance maps. The estimated abundance maps considering a worst-case scenario (20 dB SNR in the **r** with -6 dB noise in the **M**) using the TLS, the R-TLS and with the proposed TLS-Tikhonov approach are depicted in Figures 3.2 (b) to 3.2 (d), respectively. It can be clearly seen from Figure 3.2 (d) that the spatial distribution of the abundances is well preserved when compared with the ground truth maps (see Figure 3.2 (a)).

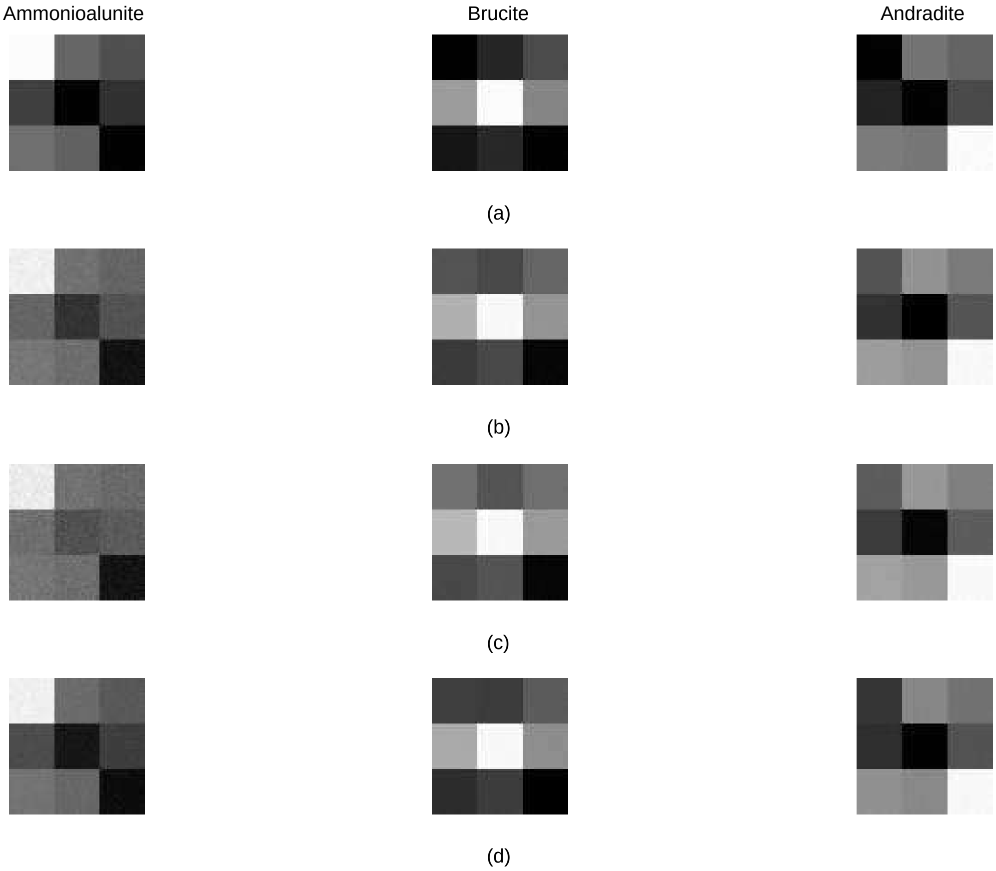

Figure 3.2: Abundance maps for simulated data: (a) The ground truth maps. Estimation using (b) TLS [129], (c) R-TLS [130], and (d) proposed TLS-Tikhonov approach [131]. Note that all the estimated maps are obtained for the 20 dB SNR data with -6 dB noise in the endmember matrix.

The performance of the proposed approach is tested for increasing levels of noise in both the data and endmembers. Quantification of the error is carried out using the root mean-squared error (RMSE) [106], spectral angle mapper (SAM) [107] and spectral information divergence (SID) [108], which are calculated between the ground truth abundances and the estimated abundances using different approaches. Due to nonavailability of a regularization based unmixing within the TLS framework, we compare our approach

Table 3.1: Noise Sensitivity Analysis of the Simulated Data Unmixing. Average error scores using TLS, restricted TLS (R-TLS) and the proposed TLS-Tikhonov approach.

Algorithm	TLS [129]	R-TLS [130]	proposed TLS-Tikhonov [131]
	RMSE [106]		
Case 1	0.036	0.029	**0.008**
Case 2	0.147	0.156	**0.059**
Case 3	0.263	0.265	**0.253**
Case 4	0.274	0.275	**0.268**
	SAM [107]		
Case 1	10.365	9.472	**2.583**
Case 2	12.485	12.869	**7.473**
Case 3	30.781	25.453	**25.401**
Case 4	31.383	26.284	**26.182**
	SID [108]		
Case 1	0.012	0.054	**0.004**
Case 2	0.124	0.153	**0.031**
Case 3	0.291	0.248	**0.224**
Case 4	0.312	0.279	**0.252**

Case 1: 1000 dB SNR data $\tilde{\mathbf{r}}$; -6 dB noise matrix $\widehat{\mathbf{M}}$
Case 2: 200 dB SNR data $\tilde{\mathbf{r}}$; -6 dB noise matrix $\widehat{\mathbf{M}}$
Case 3: 50 dB SNR data $\tilde{\mathbf{r}}$; -6 dB noise matrix $\widehat{\mathbf{M}}$
Case 4: 20 dB SNR data $\tilde{\mathbf{r}}$; -6 dB noise matrix $\widehat{\mathbf{M}}$

with the TLS based methods [129, 130] which do not consider the regularization. The unmixing using the basic TLS formulation is carried out in [129], however, the physical constraints on the abundances are incorporated in [130]. These methods consider the noise in both the endmembers and data while we use an additional constraint in terms of Tikhonov prior on the abundances that restrict the solution space making the problem better-posed and hence improve the estimation accuracy. The parameter μ can be chosen empirically if the application is not time-critical. However, μ can be estimated by using the approaches such as generalized cross-validation method [183]. Table 3.1 shows the average error scores using TLS based approaches [129, 130] and using the TLS-Tikhonov regularization based approach [131]. The average values are calculated over all the abundance maps. In this case, it is averaged over the $75 \times 75 \times 3$ values estimated by an approach. One can see that the proposed approach performs significantly better when compared to the other methods.

3.6.2 Experiments on real data

In this subsection, we demonstrate the performance of the proposed approach on the Indian Pine site data [184] collected by the AVIRIS. The data is collected in 220 contiguous bands ranging from 400-2500 nm with spectral resolution of 10 nm. The size of each band is 145 × 145 pixels with each pixel covering an area of $20m \times 20m$. As per the ground truth information [184] and as indicated by the false-color composition of the mutually exclusive ground cover classes in [7], we considered 16 endmembers for the scene. Using this data, we first obtain the endmembers using the vertex component analysis (VCA) algorithm [102] which is considered to be a state-of-art approach. Figure 3.3 shows the final 16 abundance maps obtained by using the proposed TLS-Tikhonov approach [131].

The quantification of the error is done by reconstructing the reflectance using the estimated abundances and measuring the error in reconstruction by taking square of the difference between the available and the reconstructed reflectance. We call this as data reconstruction error (DRE). Figure 3.4 shows the available and the reconstructed images of bands 50, 125 and 200 using the TLS, R-TLS and the proposed approach. The observed bands are shown in Figure 3.4 (a). Reconstructed bands using the abundances estimated by TLS method and by R-TLS approach are shown in Figure 3.4 (b) and Figure 3.4 (c), respectively. Figure 3.4 (d) displays the reconstruction using the abundance maps estimated by the proposed TLS-Tikhonov approach. Visual inspection of the reconstructed images clearly indicates that the proposed approach gives the reflectance closer to the available one (see Figure 3.4 (a) and Figure 3.4 (d)).

In Figure 3.5 we display the data reconstruction error (DRE) maps by computing the RMSE at each pixel location between the available and the reconstructed reflectance for different approaches. Figure 3.5 (a) and Figure 3.5 (b) show the DRE maps obtained for the TLS and R-TLS approaches, respectively. Finally, Figure 3.5 (c) displays the DRE map for the proposed TLS-Tikhonov approach. Comparing these maps, one may say that TLS method and the proposed approach are the best performers in terms of reducing the RMSE. However, the proposed approach is better when compared to the TLS method, since it minimizes the average error while reducing the standard deviations, indicating better estimation of abundances over the entire data cube.

In order to further clarify the performance improvement, we compute the SAM values

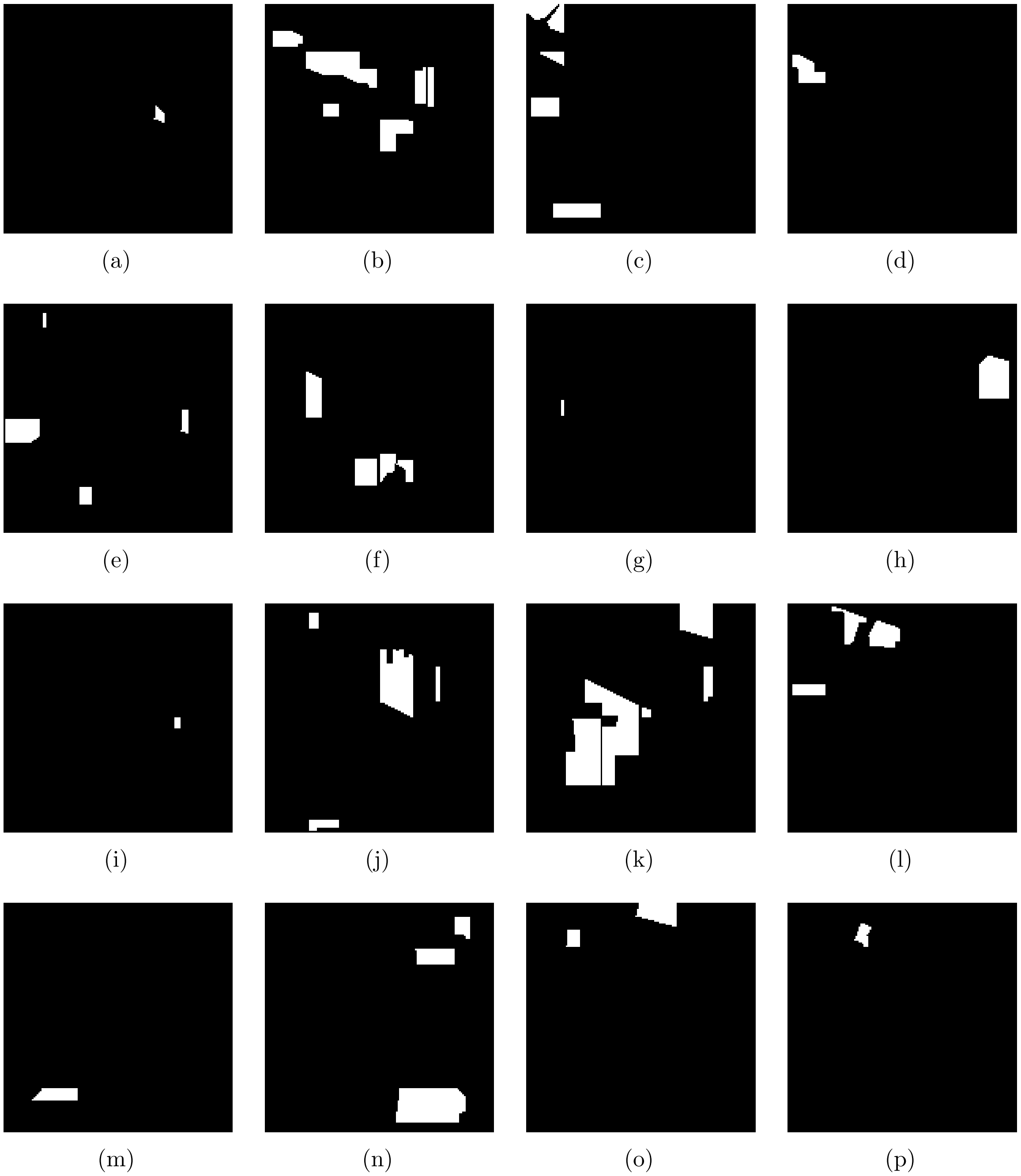
(a) (b) (c) (d)

(e) (f) (g) (h)

(i) (j) (k) (l)

(m) (n) (o) (p)

Figure 3.3: Abundance maps estimated using the proposed TLS-Tikhonov approach [131] for the Indian Pines data: (a) Alfalfa, (b) Corn-notill, (c) Corn-min, (d) Corn, (e) Grass/Pasture, (f) Grass/Trees, (g) Grass/Pasture-mowed, (h) Hay-windrowed, (i) Oats, (j) Soybeans-notill, (k) Soybeans-min, (l) Soybeans-clean, (m) Wheat, (n) Woods, (o) Building-Grass-Trees, and (p) Stone-steel-towers.

for the TLS method and the proposed approach, and display their DRE maps in Figure 3.6. Unlike the RMSE, the SAM indicates the angular difference between the available and the reconstructed reflectance over the scene across the spectra. Figure 3.6 (a) shows the DRE maps in terms of SAM for the TLS method while in Figure 3.6 (b) we display

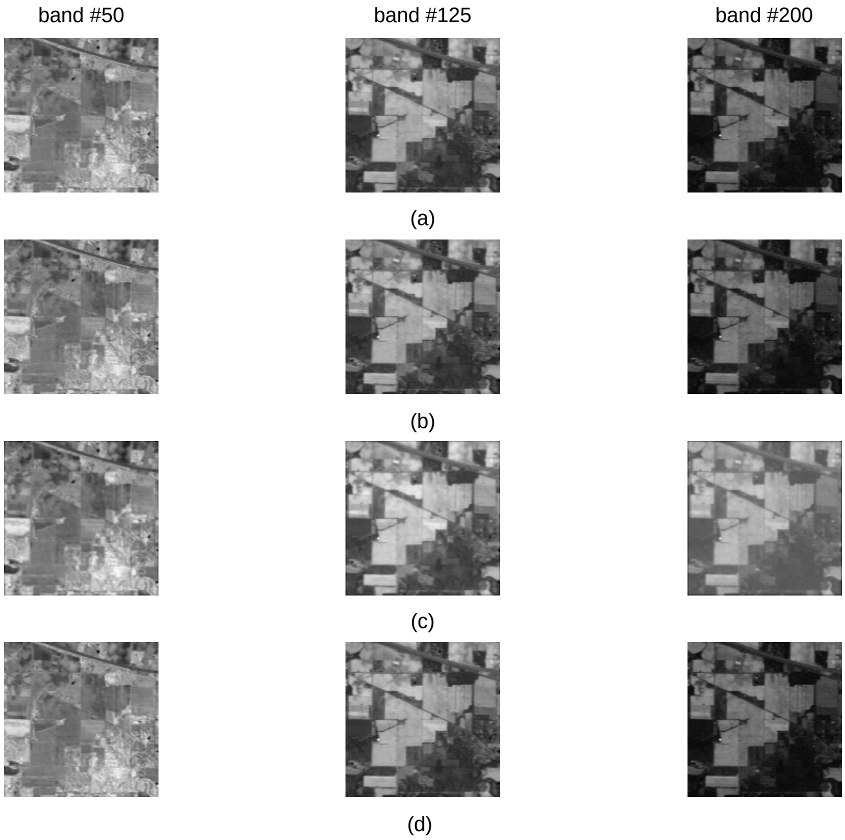

Figure 3.4: Spectral bands 50, 125 and 200 of AVIRIS Indian Pines data: (a) observed bands of the scene, reconstructed bands using abundances estimated using (b) TLS method [129], (c) R-TLS [130], and (d) proposed TLS-Tikhonov approach [131]. The spectral contents in different bands are consistent in the reconstructed scene using the proposed approach.

the same for the proposed approach. It is clear from the figure that the proposed has lesser angular differences and hence it better preserves the variations in the estimated abundances. This further validates the effectiveness of the proposed TLS-Tikhonov in solving the unmixing problem.

By conducting experiments on the simulated data by using different μ values in the proposed approach, and verifying the data reconstruction errors in terms of RMSE, we found that the performance of our approach was optimum for $\mu = 0.01$. We reiterate here that one may use the generalized cross validation (GCV) technique [183], and estimate the regularization parameter μ. However GCV is computationally expensive and we refrain from doing the same in our approach.

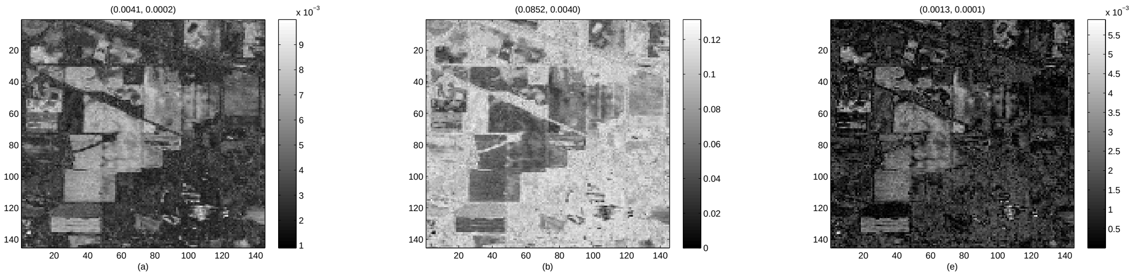

Figure 3.5: DRE maps (in terms of RMSE) for the AVIRIS Indian Pines data: DRE map using (a) TLS method [129], (b) R-TLS approach [130], and (c) proposed TLS-Tikhonov approach [131]. The average errors and their standard deviations are mentioned in parenthesis on the top of each figure. The performance of the proposed approach is better in terms of RMSE as well as preservation of abundances variance.

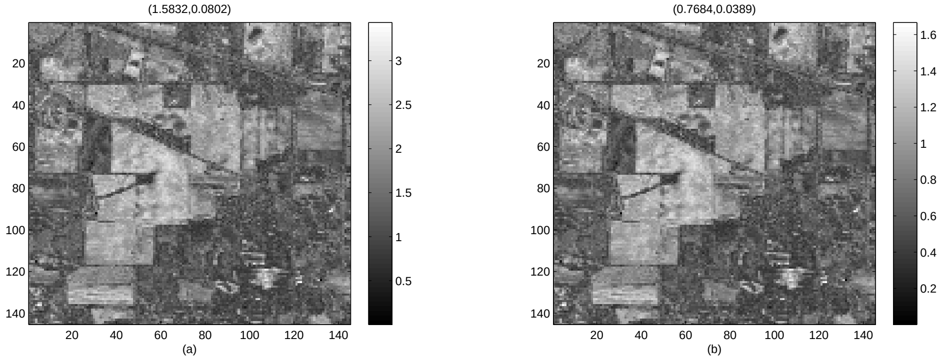

Figure 3.6: DRE maps (in terms of SAM) for the AVIRIS Indian Pines data: DRE map using (a) TLS [129] method, and (b) proposed TLS-Tikhonov approach [131]. The average errors and their standard deviations are mentioned in parenthesis on the top of each figure. This comparison excludes the R-TLS [130], since the TLS [129] method and the proposed approach [131] outperform it in terms of RMSE (see Figure 3.5).

3.7 Conclusions

Considering the widely accepted linear mixing model, the physical inversion problem of unmixing is difficult for the mixed data. It needs regularization for improving the solution. In this chapter, we have presented an approach to arrive at a better solution by using the Tikhonov regularization within the TLS estimation framework. We consider the case when the imaging spectrometer data has outliers which in turn lead to errors in endmembers and subsequently affect the unmixing. The improved estimation of abundances can be of use in many applications specifically in target detection [179] and tracking [185, 186].

Note that the problem of abundance estimation is ill-posed even when one has the ground truth endmembers. This problem is analyzed in the next chapter and a novel approach is proposed to overcome the same.

Chapter 4

A Data-driven Stochastic Approach for Unmixing Hyperspectral Imagery

In this chapter, we propose a novel approach for unmixing in which the required parameters in the prior model are estimated using the given data itself. For this purpose, we propose a two-step Bayesian approach that handles the ill-posed nature of the unmixing problem. We use the fact that the abundances are data dependent and they represent mixing proportions of the endmembers over an area. A linear mixing model is used for the image formation process in order to derive the data term. In the first step, an initial estimate of abundances is obtained using using the matched filters based approach. Assuming a Huber-Markov random field (HMRF) based prior on the abundances, we derive the threshold (prior parameter) in HMRF using the initial estimate. This makes the HMRF prior data dependent or data-driven and it helps in improving the accuracy of abundance estimation. Final abundance maps are obtained in the second step by using a maximum *a posteriori* (MAP) approach in which the prior term has data-driven HMRF (*d*HMRF). The resultant objective function is optimized using the particle swarm optimization (PSO) that ensures the global convergence. Here also the theoretical analysis is carried out to show the effectiveness of the proposed method. The approach is evaluated qualitatively as well as quantitatively by using the synthetic as well as real AVIRIS Cuprite data. The proposed method has the following advantages: 1) The estimated abundances are resistant to noise since they are based on an initial estimate that has high signal-to-noise ratio (SNR). 2) The variance in the abundance maps is better preserved since the threshold in the *d*HMRF is derived from the data itself.

4.1 Introduction

Accurate estimation of abundances is important for many applications in hyperspectral remote sensing. Few of these applications include hyperspectral image classification[7], content-based image retrieval system [13, 14], target detection [187], precision agriculture [16] and image fusion [188]. An accurate estimate of the abundance leads to better outcome in these applications. On the other hand, accurate abundances also lead to improved endmembers, since together they yield a pixel value (reflectance) in the data. As a matter of fact, in [158] the abundances have been used in finding the endmembers.

According to the linear mixing model (LMM) [38] of the hyperspectral data, the abundances are fractions of areas covered by the endmembers representing the pure spectra found in the data. Though the LMM is predominantly used in the remote sensing, the linear stochastic mixing model (SMM) [70] for the hyperspectral data has been developed by integrating the principles of spectral clustering with the LMM, and its convergence issues are discussed in [71]. The SMM is also a kind of linear model since it assumes that the data is linear combinations of the endmembers, however, it considers the data in statistical manner by modeling the signatures in probabilistic sense rather than as deterministic spectra as in LMM. Though SMM offers the generalization, it has to handle an additional challenge of estimating the model parameters while solving for the spectral unmixing [72]. It has been recommended to explore random-field modeling to solve the problem and to develop the algorithms integrating the spatial and spectral information of the hyperspectral data [5, 87, 86].

Knowing the endmember matrix, the given data can be unmixed by finding the corresponding abundances at each location over the scene. Since the abundances represent the endmembers fractions, they are constrained by nonnegativity as well as sum-to-one at each location. The unmixing approaches can be broadly categorized into constraint-energy-minimization (CEM) [117], unconstrained regularization [119], maximum-likelihood (ML) [74], stochastic expectation maximization (SEM) [189], and neural network based approaches such as [176]. Majority of the research on abundance estimation is based on the ML estimation [121, 168]. Among the other approaches, fully constrained least-squares (FCLS) abundance estimation [122] is a well-known approach that represents generalization of the least-squares formulation. The methods based on the SMM are discussed in [70, 71]. In [190], a modified SEM is proposed for enhancing the unmixing performance. Authors in [129, 130] proposed unmixing based on total least squares (TLS) approach that restricts the solution to physically constrained abundances. In our recent work [131], we proposed a Tikhonov regularization based approach formulated in the TLS framework. A nonnegative solution using the principles of maximum entropy has been proposed in [124, 125] and [126]. In [170, 171, 161, 172, 127] the approaches based on Markov chain Monte Carlo method have been investigated. In addition to the nonnegativity, these methods also incorporate the sum-to-one constraint on the solution but they suffer from high computational complexity. Many of the methods proposed in the literature use different kind of priors for modeling the spatial correlation of the abundances [132, 133, 134]. These approaches consider every band independently without considering dependencies across the spectral space. In this chapter, we propose a MAP-HMRF model based approach by considering Huber prior for the abundances over the spectral space.

A region in a scene has different proportions of mixing depending upon the amount of the constituent materials. Further, a pixel in the hyperspectral data represents reflectance spectra acquired from a large area (typically one pixel represents $20m \times 20m$) and hence it invariably forms mixed pixel at almost every location in the scene. The mixing proportions (i.e., abundances) vary at each location and the challenge is to capture these variations under the noisy conditions. Hence there is a need to individually unmix each location in order to obtain better estimate of abundance maps. The unmixing carried out at every location across the scene preserves correlatedness of the abundances both spatially and spectrally. It may also be treated as special instance of the piecewise processing of data mentioned in [5]. This has motivated us to model the abundance dependencies at each location as Huber-MRF across the spectral range of the data. Depending on the chosen threshold, Huber function [191] simultaneously preserves smoothness and discontinuity within the abundances across the spectral space.

A better way to find the Huber threshold is by using the true abundances, but these are unknown and are to be estimated. In order to estimate the threshold, one may consider using the learning based approach which requires a large hyperspectral data set. Hence deriving an accurate threshold using the training data set is computationally intensive. Moreover, one cannot generalize the use of such learned threshold for representing the dependencies of the abundances in any data. Since the abundances to be estimated are dependent on the given data, it is desirable to estimate the threshold using the available data itself, which can be used in the HMRF prior to achieve an accurate estimation of abundances.

Inspired from this, we automate the process of threshold selection based on an initial estimate of abundances obtained using the available data. Hence the resultant prior *d*HMRF now depends on the data, yielding accurate abundances. A matched filter [192, 193, 96, 194] based approach, inspired from the signal processing and communication theory is employed to obtain the initial estimate of abundances. The abundances derived using the matched filters act as a good approximation to represent the global characteristics of the true abundances. Hence, they can be used in obtaining the required threshold which in turn leads to improvement in the accuracy of estimated abundances. Thus the proposed approach obviates the training data resources to derive the threshold and gives abundances which minimize the data reconstruction error. In practice, the regularization parameter may be estimated by using generalized cross validation techniques [183]. However, this is computationally expensive and also the derived parameter is image dependent. Instead the use of proposed *d*HMRF prior helps in fixing the regularization parameter that further reduces the time complexity.

Considering the research in the spectral unmixing problem, we observe that the abundance estimation is relatively less focused when compared to the extraction of endmembers. Efforts have been made to incorporate the physical constraints (i.e., nonnegativity and sum-to-one) while estimating the abundances. However, the presence of noise and outliers make the unmixing process severely ill-posed and hence it becomes difficult to obtain a unique solution. Many approaches estimate the abundances considering the spatial correlatedness but the variations of the abundance values across the spectral bands are not addressed. We explore the fact that the hyperspectral data is acquired over narrow and contiguous bands, which makes it spectrally correlated. The proposed *data-dependent* abundance prior over the spectral range of the data takes care of preserving the sudden variations as well as homogeneity in the abundances.

Figure 4.1 shows the complete block schematic of the proposed method. Given the hyperspectral data and the number of endmembers (e), we use the spectral library of the data to construct the endmember matrix ($\mathbf{M}$). We then employ matched filters, one for each endmember and obtain initial estimate of the abundance maps. Once the initial estimate is available, it is used to derive the histogram of magnitude of gradients of these estimates using the gradients at every location. This histogram indicates the variations among the abundances. A suitable value of threshold β for Huber-MRF is then derived from this histogram, and is used in the next step. An energy function formed using the data term and the *d*HMRF prior with the estimated β is minimized to obtain the final solution.

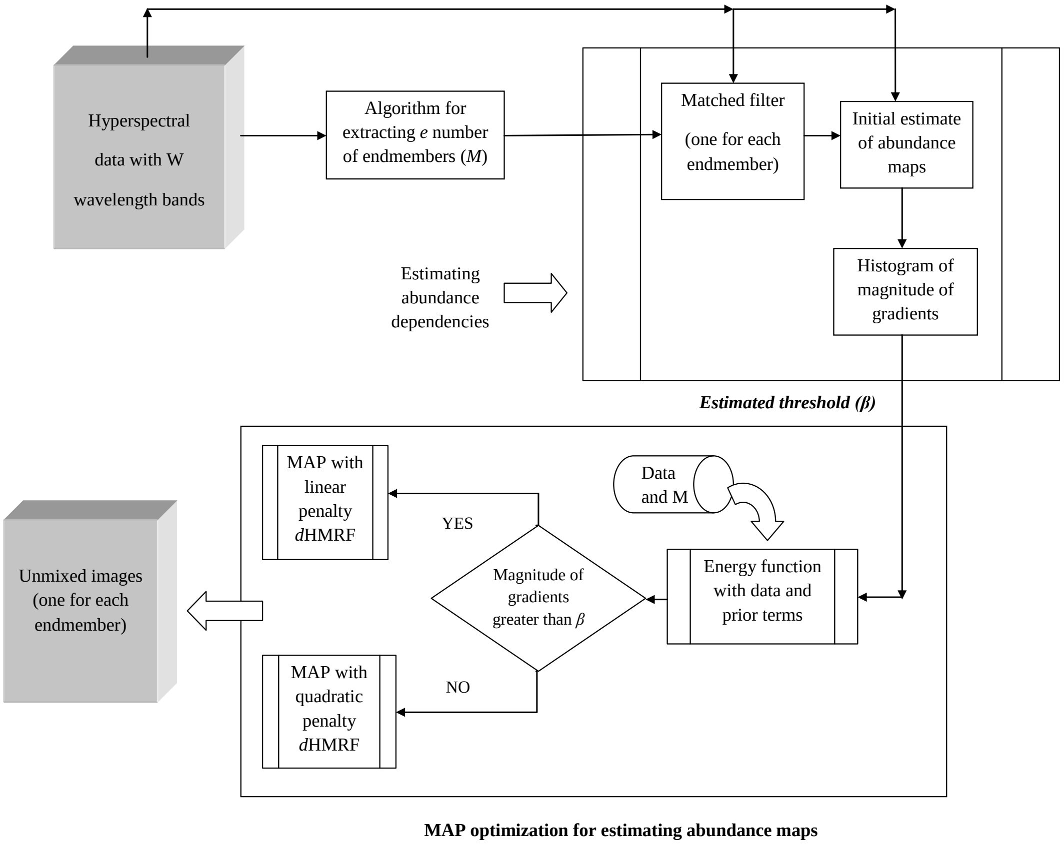

Figure 4.1: Block schematic of the proposed MAP-*d*HMRF approach.

4.2 Hyperspectral Image Formation Model

The hyperspectral imager acquires hundreds of contiguous spectral measurements of an area. The data can be modeled as either linear or nonlinear mixing of the spectral signatures of various materials found in the area. We consider a linear mixing model at each location under the additive white Gaussian noise scenario as

$$\mathbf{r} = \mathbf{M}\boldsymbol{\alpha} + \mathbf{n}, \tag{4.1}$$

where the spectral measurement $\mathbf{r}$ and the noise $\mathbf{n}$ are W-dimensional column vectors with W indicating the number of available contiguous bands. Here, the endmember matrix $\mathbf{M}$ representing the spectral signatures and it has size of $W \times e$, with e being the number of endmember vectors. The weights of these endmembers correspond to the abundances and they are denoted as a e-dimensional vector $\boldsymbol{\alpha} = [\alpha_1, \alpha_2, ..., \alpha_e]^T$ where, α_i represents the fractional area covered by the i^{th} endmember, for $i = 1, 2, ..., e$.

In the linear model given by equation (4.1) both $\mathbf{M}$ and $\boldsymbol{\alpha}$ are unknown. In the proposed work, the $\mathbf{M}$ is constructed using the ground truth spectral signatures and hence the problem returns to estimating the abundance maps, given both the $\mathbf{M}$ and $\mathbf{r}$. In practice the number of endmembers (e) are significantly less than the available bands (W) for an acquired area of interest. Hence the equation (4.1) is overdetermined in $\boldsymbol{\alpha}$ making it an ill-posed inverse problem that requires regularization using suitable prior in order to make it a better-posed one. In (4.1), $\mathbf{n}$ represents independent and identically distributed (IID) noise having the joint probability density function (pdf) at a location (across the spectral cube) as

$$\mathbf{P_r}\left(\mathbf{n}\right) = \frac{\mathbf{1}}{\left(\mathbf{2}\boldsymbol{\pi}\boldsymbol{\sigma}^{\mathbf{2}}\right)^{\frac{\mathbf{W}}{\mathbf{2}}}}\mathbf{exp}\left(\frac{-\left\|\mathbf{n}\right\|^{\mathbf{2}}}{\mathbf{2}\boldsymbol{\sigma}^{\mathbf{2}}}\right), \tag{4.2}$$

where $\boldsymbol{\sigma}^{\mathbf{2}}$ represents the noise variance.

4.3 Prior Model

Since we cast the problem in the MAP framework, a suitable prior is required in order to obtain a better solution. The prior has to take care of smoothness (slow variations) as well as discontinuity (sudden variations) of the abundance values. This can be done by choosing a prior that considers dependencies or correlatedness among the abundances. Markov random field (MRF) based model can effectively represent such dependencies. When an abundance map is modeled as an MRF, the abundance values at each location can be expressed as a joint pdf as

$$\mathbf{P_r}\left(\boldsymbol{\alpha}\right)=\frac{1}{Z}\mathbf{exp}\left(-\lambda\sum_{\boldsymbol{W}}\rho\left(\alpha\right)\right). \tag{4.3}$$

Note that equation (4.3) represents an MRF modeling the correlatedness among the abundances at a location. Here Z is the normalization constant that ensures total probability sum to unity and λ is a regularization (weighting) parameter, with $\rho\left(\alpha\right)$ representing the clique potential. The advantage of using MRF is that it represents a general model for quantifying correlatedness (dependencies) in the abundance values. One has the freedom to choose an appropriate clique potential in order to capture the dependencies in a better way. For an entity x modeled as an MRF, Huber has proposed the following clique potential [191],

$$\rho\left(x\right)=\begin{cases}x^2 & \text{if } x\leq\beta,\\ 2|x|\beta-\beta^2 & \text{if } x>\beta.\end{cases} \tag{4.4}$$

Here β denotes a constant called the Huber threshold. It can be seen from the equation (4.4) that depending upon the value of β the Huber-MRF can provide quadratic or linear penalty. By considering ρ as function of finite differences in $\boldsymbol{\alpha}$ at a location, i.e., $\alpha_d=\left|\alpha_i-\alpha_{(i+1\ mod\ e)}\right|$, for $i=0,1,2,...,e-1$, one may write equation (4.4) as

$$\rho\left(\alpha_d\right)=\begin{cases}\alpha_d^2 & \text{if } \alpha_d\leq\beta,\\ 2|\alpha_d|\beta-\beta^2 & \text{if } \alpha_d>\beta.\end{cases} \tag{4.5}$$

Note that if the $\alpha_d\leq\beta$ the smoothness in $\boldsymbol{\alpha}$ is preserved and $\alpha_d>\beta$ indicates that there exists significant difference (discontinuity) among the abundances. Hence, a proper choice of β is required in order to better preserve the gradual as well as sudden variations among the estimated abundances. In the next section, we discuss a method for extracting the β directly from the data based on the histogram of the initial estimate of abundances.

4.4 Deriving Data-dependent Threshold β

In the area of signal processing and communication theory, a matched filter is defined as a filter with an impulse response $h\left(t\right)$ that maximizes the output signal-to-noise ratio

(SNR) for the given input signal $f\left(t\right)$ and is given by

$$h\left(t\right)=kf\left(t_0-t\right), \tag{4.6}$$

where k is a constant and $f\left(t_0-t\right)$ represents the input signal delayed by time t_0.

When using hyperspectral data, the matched filter for a given endmember matrix is defined as [195]

$$\mathbf{MF_i}=\frac{\mathbf{\Sigma^{-1}}\left(\mathbf{m_i}-\overline{\mathbf{R}}\right)}{\left(\mathbf{m_i}-\overline{\mathbf{R}}\right)^{\mathbf{T}}\mathbf{\Sigma^{-1}}\left(\mathbf{m_i}-\overline{\mathbf{R}}\right)}, \text{for } i=1,2,...,e, \tag{4.7}$$

where, $\mathbf{MF_i}$ stands for a W-dimensional matched filter vector for the i^{th} endmember and the corresponding signature $\mathbf{m_i}$ of size $W\times 1$. Here $\overline{\mathbf{R}}$ and $\mathbf{\Sigma}$ represent the sample mean vector and the covariance matrix of size $W\times 1$ and $W\times W$, respectively. Projecting the mean-subtracted endmember signature on the inverse of the data covariance $\mathbf{\Sigma}^{-1}$ indicates how well the endmember signature is correlated with the data. Matched filter output is then obtained by dividing the resultant product with the Mahalanobis distance [196] between the projected endmember signature and the data. Normalized $\mathbf{MF_i}$ indicates the contribution of i^{th} endmember signature in the data.

Now using equation (4.7), one can obtain the initial estimate of the corresponding abundance $\hat{\alpha}_{init_i}$ as

$$\hat{\alpha}_{init_i}=\left\langle \mathbf{r}-\overline{\mathbf{R}},\mathbf{MF_i}\right\rangle, \text{for } i=1,2,...,e, \tag{4.8}$$

where, $\langle .,. \rangle$ represents the inner product. Here $\hat{\alpha}_{init_i}$ gives the initial estimate of the abundance of the i^{th} endmember. The equation (4.8) is applied at every pixel vector of the data cube for all available endmembers, which yields e number of initial abundance maps each of size $\mathbf{N_1}\times\mathbf{N_2}$ pixels.

The initial estimate of abundances using equation (4.7) and equation (4.8) may not correspond to the abundances closer to their true values. This is because although the abundances estimated using the equations (4.7) and (4.8) make use of the data covariance in order to enhance the output SNR of endmembers, they do not correspond to optimal unmixing [195]. However they serve as better estimate in finding the required parameters that indicate the global dependencies of abundances. Hence, we use the matched filters to find the initial estimate of abundances as given by equation (4.7). This in turn is employed in estimating the threshold (β). Following steps are used in finding the threshold β:

1. Using the available initial estimate of abundances, calculate the magnitude of gradient at each location. This yields a gradient cube of size $\mathbf{N_1} \times \mathbf{N_2} \times e$.
2. Find the histogram for the magnitude of gradients obtained in step 1.
3. Locate the densely populated gradient bins located near the tail of the histogram. This region represents higher probability of noncoherence among the abundances.
4. Select the center of bins in step 3 as the threshold β.

Since the derived value of β now depends on the data, we call this HMRF as *d*HMRF i.e., data-dependent HMRF.

4.5 MAP-*d*HMRF based Unmixing

In order to solve the problem using the MAP estimation, we need to maximize the probability of $\boldsymbol{\alpha}$ given the data, i.e., maximize $\mathbf{P_r}\left(\boldsymbol{\alpha}|\mathbf{r}\right), \forall \boldsymbol{\alpha}$. Using the Bayes' rule one may write MAP estimate of $\boldsymbol{\alpha}$ as

$$\hat{\boldsymbol{\alpha}} = \arg\max_{\forall \boldsymbol{\alpha}} \mathbf{P_r}\left(\mathbf{r}|\boldsymbol{\alpha}\right) \mathbf{P_r}\left(\boldsymbol{\alpha}\right) \tag{4.9}$$

$$\textbf{s.t.:}\ 0 \leq \hat{\alpha}_i \leq 1,\ \forall i \text{ and } \textstyle\sum_{i=1}^{e} \hat{\alpha}_i = 1.$$

Since maximizing the probabilities in the equation (4.9) is equivalent to maximizing their logarithmic probabilities, the equation (4.9) can now be written as

$$\begin{aligned} \hat{\boldsymbol{\alpha}} &= \arg\max_{\forall \boldsymbol{\alpha}} \left[\mathbf{log} P_r\left(\mathbf{r}|\boldsymbol{\alpha}\right) + \mathbf{log} P_r\left(\boldsymbol{\alpha}\right)\right] \\ &= \arg\min_{\forall \boldsymbol{\alpha}} \left[-\mathbf{log} P_r\left(\mathbf{r}|\boldsymbol{\alpha}\right) - \mathbf{log} P_r\left(\boldsymbol{\alpha}\right)\right]. \end{aligned} \tag{4.10}$$

Here the first and the second terms represent the likelihood probability and the prior probability, respectively. Using the equations (4.1) and (4.2) one can show that the likelihood probability at every location can be obtained as

$$\mathbf{P_r}\left(\mathbf{r}|\boldsymbol{\alpha}\right) = \frac{\mathbf{1}}{\left(\mathbf{2}\boldsymbol{\pi}\boldsymbol{\sigma}^{\mathbf{2}}\right)^{\frac{\mathbf{W}}{\mathbf{2}}}} \mathbf{exp}\left(\frac{-\left\|\mathbf{r} - \mathbf{M}\boldsymbol{\alpha}\right\|^{\mathbf{2}}}{\mathbf{2}\boldsymbol{\sigma}^{\mathbf{2}}}\right). \tag{4.11}$$

Using the equations (4.3), (4.5), (4.10) and (4.11) one can obtain the estimate of abundances ($\hat{\boldsymbol{\alpha}}$) as the minimization of the following energy functions,

$$\hat{\boldsymbol{\alpha}} = \begin{cases} \arg\min\limits_{\forall \boldsymbol{\alpha}} \left[\dfrac{\|\mathbf{r} - \mathbf{M}\boldsymbol{\alpha}\|^2}{2\boldsymbol{\sigma}^2} + \lambda \sum\limits_{i=0}^{e-1} \left| \alpha_i - \alpha_{(i+1 \ mod \ e)} \right|^2 \right], \text{if } \alpha_d \leq \beta, & \text{(4.12a)} \\ \arg\min\limits_{\forall \boldsymbol{\alpha}} \left[\dfrac{\|\mathbf{r} - \mathbf{M}\boldsymbol{\alpha}\|^2}{2\boldsymbol{\sigma}^2} + \lambda \sum\limits_{i=0}^{e-1} \left(2 \left| \alpha_i - \alpha_{(i+1 \ mod \ e)} \right| \beta - \beta^2 \right) \right], \text{if } \alpha_d > \beta. & \text{(4.12b)} \end{cases}$$

The first term in each of these equations represents the data-term and the second term represents the prior-term. Here λ indicates the weighing factor between these two terms. The incorporation of the *d*HMRF as the prior distribution on the abundance maps allows us to simultaneously preserve the smoothness and sudden variations among the abundances. This is because the quadratic penalty $\alpha_d \leq \beta$ in equation (4.12a) preserves the smooth variations while the discontinuities in the abundances are taken care by the linear penalty for $\alpha_d > \beta$ by equation (4.12b). The equations (4.12a) and (4.12b) simultaneously minimized making use of a global optimization technique particle swarm optimization (PSO) [197]. Though the PSO is an evolutionary approach, it has a simple implementation structure. Recently, PSO has been successfully used as an optimization tool in solving various problems related to the hyperspectral data, such as precise recovery of the endmembers [198], and better classification of hyperspectral data [199]. It can also be implemented in parallel form in order to reduce the time complexity.

A key to fast convergence of PSO lies in its initialization with problem-specific group of particles. In this work, we use a group of initial particles derived from Dirichlet density function that ensures nonnegativity and the sum-to-one constraints on the abundance values. Dirichlet function has been used in the spectral unmixing for detecting endmembers and in modeling the abundances [115, 64, 138].

The PSO searches for the best solution through an iterative process by computing the fitness cost. Let α_{bp}^k and α_{bg}^k be the personal and the global best particles, respectively, at the k^{th} iteration with the fitness values $F_{\alpha_{bp}^k}$ and $F_{\alpha_{bg}^k}$, respectively. While optimizing using PSO, the velocity V_{α_b} and the position α_b (abundance value) are updated as,

$$V_\alpha b^{k+1} = w\alpha_b^k + c_1 r_1 \left(F_{\alpha_{bp}^k} - F_{\alpha_b^k} \right) + c_2 r_2 \left(F_{\alpha b g^k} - F_{\alpha_b^k} \right), \tag{4.13}$$

and

$$\alpha_b^{k+1} = \alpha_b^k + V_\alpha b^k, \tag{4.14}$$

where r_1 and r_2 are random numbers with uniform distribution in $[0, 1]$. Here w, c_1 and c_2 are the constants representing the memory of previous velocities, cognitive and social parameters, respectively. The final values of $\boldsymbol{\alpha}$ are obtained iteratively using the equations (4.13) and (4.14), respectively. The convergence is obtained when every particle has the same personal best that equals the global best. This minimization is carried out at each location in order to estimate the complete abundance maps.

4.6 Theoretical Analysis of MAP-*d*HMRF based Unmixing

We now carry out the theoretical analysis of the proposed approach and compare it with the FCLS [122] and MaxEnt [126] approaches. This analysis illustrates the effectiveness of the proposed approach for solving unmixing problem.

The remotely sensed hyperspectral reflectance is inevitably corrupted by the noise originating from various sources which can be conveniently modeled as additive white Gaussian noise (AWGN). Given the corrupted data $\mathbf{r}$ acquired over the W contiguous bands and the endmember matrix $\mathbf{M}$, the linear unmixing estimates the underlying abundance values $\boldsymbol{\alpha}$ of every endmember. Solving the unmixing problem using a mixing model as given in equation (4.1) is challenging due to the following reasons, 1) though the endmembers are linearly independent, they may be correlated yielding ill-conditioned endmember matrix. This causes errors while inverting it to obtain the abundances and makes the abundance estimation sensitive to the noise [5], 2) the measured data-vectors across the spectral bands are convex combinations of endmembers enforcing additional constraints on the abundances, i.e., they should be nonnegative and sum-to-one, at each pixel location, and 3) the presence of noise and outliers as well as the overdetermined system of equations makes it difficult to find the true $\boldsymbol{\alpha}$.

In order to carry out the analysis, let us consider the geometric representation of various vectors which can be shown using the nonzero line segments. The acquired data over different locations of the scene can be considered as vectors in the W-dimensional nonnegative real vector space, i.e., $\mathbb{R}^{+W}$. The endmembers are the set of linearly independent vectors (bases) that span the given data vector space. The abundances represent the weights of these basis vectors and their linear combinations form the data vectors in the $\mathbb{R}^{+W}$. The solution space of abundances and various vectors can be better illustrated by considering 2-D space with $W = 2$. Consequently two linearly independent vectors of the $\mathbb{R}^{+2}$ representing the two endmembers $\mathbf{m_1}$ and $\mathbf{m_2}$ are depicted as $\overrightarrow{\mathbf{om_1}}$ and $\overrightarrow{\mathbf{om_2}}$ in Figure 4.2 (a). Here α_1 and α_2 are the scalars representing their abundances at that location. As shown in the figure, the vector $\mathbf{r_{true}}$ is a linear combination of the endmembers $\mathbf{m_1}$ and $\mathbf{m_2}$ with α_1 and α_2 as their weights. Since $\alpha_1 + \alpha_2 = 1$, the solution space (i.e., a line in the 2-D case) for $\boldsymbol{\alpha}$ strictly lies on the dashed line segment as shown in Figure 4.2 (a). It may be noted that Figure 4.2 (a) represents an ideal scenario in which no noise is considered in the data, and the $\mathbf{M}$ and $\boldsymbol{\alpha}$ correspond to their true values. Figure 4.2 (b) shows the practical scenario in which the data is corrupted by the additive noise $\mathbf{r_{noise}}$ giving the measured reflectance as $\mathbf{r}$ instead of $\mathbf{r_{true}}$.

Using this $\mathbf{r}$ and $\mathbf{M}$, we need to estimate the values of the abundances, i.e., $\hat{\alpha}_1$ and $\hat{\alpha}_2$, such that their linear combination with the $\mathbf{m_1}$ and $\mathbf{m_2}$ yields a projection vector $\mathbf{r_p}$ on the solution line shown as dashed. One can estimate the values of abundances such that the error $\|\mathbf{r_{true}} - \mathbf{r_p}\|^2$ is minimum, with the constraint that $\alpha_1 + \alpha_2 = 1$. A least-squares with a condition that the abundances sum-to-one can be solved as,

$$\arg\min_{\forall \boldsymbol{\alpha}} \|\mathbf{r} - \mathbf{M}\boldsymbol{\alpha}\|^{\mathbf{2}} \text{ such that } \hat{\alpha}_{\mathbf{1}} + \hat{\alpha}_{\mathbf{2}} = \mathbf{1}. \tag{4.15}$$

Note that when the abundances are nonnegative, the equation (4.15) leads to the fully-constrained solution, i.e., FCLS solution. Figure 4.2 (b) shows this projection, reconstructed vector $\mathbf{r_p}$ and the associated error. Since any point on the dashed line segment could be a candidate solution, the problem is ill-posed. Solving such a problem is difficult due to the presence of noise as well as outliers in the data. In practice, the number of endmembers is considerably less than the available bands (W) in the data. Most often the endmembers are strongly correlated yielding an ill-conditioned endmember matrix. Hence, the unmixing becomes a severely ill-posed problem. In such cases, one has to regularize the solution using prior information about the solution.

Let us consider the solutions obtained by using different approaches while solving the unmixing problem. The solutions obtained using the FCLS [122] method and Max-

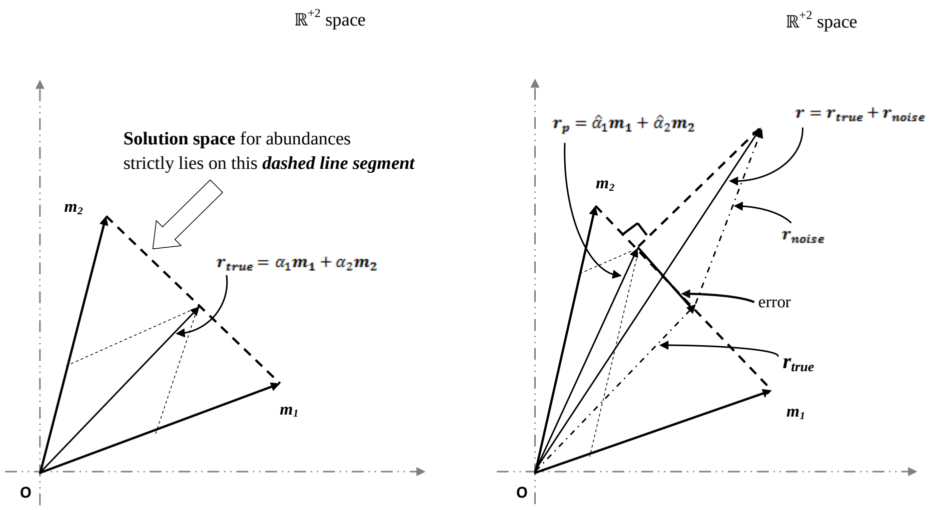

(a) Solution space for abundances. (no noise data)

(b) Solution space for abundances. (noisy data)

Figure 4.2: A 2-D example to illustrate the solution space for abundances.

Ent [126] approach are optimum in the least-squares sense. The FCLS initializes with abundances obtained using nonnegatively constrained least-squares (NCLS) approach [200] and iteratively converges to the fully constrained solution. The MaxEnt initializes the solution with the uniform abundances using their entropy which inherently provides nonnegative constraint. Although this incorporates the physical constraints on the abundances, it also converges in the LS sense [126] and provides a comparable performance with the FCLS. As per the Bayesian principles under the condition of IID Gaussian noise, the LS solution is equivalent to the maximum-likelihood (ML) estimation. This is equivalent to solving the problem using MAP in which uniform distribution is assumed for the prior, i.e., we obtain the estimate as

$$\hat{\boldsymbol{\alpha}} = \arg\max_{\forall \boldsymbol{\alpha}} \mathbf{P_r}\left(\boldsymbol{\alpha}|\mathbf{r}\right) = \arg\max_{\forall \boldsymbol{\alpha}} \mathbf{P_r}\left(\mathbf{r}|\boldsymbol{\alpha}\right) = \arg\min_{\forall \boldsymbol{\alpha}} \|\mathbf{r} - \mathbf{M}\boldsymbol{\alpha}\|^{\mathbf{2}} \tag{4.16}$$

$$\textbf{s.t.:}\ 0 \leq \hat{\alpha}_i \leq 1, \text{ for } i = 1, 2, ..., e. \text{ and } \textstyle\sum_{i=1}^{e} \hat{\alpha}_i = 1.$$

Equation (4.16) indicates that both the FCLS and MaxEnt assume uniform distribution for the prior yielding the LS solution. This also indicates that no assumption is made on the solution space which in turn increases the error while estimating the abundances. Unlike these approaches, the proposed approach uses the MAP framework that incorporates the data-dependent prior while solving for abundances. Our approach uses additional information about the variations in the abundances which is derived from the initial estimate and improves the constrained least-squares solution. As discussed in Section 4.4, the initial estimate obtained using the matched-filters approach is based on the data covariance and hence the derived threshold β provides the required information about the abundances variations. Use of proper value of β in our MAP solution results in abundances that reduce the data reconstruction error.

The performance improvement of the proposed approach can now be analyzed using the geometric illustration. Continuing with the 2-D example, the given reflectance represents a mix of two endmembers with the proportions based on the area covered by these spectral signatures. Figure 4.3 shows geometric representation of various vectors and the solutions using the FCLS, MaxEnt and the proposed methods. As shown in Figure 4.3 (a), we consider two linearly independent endmember vectors $\mathbf{m_1}$ and $\mathbf{m_2}$ depicted as $\overrightarrow{\mathbf{om_1}}$ and $\overrightarrow{\mathbf{om_2}} \in \mathbb{R}^{+2}$. We know that the solution space for the abundances has to lie on the line segment $\overline{\mathbf{m_1 m_2}}$. Given the corrupted $\mathbf{r}$, one needs to find a projection of the $\mathbf{r}$ on the line segment $\overline{\mathbf{m_1 m_2}}$ in order to locate the abundances.

Figure 4.3 (a) shows the solution space for the proposed approach. Here, the optimization is carried out by using the PSO which we initialize the abundances using the particles drawn from Dirichlet distribution including those estimated using the other approaches and these are inherently nonnegative and sum-to-one. The resultant solution using the formulation given in equation (4.9) is guaranteed to lie within the physically acceptable range of abundances, i.e., they lie on the line segment $\overline{\mathbf{m_1 m_2}}$. Figure 4.3 (a) shows different projections of $\mathbf{r}$ on $\overline{\mathbf{m_1 m_2}}$ due to initialization by the candidate abundance particles.

Table 4.1: A Comparative Summary of the FCLS method, the MaxEnt approach and the proposed MAP-*d*HMRF approach.

Algorithm	**Inputs**	**Initial estimate**	**Working principle**	**Ill-posedness***	**Optimization**	**Initialization**	**Solution**	**Output**
FCLS[122]	$\mathbf{r}$ & $\mathbf{M}$	-	FCLS	-	Quadratic prog.	NCLS[200]	ML	constrained $\hat{\boldsymbol{\alpha}}$
MaxEnt[126]	$\mathbf{r}$ & $\mathbf{M}$	-	FCLS + entropy prior	-	Gradient descent	uniform $\hat{\boldsymbol{\alpha}}$	ML	constrained $\hat{\boldsymbol{\alpha}}$
proposed	$\mathbf{r}$ & $\mathbf{M}$	matched-filters	FCLS + *d*HMRF prior	Yes	PSO	candidate $\hat{\boldsymbol{\alpha}}$	MAP	constrained & improved $\hat{\boldsymbol{\alpha}}$

*****takes care of noise and outliers in $\mathbf{r}$, ill-conditioning of $\mathbf{M}$ and sudden variations in abundances.

Figure 4.3 (b) depicts the scenario for one of the iterations for the three approaches. FCLS initializes with the abundances obtained using the NCLS [200] and the MaxEnt with uniform abundances. Both the FCLS and MaxEnt yield the mean squared error as $\left\|\mathbf{r} - \mathbf{M}\boldsymbol{\alpha}_{\boldsymbol{FCLS/MaxEnt}}\right\|^{\mathbf{2}}$. The proposed approach performs the MAP optimization on the initial abundance particles iteratively then finally converges to the solution. Figure

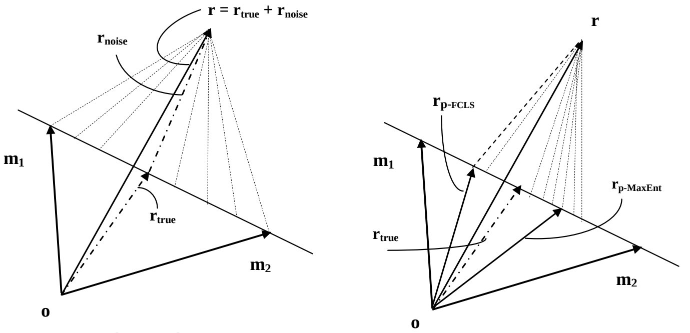

(a) Proposed approach
(········ due to initialization particles)

(b) Proposed, FCLS and MaxEnt approach
(one of the iterations)

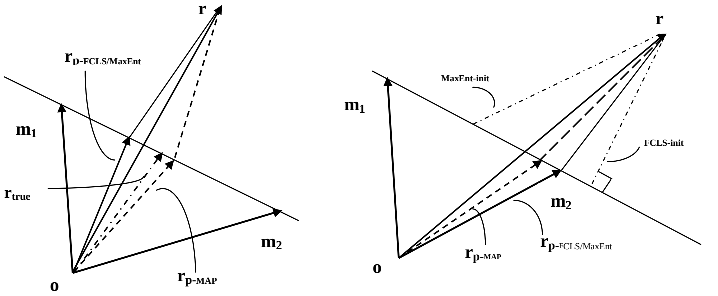

(c) Proposed and FCLS/MaxEnt approach (final solution)
(FCLS/MaxEnt initial projection within the solution space)
$\|r_{true} - r_{p-MAP}\| < \|r_{true} - r_{p-FCLS/MaxEnt}\|$

(d) Proposed and FCLS/MaxEnt approach (final solution)
(FCLS initial projection outside the solution space)
$\|r_{true} - r_{p-MAP}\| < \|r_{true} - r_{p-FCLS/MaxEnt}\|$

Figure 4.3: Geometric illustration of the proposed MAP-*d*HMRF solution compared with the FCLS/MaxEnt solution.

4.3 (b) shows that as the iterations progress, the initialized particles in our approach converge to a set of projection vectors that yield better abundances. Figure 4.3 (c) depicts the final solution for the three methods. As seen from the Figure 4.3 (c) we have $\|\mathbf{r_{true}} - \mathbf{r_{p-MAP}}\|_\mathbf{2} < \|\mathbf{r_{true}} - \mathbf{r_{p-FCLS/MaxEnt}}\|_\mathbf{2}$. This is because the data-dependent HMRF prior forces the solution closer towards the true abundances α_1 and α_2 so the reconstructed reflectance is closer to $\mathbf{r_{true}}$. The β derived from the initial estimate of the abundances forces the minimization in equation (4.12) to the true solution by imposing the additional condition of dependencies of the abundances. This clearly indicates that the solution using the proposed approach represents better unmixing.

In order to show superiority of the proposed method even when a measured reflectance $\mathbf{r}$ has the dominance of one of the endmembers, i.e., when we consider that the significant content of the scene is due to one of the materials, the situation is as shown in Figure 4.3 (d). Note that in this case the abundance for $\mathbf{m_1}$ has a small nonzero value but the $\mathbf{m_2}$ dominates. For such a data, the initial error projection for FCLS is outside the limits of $\overline{\mathbf{m_1 m_2}}$ as shown by FCLS-init in Figure 4.3 (d). Since the FCLS converges in the LS sense, at most it converges to a point where the reflectance vector is $\overrightarrow{\mathbf{om_2}}$ and hence results in $\hat{\alpha}_1 = 0$ and the $\hat{\alpha}_2 = 1$ which are incorrect. This is because $\hat{\alpha}_1$ is small but nonzero. As shown in Figure 4.3 (d), the MaxEnt initializes the abundances with the uniform distribution giving the initial error vector projection MaxEnt-init. Both the MaxEnt and the FCLS converge to the same solution which is shown as $\mathbf{r_{p-FCLS/MaxEnt}}$ in Figure 4.3 (d). On the other hand, as already explained the proposed approach iteratively chooses the abundances and yields a projection that results in nonzero abundance value for $\hat{\alpha}_1$ and a value of $\hat{\alpha}_2$ closer to 1 thus reflecting the dominance by the $\mathbf{m_2}$ as required. This is shown by the projection $\mathbf{r_{p-MAP}}$ in Figure 4.3 (d). Thus in our approach, we obtain better solution when compared to the FCLS as well as MaxEnt methods, even when one of the endmembers is dominant in the data.

Table 4.1 shows the comparative summary of various key features of the FCLS, MaxEnt and the proposed method. It is clear from the Table 4.1 that the proposed approach makes use of additional details about the entity to be estimated in order to improve the solution.

4.7 Experimental Analysis

We now demonstrate the efficacy of our approach to recover abundances from the given data. We first conduct the experiments on the synthesized images using three spectral signatures of the US Geological Survey (USGS) digital spectral library [85]. Next, we show the experiments on the real data collected by the Airborne Visible/InfraRed Imaging Spectrometer (AVIRIS) over the Cuprite mining site area [201]. Finally, we discuss the choice of various parameters used in the optimization and give the sensitivity analysis of the parameter λ and β.

We compare the performance of the proposed method with two of the state-of-art approaches, the FCLS [122] and the MaxEnt [126]. Comparison of the proposed approach is also done with the results obtained using our work [135] in which the β was empirically chosen. Further we compare the results with Tikhonov regularization [131] which is based on the total least squares (TLS) formulation. We also demonstrate the unmixing results by imposing only the nonnegativity constraint in the proposed method and compare the performance with the nonnegative constrained least-squares (NCLS) [202] method. The various parameters used while minimizing the proposed energy function using PSO are tabulated in Table 4.2. These parameters were fixed after verifying them for satisfactory results on synthetic data.

Table 4.2: Parameters used in the proposed MAP-*d*HMRF energy function.

Parameter	Value
w	0.01
c_1	0.01
c_2	0.01
λ	1.00

4.7.1 Experiments with synthetically generated data

For constructing the synthetic data, we use the 224 contiguous band reflectance spectra in the spectral range of 400-2500 nm. The data has three spectrally distinct materials namely, Ammonioalunite NMNH145596, Brucite HS247.3B and Andradite WS487 and are downloaded from the USGS library [85]. The signatures of these materials, i.e., endmember values, are known which form an endmember matrix $\mathbf{M}$ of size 224×3 where the three column vectors correspond to the spectral signatures. Using the known abundance vector $\boldsymbol{\alpha}$ of size 3×1, a pixel vector $\mathbf{r_{true}}$ is constructed as $\mathbf{r_{true}} = \mathbf{M}\boldsymbol{\alpha}$, generating a 224×1 reflectance data vector. Considering an image of size 75×75 pixels for each band, a total of $75 \times 75 = 5625$ reflectance vectors are generated. This yields a 224-band hyperspectral ground truth reflectance cube with each band image having a size of 75×75 pixels. The corresponding ground truth abundance maps each of size 75×75 pixels are shown in Figure 4.4. It can be seen that the scene is divided into nine regions with each region having different linear mixing proportions. This kind of mixing is chosen to test our algorithm on both homogeneous as well as heterogeneous nature of abundance values. The experiments are conducted to estimate the abundance maps for different levels of the additive noise in the reflectance, i.e., the synthesized data.

We first derive Huber threshold β from the available data. The initial estimate of abundance maps are obtained using the matched filters approach as discussed in Section 4 as follows. Matched filter responses are obtained using equation (4.6) where the endmember matrix constructed using the USGS library signatures [85] are utilized. Then using the equation (4.7), the inner product of the filtered output and the mean subtracted data vector results in the initial estimate of the abundances. These estimates are used to

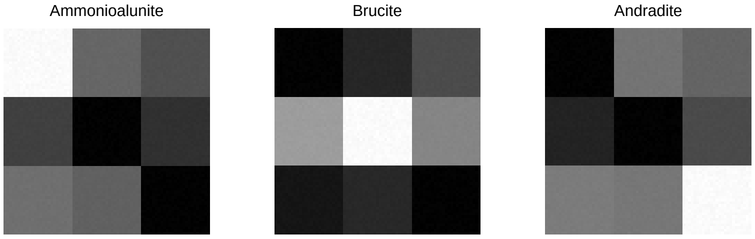

Figure 4.4: Ground truth abundance maps for the three endmembers of synthetic data.

obtain the histogram of the magnitudes of gradients from which the β value is derived. The initial estimates of abundance maps for increasing amounts of noise in the data are shown in Figure 4.5. No noise case, i.e., SNR $= \infty$, is shown in Figure 4.5 (a). In Figure 4.5 (b) and Figure 4.5 (c), we show these maps for 200 dB and 20 dB SNR, respectively. The histograms of magnitude of gradients of the estimated abundances computed for each case are displayed in Figure 4.5 (d-f). Following the steps given in Section 4.4, the values of β selected from the histograms are 0.20, 0.1927, and 0.18, for the three cases of no noise, SNR 200 dB and SNR 20 dB, respectively. These values of β are used in our MAP framework to obtain the final abundance maps. Note that the selected β correspond to the center of the gradients region that indicates the high probability of occurrence of discontinuities in abundances.

The abundance maps estimated by using the FCLS [122] and the MaxEnt [126] approaches for the case of 20 dB SNR are shown in Figure 4.6 (a) and Figure 4.6 (b), respectively. The final result of our approach using the β value selected from the proposed method is shown in Figure 4.6 (c). It can be seen that the spatial variations of the abundances estimated using the proposed approach are consistent with the ground truth maps shown in Figure 4.4 as well as when compared to the estimated maps shown in Figure 4.6 (a) and Figure 4.6 (b). We mention here, although the final results are shown for the case of lowest SNR only, the initial estimates of abundances are displayed for SNR of 200 dB as well as 20 dB. This is done in order to point out the resulting variations in estimated values of β. In order to illustrate how well the solution depends on the proper choice of β as done in the proposed method, we show the plots of pixel locations Vs. estimated abundance values for selected regions considering the low and high variations of abundances. Figure 4.7 (a), Figure 4.7 (b), and Figure 4.7 (c) display

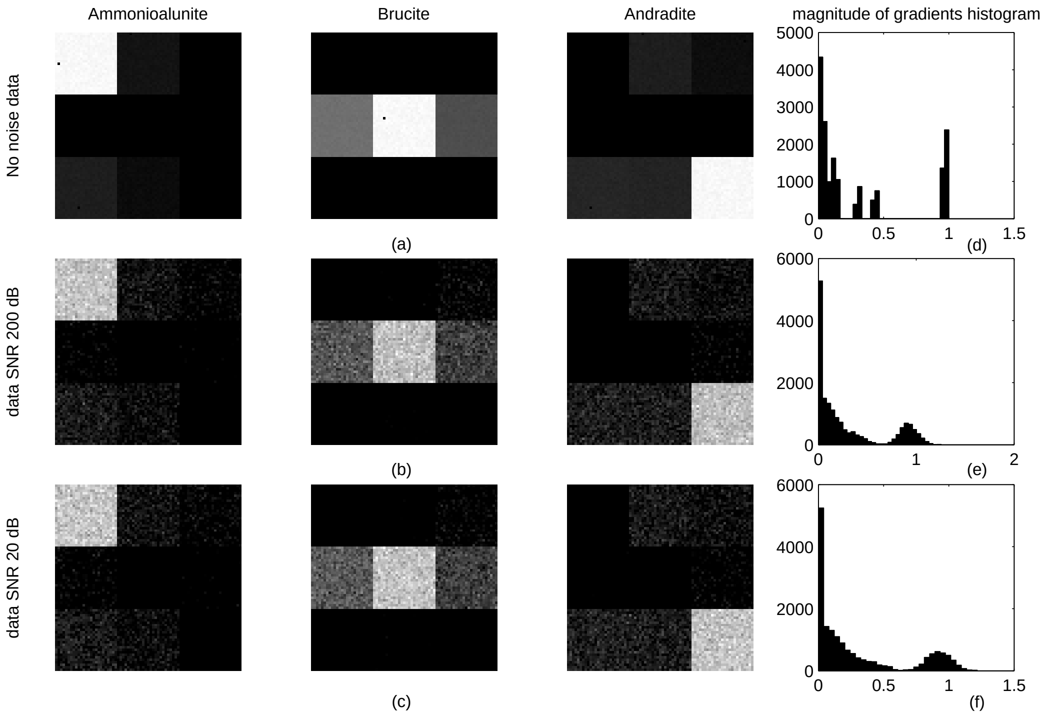

Figure 4.5: Deriving data-dependent β from the synthetic data: Initial estimate of abundances (a) with no noise data, (b) with 200 dB SNR data, and (c) with 20 dB SNR data. The plots in (d), (e), and (f) are corresponding histograms of magnitude of gradients of abundances at each location.

the abundance maps of Ammonioalunite, Brucite and Andradite, respectively, wherein a heterogeneous and a homogeneous region in the data marked as rectangles with red and yellow borders, respectively. These selected regions are also marked in the mean image of the 224 contiguous band synthetic data shown in Figure 4.7 (d). The corresponding pixel locations within the regions Vs. abundance values are shown separately for each material in Figure 4.8. Plots in Figure 4.8 (a) show abundances for the heterogeneous region while Figure 4.8 (b) display abundances for the homogeneous region. In each plot we show abundances estimated using the FCLS method and the proposed approach for SNR = 20 dB. The ground truths are also shown for the comparison. Here, we avoid showing the comparison with the MaxEnt approach since it has comparable performance to the FCLS method. As expected, one can see from the figure that the estimated abundances at different locations using the proposed approach are closer to the ground truth. This indicates that the proper choice of β is important for better estimates of abundances.

We now discuss the quantitative performance of the proposed approach and compare

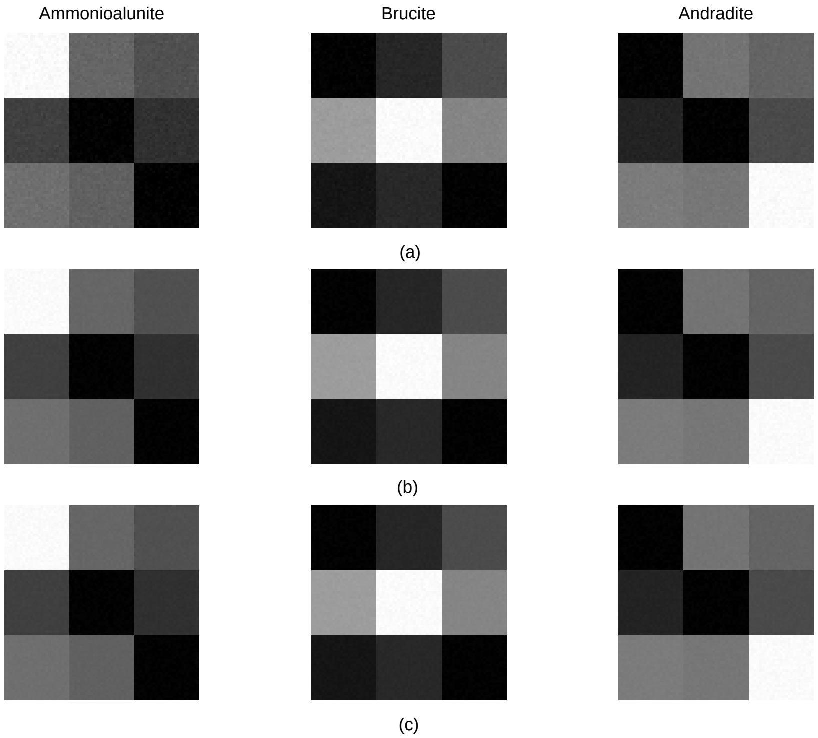

Figure 4.6: Unmixed images for synthetically generated data with 20 dB SNR: Estimated abundance maps by using (a) the FCLS [122] method, (b) the MaxEnt [126] approach, and (c) the proposed MAP-*d*HMRF approach [157].

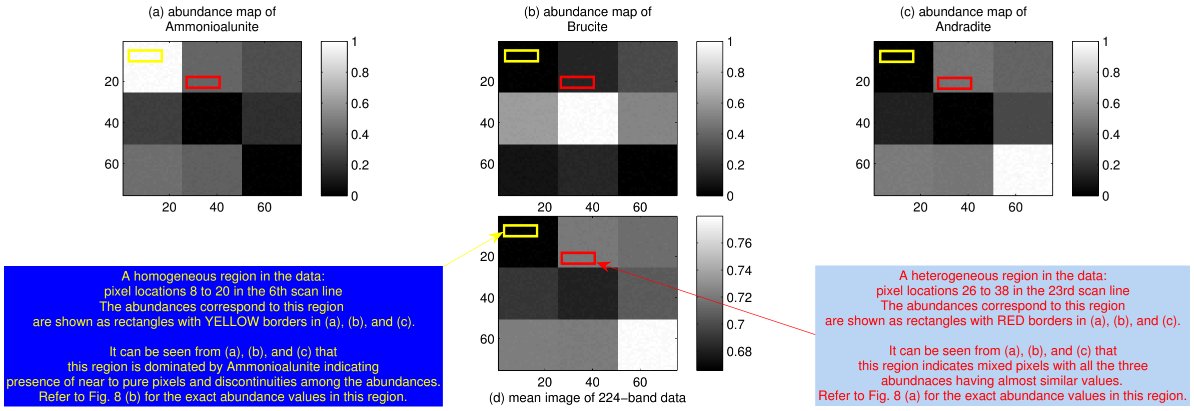

A homogeneous region in the data:
pixel locations 8 to 20 in the 6th scan line
The abundances correspond to this region
are shown as rectangles with YELLOW borders in (a), (b), and (c).

It can be seen from (a), (b), and (c) that
this region is dominated by Ammonioalunite indicating
presence of near to pure pixels and discontinuities among the abundances.
Refer to Fig. 8 (b) for the exact abundance values in this region.

A heterogeneous region in the data:
pixel locations 26 to 38 in the 23rd scan line
The abundances correspond to this region
are shown as rectangles with RED borders in (a), (b), and (c).

It can be seen from (a), (b), and (c) that
this region indicates mixed pixels with all the three
abundnaces having almost similar values.
Refer to Fig. 8 (a) for the exact abundance values in this region.

Figure 4.7: Selected regions shown in the abundance maps and in the mean image of 224 contiguous bands synthetically generated data. Abundance map of (a) Ammonioalunite, (b) Brucite, and (c) Andradite, with heterogeneous and homogeneous region in the data marked as rectangles with red and yellow borders, respectively, and (d) mean image of the 224-band data with the corresponding regions marked with the rectangles using the respective colors. The corresponding abundance values are shown in Figure 4.8.

the same with the other approaches. In order to do this, we used the following measures: root mean squared error (RMSE) [106], spectral angle mapper (SAM) [107] and spectral

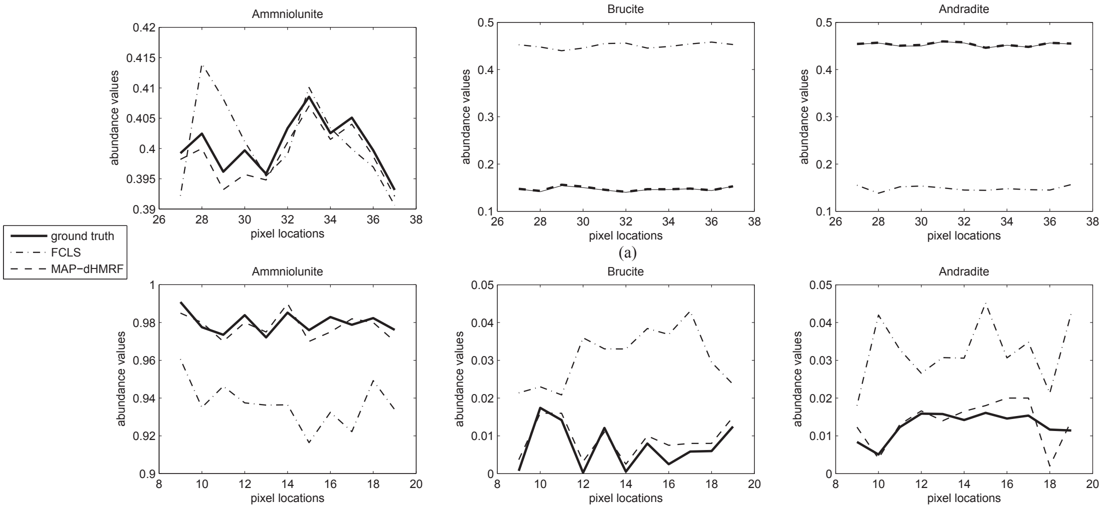

(a)

(b)

Figure 4.8: Pixel locations Vs. estimated abundances on selected regions within synthetic data (20 dB SNR): (a) estimated abundances in the heterogeneous reflectance region (a region where abundance values are almost similar referring to rectangles with red borders in Figure 4.7) using FCLS method [122] and using the proposed approach [157], and (b) estimated abundances in the homogeneous reflectance region (a region where abundance values have discontinuity referring to rectangles with yellow borders in Figure 4.7) using FCLS method [122] and using proposed approach [157]. Note that the scale in the graphs of (a) and (b) are different, indicating higher variance in the abundances displayed in (b).

information divergence (SID) [108]. These measures are considered in order to assess the preservation of the spatial as well as spectral characteristics in the estimated abundances. Lower values of the RMSE ensures the spatial fidelity while lower values of the SAM and SID indicate the spectral fidelity. These measures averaged over the entire set of abundance values i.e., 75 × 75 × 3 are shown in the Table 4.3 for various approaches. These values shown under NSCA (nonnegative and sum-to-one constrained abundances) in the table indicate the performance for increasing levels of noise in the data starting from 1000 dB to 20 dB SNR. From the Table 4.3 we observe that as far as the performance in terms of quantitative measures are concerned, the proposed approach outperforms all the other approaches, with the exception of FCLS performing little bit better in terms of RMSE at high SNR of 1000 dB. The reasons for this are as follows. The noise in the data is almost non existent at such a high SNR making it free from outliers, so the FCLS method being the least-squares approach converges to a solution that yields abundances closer to the true values. However, the proposed approach uses the prior information in terms of dHMRF and hence forces the solution to drift relatively from the true abundances even when the noise level in the data is minimum. One can see that even though FCLS has better spatial fidelity at low noise level, it performs poor in terms of preservation of spectral characterization which is clearly evident from the high values for SAM and SID. One may conclude that at lower noise level, the proposed MAP-*d*HMRF approach exhibits spatial enhancement comparable to the state-of-art method such as FCLS approach but it performs better as far as spectral preservation is concerned. It should be noted that for increasing levels of noise, the proposed approach outperforms all the other approaches.

Table 4.3: Noise Sensitivity Analysis and Comparative Performance. Average Error Scores for the Unmixing with the Synthetic data. The Minimum Values of Each Error are Shown in Bold Typeface

Measure	Abundances	Algorithm	SNR = 1000 dB	SNR = 200 dB	SNR = 50 dB	SNR = 20 dB
RMSE [106]	NSCA	FCLS [122]	**0.0005**	0.0088	0.0102	0.0177
		MaxEnt [126]	0.0896	0.1836	0.2638	0.2740
		TLS-Tikhonov [131]	0.0436	0.1014	0.2533	0.2681
		MAP-HMRF [135]	0.0785	0.1237	0.2733	0.2783
		proposed (MAP-*d*HMRF) [157]	0.0008	**0.0012**	**0.0022**	**0.0025**
	NCA	NCLS [202]	**0.0004**	0.0093	0.0157	0.0245
		proposed (MAP-*d*HMRF) [157]	0.0009	**0.0014**	**0.0047**	**0.0111**
SAM [107]	NSCA	FCLS [122]	1.0034	2.7632	7.3645	11.5184
		MaxEnt [126]	2.3416	7.3678	10.7814	12.3802
		TLS-Tikhonov [131]	1.7832	11.9216	15.4017	16.1822
		MAP-HMRF [135]	2.6575	11.3154	13.3921	15.8344
		proposed (MAP-*d*HMRF) [157]	**0.9653**	**2.3421**	**3.9386**	**4.9627**
	NCA	NCLS [202]	1.0003	2.8925	7.7588	12.0178
		proposed (MAP-*d*HMRF) [157]	**0.9942**	**2.6489**	**4.6349**	**5.7876**
SID [108]	NSCA	FCLS [122]	0.0008	0.0129	0.0212	0.0230
		MaxEnt [126]	0.0196	0.2133	0.2912	0.3123
		TLS-Tikhonov [131]	0.0102	0.1038	0.2246	0.2528
		MAP-HMRF [135]	0.0097	0.0185	0.0989	0.1343
		proposed (MAP-*d*HMRF) [157]	**0.0006**	**0.0087**	**0.0118**	**0.0129**
	NCA	NCLS [202]	0.0007	0.0153	0.0274	0.0311
		proposed (MAP-*d*HMRF) [157]	**0.0004**	**0.0096**	**0.0120**	**0.0164**

NSCA: nonnegative and sum-to-one constrained abundances
NCA: nonnegative constrained abundances

While analyzing the real data, imposing the sum-to-one constraint may lead to misleading results as one may not have the complete endmember information, i.e., number of endmembers and their signatures. However, in the simulated data, we have the complete knowledge of endmembers. This prompted us to assess the performance of the proposed approach by imposing only the nonnegativity constraint on abundances. In the proposed method, only nonnegativity constraint can be imposed by choosing the candidate particles for PSO with a set of random numbers uniformly distributed between $[0, 1]$. Note that the resultant nonnegative abundance values may not necessarily be sum-to-one. Results of

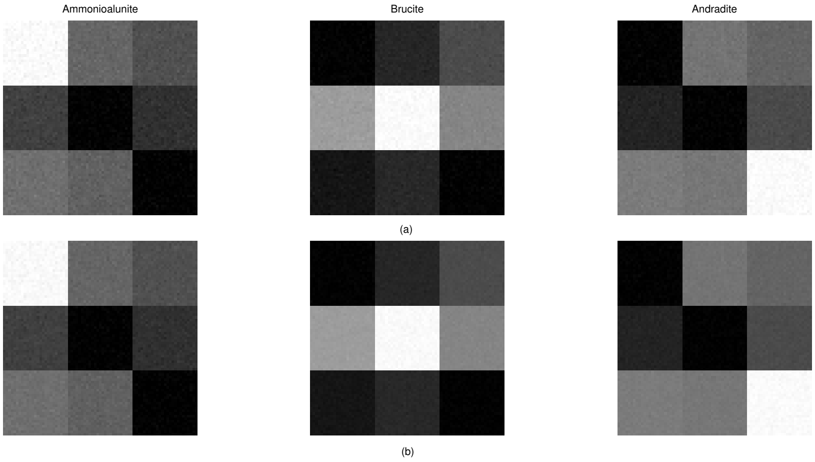

Figure 4.9: Unmixed images of synthetically generated data by considering *nonnegativity constraint* only.: The results are shown for data at 20 dB SNR. Estimated abundance maps by using (a) the NCLS [202] method, and (b) the proposed MAP-*d*HMRF approach [157].

this experiment are compared with the nonnegative constraint least-squares (NCLS) [202] method. Unlike the proposed method which uses prior information of the abundances, the NCLS imposes only the nonnegativity constraint to obtain the solution. Hence, we expect the proposed method to perform better. The estimated abundance maps by the NCLS method and the proposed MAP-*d*HMRF with only nonnegativity constraint are shown in Figure 4.9 at SNR = 20 dB. Figure 4.9 (a) and Figure 4.9 (b) show the estimated abundance maps using the NCLS and the proposed methods, respectively. One may observe from the Figure 4.9 that spatial patterns of the abundances are consistent in both the methods, and the maps are also visually similar to those shown in Figure 4.6. The quantitative measures with the nonnegativity constraint are shown in Table 4.3 under the NCA (nonnegative constrained abundances). From the Table 4.3, we see that only at lowest noise level (SNR = 1000 dB), NCLS performs relatively better in terms of RMSE, however, for all other increasing levels of noise, the performance of the proposed approach is better than the NCLS [202] method.

Finally, we look at the complexity of the various approaches in terms of average processing time and it is summarized in Table 4.4. As far as the comparison with our previous works [131] and [135] is concerned, the proposed MAP-*d*HMRF approach is faster. Also it has lesser execution time than the MaxEnt approach. However, the processing time of the proposed approach is moderately higher when compared to the

FCLS method. This is because of the evolutionary nature of PSO, which increases the time complexity in our method. Similarly, considering the nonnegativity constraint, the average processing time of the proposed approach is relatively higher, however, it is found in the same order as that of the NCLS method. We would like to mention here that one may use parallel implementation for decreasing the execution time using the spatial data-partitioning strategy suggested in [165] and as demonstrated in [203].

Table 4.4: Processing Time to Unmix A Pixel Location using the Synthetic Data Average over different SNR values.

Algorithm	Unmixing time (in seconds)
FCLS [122]	0.0034
MaxEnt [126]	0.2543
TLS-Tikhonov [131]	0.1278
MAP-HMRF [135]	0.6835
proposed (MAP-dHMRF) [157]	0.0331

4.7.2 Experiments on real AVIRIS Cuprite data

In this subsection, we assess the effectiveness of the proposed approach on the benchmark real data. For this purpose, we consider data acquired by the AVIRIS over the Cuprite mining site [201]. The Cuprite site is rich in minerals and is located around 200 Km northwest of Las Vegas (USA). It has been extensively used in experimentation by the remote sensing research community for many years. The data is collected in 224 contiguous wavelength bands ranging from 400-2500 nm with the spectral resolution of 10 nm. For experimenting, we use only a part of the scene [204] which is located towards the east-south center of the scene. The size of an image in each band is 250 × 191 pixels with each pixel covering an area of $20m \times 20m$. Experiments are conducted on 188 bands after removing the bands 1-2, 104-113, 148-167 and 221-224, and they correspond to water absorption having low SNR [204]. In Figure 4.10, we show one of the bands (#50^{th} spectral band) of the data since sufficient number of the minerals are visible in this band.

Based on the mineral classification maps and the information available in [205, 206], and the published results in [102, 126], fourteen endmembers are considered within the scene of selected region. The available endmembers in this region include the following minerals, namely, Chalcedony, Alunite, Kaolinite #1, Nontronite, Kaolinite #3, Desert vanish, Dumortierite, Muscovite, Sphene, Andradite, Pyrope #1, Pyrope #2, Buddingtonite, and Montmorillonite. The virtual dimensionality (VD) [79] algorithm was also run as the verification test which also resulted in fourteen endmembers in the data.

Knowing the number of endmembers, we construct the endmember matrix using the USGS library signatures [85]. An initial estimate of the abundances was then obtained by using the matched-filters based approach which was used in deriving threshold β as was done in the case of synthetic data. In order to show the visual perception of variations of abundances, a map consist of magnitude of gradients of the initial abundance maps averaged at each pixel is displayed in Figure 4.11 (a). In Figure 4.11 (b) we show the histogram of these magnitudes from which a value of $\beta = 0.11$ was selected.

In general a real data may have many unidentified minerals and unknown background signatures. Hence in the absence of complete knowledge about the number of endmembers and their signatures, the unmixing results obtained using physical constraint such as sum-to-one may lead to inaccurate estimates of abundances. It is also safer to drop the sum-to-one constraint on the abundances while unmixing due to the uncertainty in the spectral signatures called the endmember variability which may occur in a real scene [128, 207]. Thus, our proposed model becomes more generalized to represent real scenario. Hence while using the real data we avoid the comparison of our results with the FCLS as well as the MaxEnt approaches since they impose the strict constraint on the abundances. We do show the comparison with the NCLS method. We also show the comparison when the NCLS output is used as the initial estimate in the proposed MAP approach. To do this, we consider the abundances estimated using the NCLS approach as an initial estimate and obtain the β as was done for the matched-filters output as the initial estimate. Figure 4.12 (a) shows the image for the average magnitude of gradients of the abundances obtained using NCLS approach. In Figure 4.12 (b) we show the histogram of magnitude of gradients from which $\beta = 0.15$ was derived. The final estimated abundance maps using the proposed approach are shown in Figure 4.13. We avoid displaying estimated abundance maps using NCLS based approach and using the NCLS as an initial estimate in the MAP approach. We would like to mention here that the estimated abundance maps using the proposed method are visually closer to those of in [205, 206, 102, 126] as well as the abundance maps estimated using the NCLS approach and using the NCLS as an initial estimate in the MAP approach.

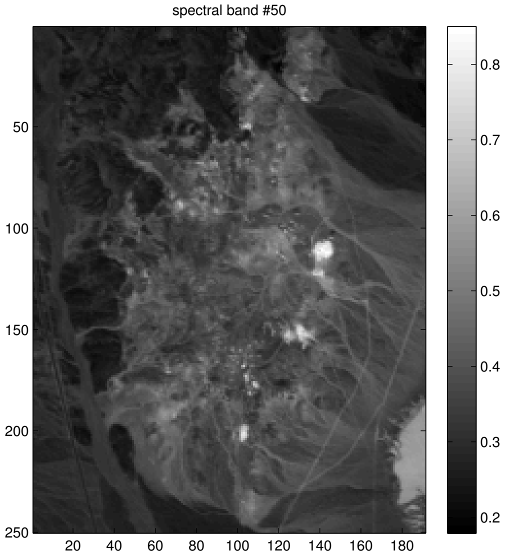

Figure 4.10: The spectral band #50 of the AVIRIS Cuprite data in the selected region.

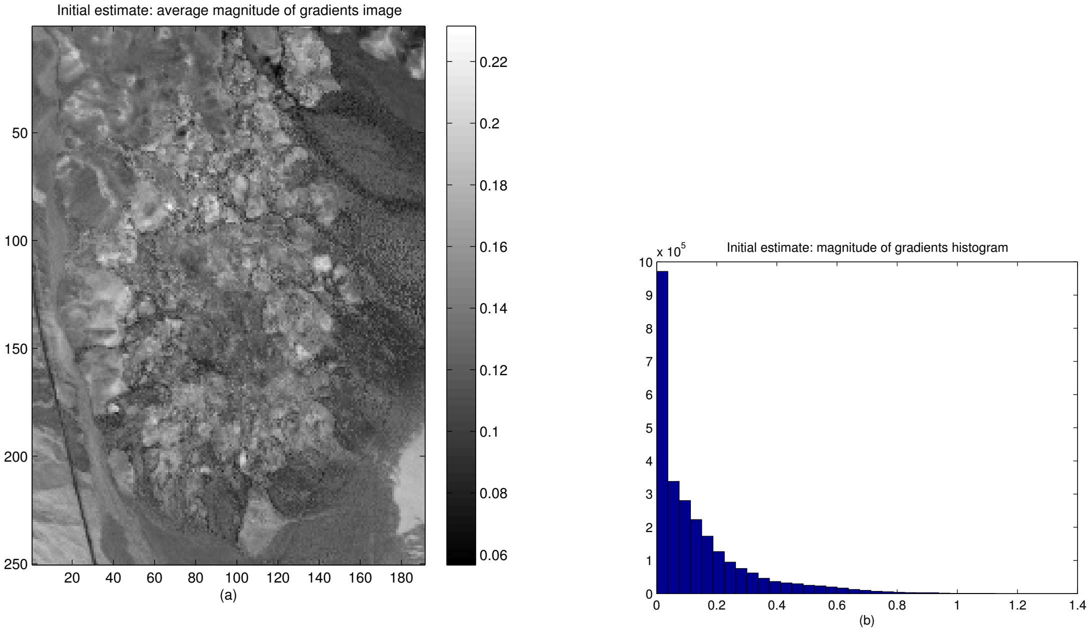

Figure 4.11: Deriving data-dependent β from AVIRIS Cuprite scene using the proposed matched-filters as the initial estimate of abundances (a) average magnitude of gradients of the abundances at each location over the entire scene, and (b) histogram of magnitude of gradients of the estimated abundances. The value of $\beta = 0.11$ is selected from the histogram.

For a quantitative analysis, we first resort to reconstructing the reflectance data using the USGS endmembers while using the estimated abundances from different approaches, and measure the data reconstruction error (DRE) in terms of the RMSE at each pixel location, which is displayed as an image, i.e., a DRE map. In Figure 4.14 (a) we display

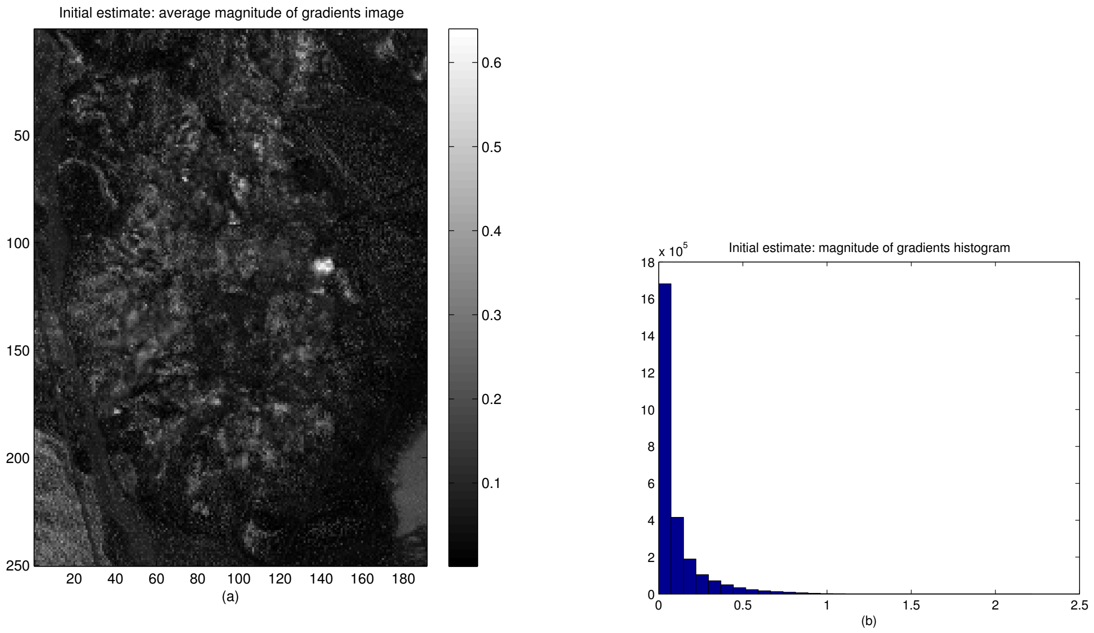

Figure 4.12: Deriving data-dependent β from AVIRIS Cuprite scene using the NCLS as the initial estimate of abundances (a) average magnitude of gradients of the abundances at each location over the scene, and (b) histogram of magnitude of gradients of the estimated abundances. The value of $\beta = 0.15$ is selected from the histogram.

the DRE map for the NCLS [202] based approach. Figure 4.14 (b) shows the DRE map of MAP approach using the abundances estimated using the NCLS method as the initial estimate, and in Figure 4.14 (c) we display the result of the proposed MAP-dHMRF approach [157]. It can be seen from the DRE maps that the proposed approach results in reduced mean as well as standard deviation when compared to both the NCLS as well as the MAP based on NCLS as the initial estimate, indicating lower values for reconstruction error for the proposed method. It is clear that the reduced reconstruction error is an indication of reduced unmixing error, since in these experiments we use the same endmember information for all the approaches in the comparison. One may argue that to take into account the possibility of unidentified signal sources present in the real data, it may be preferable to use the NCLS approach or use the NCLS as an initial estimate in the MAP approach when compared to the matched-filters based estimate. But as shown by the proposed approach, the value of β plays an important role in improving the accuracy of estimated abundances. The reduced error is due to the selection of proper value for β and the regularization as done in the proposed method.

In order to further quantify the results, we use the quality with no reference (QNR)

[208] index from the pansharpening research [209]. It is a quality measure which does not require the availability of the ground truth abundances. Hence, it can be suitable for testing the effectiveness of the algorithms while using the real data. QNR basically generalizes the notion of universal quality index for the multi-band images [210]. We compute the QNR for the reconstructed data and assess both the spatial as well as spectral quality of the reconstructed reflectance. These measures correspond to spectral and spatial distortion indices, i.e., d_{bands} and d_{image}, respectively. QNR [208] is given by

$$\mathrm{QNR} = (1 - d_{bands}) \cdot (1 - d_{image})\,. \tag{4.17}$$

Lower values for d_{bands} and d_{image} measures and in turn a higher value for the QNR closer to unity indicates the better data reflectance. In our case, since the endmembers are same in all the approaches, the reconstructed reflectance should differ with the different abundance estimation techniques. The d_{bands} index amounts for the inter-band distortions across the spectral range of data while the d_{image} considers the average distortions over the spatial locations. We first calculate d_{bands} and d_{image} as in [208] and then insert these values in equation (4.17) to compute the QNR index. Table 4.5 shows the d_{bands}, d_{image}, and QNR indices computed for the different approaches along with their ideal values. It can be seen from the table that the proposed approach has the minimum spectral and spatial indices, resulting in better QNR which indicates improved unmixing.

Finally, we carry out sensitivity analysis by reconstructing the data using the estimated abundances by varying the number of endmembers and measuring the total data reconstruction error (DRE) in each case. The total DRE is computed by summing up the DRE values at every pixel location in the DRE map. Figure 4.15 shows the plot of total DRE versus number of endmembers. It can be seen from the graph that the error decreases more rapidly up to six endmembers while it is almost constant as it approaches the fourteenth endmember. After this point, the error remains almost same. We conclude that though the site has plenty of minerals and may have unidentified signal sources, these have little effect on the unmixing performance.

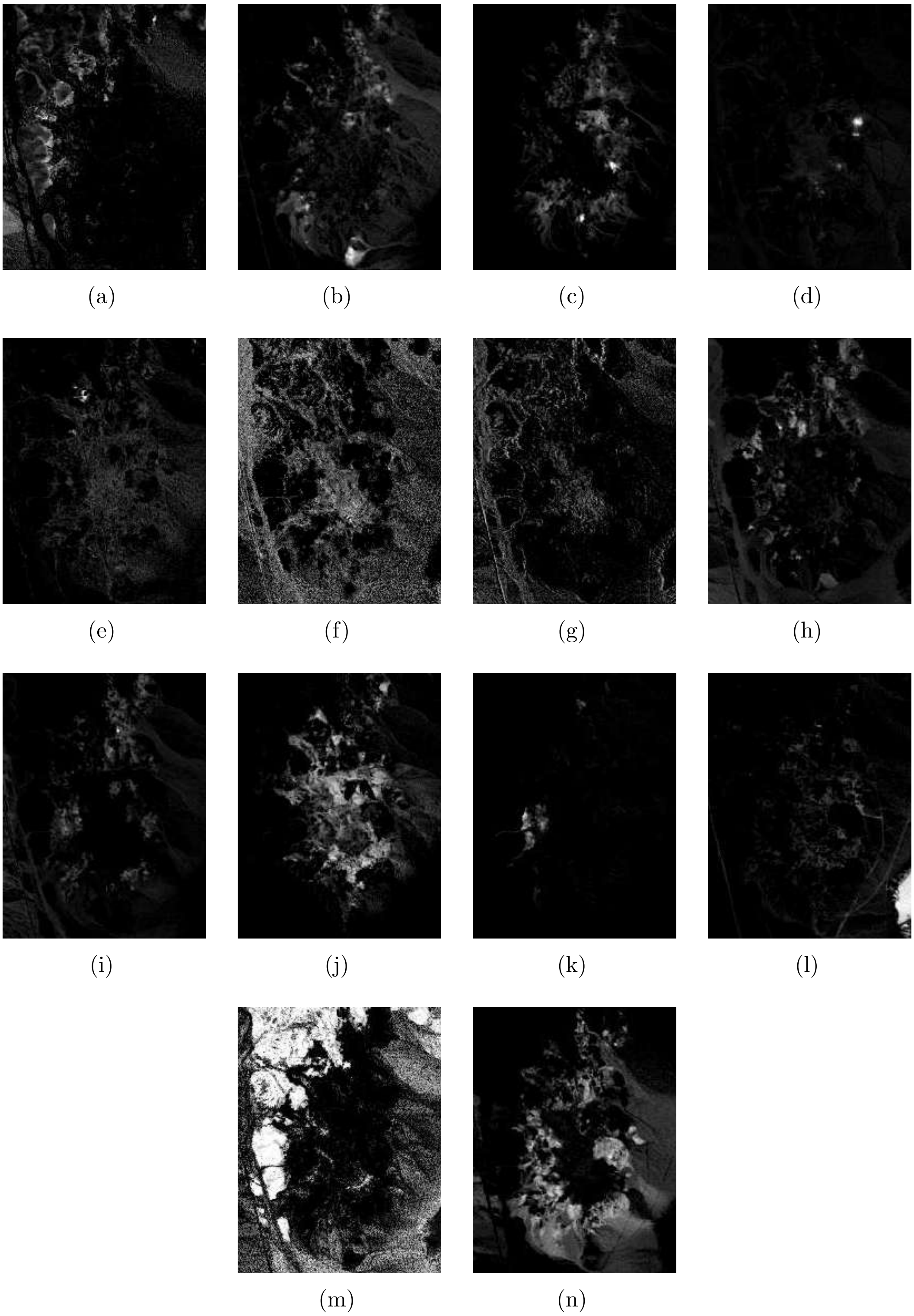

(a) (b) (c) (d)

(e) (f) (g) (h)

(i) (j) (k) (l)

(m) (n)

Figure 4.13: Abundance maps estimated using the proposed MAP-dHMRF approach [157] for the Cuprite scene: (a) Pyrope #1, (b) Kaolinite #3, (c) Pyrope #2, (d) Muscovite, (e) Nontronite, (f) Desert vanish, (g) Andradite, (h) Dumortierite, (i) Kaolinite #1, (j) Chalcedony, (k) Buddingtonite, (l) Montmorillonite, (m) Sphene, and (n) Alunite.

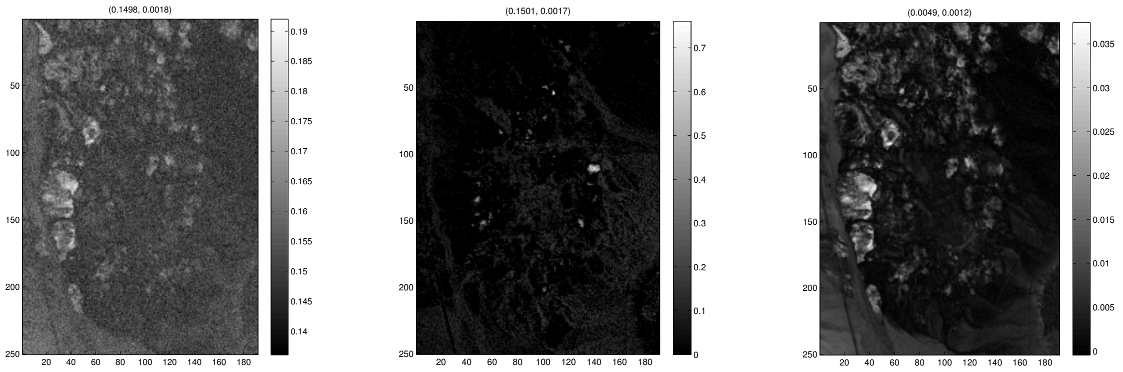

(a) (b) (c)

Figure 4.14: Data reconstruction error (DRE) maps for AVIRIS Cuprite scene. (a) using NCLS [202] based approach, (b) MAP with the NCLS as an initial estimate, and (c) proposed MAP-*d*HMRF approach [157] with nonnegativity constraint. The average errors and their standard deviations are mentioned in parenthesis on the top of each figure. Since the endmember information remains same in all the three cases, the variance of the error is an indication of the difference in estimated abundances by the different approaches. It can be seen that the proposed approach is better in terms of RMSE as well as preservation of abundances variance.

Table 4.5: Spectral distortion index (d_{bands}), Spatial distortion index (d_{image}) and Quality-with-no-reference (QNR) of the reconstructed data using different approaches.

Algorithm	d_{bands}	d_{image}	QNR
Ideal value	0.0000	0.0000	1.0000
NCLS [202]	0.2480	0.3534	0.4888
MAP with NCLS initialization	0.2261	0.3008	0.5417
proposed (MAP-*d*HMRF) [157]	**0.0011**	**0.1921**	**0.8091**

4.7.3 Choice of PSO parameters and sensitivity analysis of λ and β

In this subsection, we discuss the choice of various PSO parameters followed by sensitivity analysis of λ and β on the final solution. In order to fix the various parameters, the experiments are conducted on the synthetic data. This gives us the flexibility in choosing the abundances over the scene and hence allows us to choose the optimum parameters based on the minimum data reconstruction error for different levels of noise in the data. We select the synthetic data as reference to carry out the sensitivity analysis for λ and β. The same parameters are used while conducting the experiments on the real data.

Being an evolutionary algorithm, the parameter settings of PSO are to be done based

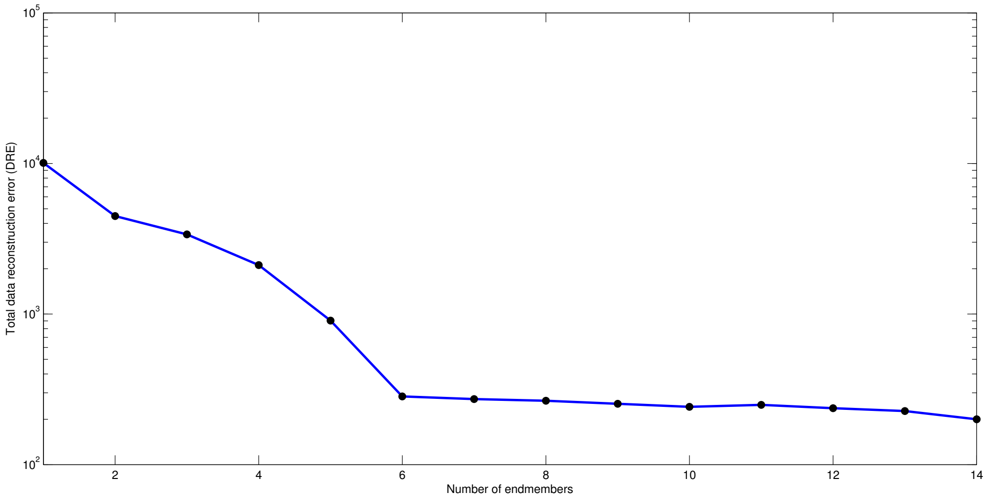

Figure 4.15: Total data reconstruction error for increasing number of endmembers in the AVIRIS Cuprite scene.

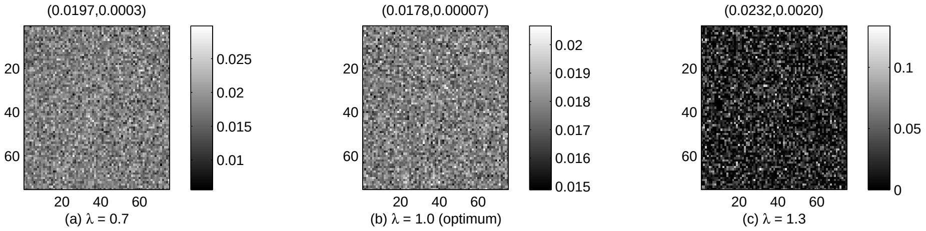

(a) λ = 0.7 (b) λ = 1.0 (optimum) (c) λ = 1.3

Figure 4.16: RMSE maps for the MAP approach using different values of λ at 20 dB SNR in the synthetic data. RMSE map for (a) $\lambda = 0.7$, (b) $\lambda = 1.0$, and (c) for $\lambda = 1.3$. The average errors and their standard deviations are mentioned in the parenthesis on the top of each figure. We see that the RMSE and standard deviation are minimum for $\lambda = 1$.

on the problem at hand. PSO works by moving the swarm of particles, i.e., possible solutions, in the search space with improvements in search influenced by the other particles. Hence the optimization by PSO is dependent on the swarm size and initialization of particles. Though the use of larger swarm size speed-up the convergence, it happens at the cost of increased computations [211, 212, 213]. As a compromise, we choose nine particles and they include the abundances obtained using the FCLS, matched-filters and abundances drawn from Dirichlet distribution. By doing so we restrict the solution space that achieves faster convergence. The PSO expression given in equation (4.13) has three parameters, c_1, c_2, and w, which have to be chosen carefully for better convergence. Researchers have studied the behavior of these parameters on the solution by using a set of standard functions for minimization and have recommended using low values for c_1 and c_2 [211, 212, 213]. We tested the performance of PSO algorithm on the synthetic data by

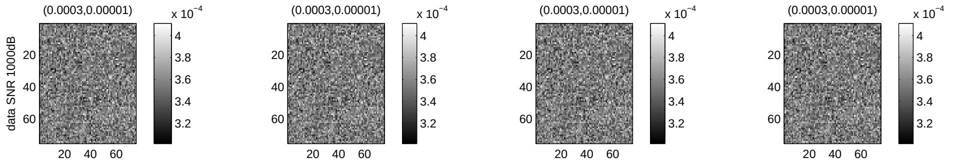

(a) β = 0.20 by FCLS (d) β = 0.20 by MaxEnt (g) β = 0.20 in MAP−HMRF (j) β = 0.20 by matched−filters

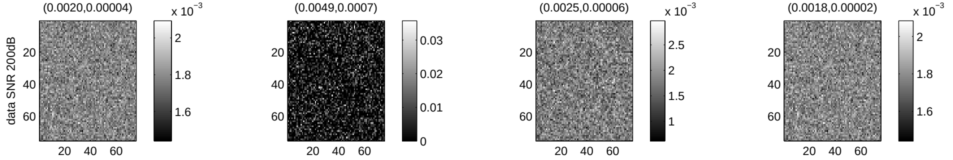

(b) β = 0.1970 by FCLS (e) β = 0.21 by MaxEnt (h) β = 0.20 in MAP−HMRF (k) β = 0.1927 by matched−filters

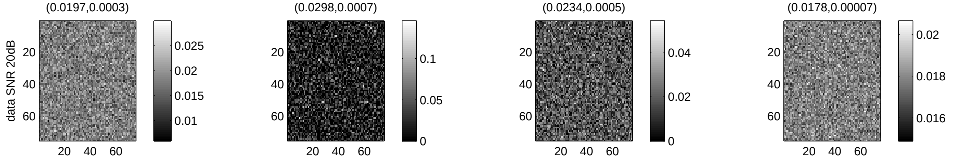

(c) β = 0.19 by FCLS (f) β = 0.22 by MaxEnt (i) β = 0.20 in MAP−HMRF (l) β = 0.18 by matched−filters

Figure 4.17: RMSE maps: Sensitivity analysis for MAP solution using β derived from various initial estimates with increasing noise levels (SNR = 1000 dB, 200 dB, and 20 dB) in the synthetic data. RMSE maps (a-c) for β obtained using the FCLS as initial estimate, (d-f) for β derived using MaxEnt, (g-i) for empirical value of β as used in MAP-HMRF, and (j-l) for β as obtained using the matched filters as the initial estimate (i.e., proposed MAP-*d*HMRF). The average errors and their standard deviations are mentioned in parenthesis on the top of each figure. We see that the better estimate of β obtained by using the matched-filters ensures the minimum average errors and drastic reduction in standard deviations which in turn results in preserving the variance in abundances.

choosing various low values of c_1, c_2, and w, and finally set $c_1 = c_2 = 0.01$, and $w = 0.01$ that resulted in quick convergence.

We now demonstrate the sensitivity of λ as well as β on the solution obtained by varying each of them independently [214]. This provides an opportunity to test the effect of individual parameter on the solution. By selecting the derived value of β and conducting experiments using different λ values, we found that the performance of our approach was optimum when the data and the prior terms have equal weightage, i.e., $\lambda = 1$. The RMSE maps for three different values of λ at the highest noise level of SNR = 20dB is shown in Figure 4.16. One can observe from the RMSE maps that the use of $\lambda = 1$ reduces the average error and has lower standard deviation. We reiterate here that one may use the generalized cross validation (GCV) technique and estimate the regularization parameter λ. However GCV is computationally expensive and we refrain from doing the same in our approach.

A proper value of β is very important as far as the performance of the proposed approach is concerned. β is a global threshold that characterizes the variations of the abundances across the acquired scene. In order to obtain the correct value for the β, one must have the true abundances which are not available, as they are to be estimated. Due to the nonavailability of the strong mathematical models, one has to look for solving such practical problems by using the available data itself. To this end, one can use initial estimate of abundances that preserves the statistical characteristics of abundances. As discussed in Section 4.4, the matched-filters based approach enhances the signal-to-noise ratio (SNR) of the output by considering the properties of data covariance that characterizes the needed global behavior of abundances. Hence we choose the matched-filters based approach in order to derive the initial estimate in the proposed approach.

Now, we verify the suitability of using Huber threshold β estimated from matched-filters in the proposed approach by conducting the experiments on the synthetic data. The experiments are also conducted by using the β derived from the FCLS and MaxEnt approaches, including the empirically selected β as in MAP-HMRF [135]. Since the NCLS based approach was performing poor, we avoid considering the NCLS as an initial estimate. Figure 4.17 shows the sensitivity of the proposed approach in terms of RMSE. Though the values of β obtained using different approaches are same at lowest noise level (i.e., almost no noise in the data), there exist difference with the increasing noise levels. The empirically set β as in the MAP-HMRF case does not guarantee minimum reconstruction error as seen from Figure 4.17 (g-i). One can see that the MAP solution with the β derived using the FCLS as well as MaxEnt approaches do not yield better solution as indicated by the higher RMSE in the Figure 4.17 (b), Figure 4.17 (c), Figure 4.17 (e), and Figure 4.17 (f). This is because the increase in noise affects the LS solution and hence the derived β is inaccurate. By comparing the RMSE maps displayed in Figure 4.17, one can observe significant reduction in the average errors as well as the standard deviations for the β obtained using the matched-filters as done in our proposed MAP-*d*HMRF approach [157] (see Figure 4.17 (k) and Figure 4.17 (l)).

4.8 Conclusions

We have presented a novel approach for unmixing which overcomes the ill-posedness due to the noise and outliers in the data, ill-conditioning of endmember matrix as well as preserves both smooth and the sudden variations in abundances. It has an MAP solution with the data-dependent Huber-MRF prior across the contiguous spectral measurements of the scene. Huber threshold β is derived from the initial estimate of abundances which is found using the matched filters based approach for the endmembers. The detail theoretical analysis shows that the proposed two-step Bayesian approach obtains abundances that minimize the reconstruction error and the experimental demonstration validates the effectiveness of the proposed solution. Deriving the β from the given data obviates the training data resources and the subsequent learning process.

In the previous two chapters, we discussed about the problems related to the abundance estimation and have provided two different solutions under the different conditions. However, we considered that the endmembers were known. In the next chapter, we solve the problem of endmember extraction which in turn can be used in solving the complete spectral unmixing problem.

Chapter 5

Band-wise Endmember Extraction using Multi-temporal data (BEEM)

In this chapter, we develop a new algorithm for the endmember extraction. Given the number of endmembers in a scene, most of the algorithms in the literature for the endmember extraction are using only the spectral space of the data. Few of them use the spatial information in addition to the spectral details to improve the solution. The proposed algorithm in this chapter is mainly based on following two observations: 1) the endmembers together with their abundances form the reflectance in the hyperspectral data, and 2) use of information in terms of temporal characteristics of a scene in addition to the spatial/spectral information results in restricting the solution space. Given these multi-temporal data cubes of the same scene acquired at different times and using the abundances of the cubes, we estimate the endmembers of the scene. We assume that the data cubes representing the scene are co-registered and the variations in the (reflectance) data are due to the variations in the abundances over a period of time [8, 9, 10, 11]. We formulate the problem within the nonnegative constrained least-squares framework that leads to solving an overdetermined system of linear equations. The additional information used in terms of the multi-temporal data and the knowledge of the abundances lead to a better solution for endmembers. We demonstrate a case study of the proposed algorithm on a multi-temporal data generated using real hyperspectral signatures from the USGS spectral library, and the results are compared with the state-of-art approaches using various quantitative measures. The proposed approach performs better when compared to the other approaches.

Most of the research on the abundance estimation relies on the extracted endmembers. In the proposed algorithm, we assume the availability of abundances in order to estimate the endmembers of the scene. We make use of this in our next chapter to solve the complete spectral unmixing.

5.1 Introduction

The algorithms for endmember extraction are either based on the assumption of presence of the pure pixels in the data [5, 86, 87, 88, 89] or they do not assume any thing about the purity of the pixels [109]. Mostly the algorithms work on the spectral space of the data in order to extract the endmembers. Such algorithms include pixel purity index (PPI) [92] and its variants which can be found in [93, 94], the minimum-volume transform based approaches [95, 98], N-FINDR algorithm [98] including development of its variants [215], and the vertex component analysis (VCA) [102] that has drastically reduced the computational complexities of the volume based approaches. The spatial information in the data is also integrated along with the spectral resolution of the data in order to improve the endmembers. This includes automatic morphological endmember extraction (AMEE) [103], spatial spectral endmember extraction (SSEE) [104], and spatial preprocessing (SPP) [105]. Note that these methods invariably assume the presence of pure pixels within the acquired data.

The algorithms which do not assume the presence of pure pixels are mainly based on the concepts of nonnegative matrix factorization (NMF) formulation which was introduced in [110]. A method known as minimum volume constrained nonnegative matrix factorization (MVC-NMF) is proposed in [111] for highly mixed data without making any assumption on the purity of pixels. It introduces the minimum volume constraint in the regularization framework for restricting the solution space. Recently, sparsity based prior is used to detect the endmembers while performing the band selection in the hyperspectral data [216].

The hyperspectral data is composed of its endmembers and their distribution, i.e., abundances, in a scene. Thus it is clear that, given the endmembers, the abundances can be estimated which is done in the previous two chapters. Similarly, given the abundances, the endmembers can also be estimated, since together they form the reflectance values in the scene. Researchers have attempted to use the estimated abundances for extracting the endmembers as demonstrated in [158] which is called as abundance guided endmember selection (AGES).

Looking at the literature, we found that temporal characteristic of the data has not been explored in order to extract the endmembers. Hence, in this chapter, we use the multi-temporal data of the same scene, and formulate the problem in a supervised way wherein given the abundance information, we seek an improved endmember extraction. The idea here is to make use of the variations occurred in the abundances over a period of time. We consider a case wherein the endmembers remain constant, e.g., typically within a season of a year, while the changes in the reflectance (data) are due to the variations in their abundances over the period of time [8, 9, 10, 11].

5.2 Structure of Endmember Matrix

The central idea in hyperspectral remote sensing is to capture the laboratory like spectra of various materials found on the earth. These spectra though not continuous have very fine spectral resolution in terms of narrow and contiguous measurements which qualify them as the signatures of those materials. Due to the hardware limitation and the data acquisition at the high altitude, the hyperspectral signatures are also contiguous in bands. This process is similar to recording reflectance of a material at different wavelength using a spectrometer in the laboratory. Thus remote sensing of a scene captures the spectral signatures of the constituent materials which are called as the endmembers in the spectral unmixing. It is clear that the hyperspectral data has the endmembers at some locations and rest of the locations are mixed with the linear combinations of these endmembers, i.e., linear mixing model (LMM). Hence, the data forms a real nonnegative vector space and the endmembers span the data space.

The endmembers in the LMM form a matrix called endmember matrix that has different materials spectral signatures as its column vectors and the number of columns is given by the number of endmembers in the data. It is found that in general the number of endmembers in a scene is far less than the number of bands. Hence, the endmember matrix is not a square matrix. Since, the endmembers span the entire data space, the column vectors representing the endmember signatures need to be linearly independent.

It should be noted that each value in each spectral signature in an endmember matrix has to be nonnegative due to the passive remote sensing.

Now, let us take a closer look at the structure of an endmember matrix. Considering an endmember matrix **M** of size equals to number of bands times the number of endmembers, it can be seen that each row of the matrix represents reflected values of the different endmembers in a band.

$$\mathbf{M} = \begin{array}{c} \\ \text{band 1} \\ \text{band 2} \\ \text{band 3} \\ \vdots \\ \text{band W} \end{array} \begin{array}{c} \begin{array}{cccc} \text{endmember 1} & \text{endmember 2} & \cdots & \text{endmember e} \end{array} \\ \begin{pmatrix} m_{1,1} & m_{1,2} & \cdots & m_{1,e} \\ m_{2,1} & m_{2,2} & \cdots & m_{2,e} \\ m_{3,1} & m_{3,2} & \cdots & m_{3,e} \\ \vdots & \vdots & \ddots & \vdots \\ m_{W,1} & m_{W,2} & \cdots & m_{W,e} \end{pmatrix} \end{array}, \tag{5.1}$$

where, $m_{i,j} \geq 0$ for $i = 1, .., W$ and $j = 1, ..., e$.

The structure of the endmember matrix allows us to estimate the endmembers in either column-wise or row-wise format. In this chapter we propose an approach to extract the endmember values in each band which is the row-wise extraction of endmembers. For this purpose we make use of multitemporal data and the knowledge of the abundance maps. In the next section, we explain the proposed approach for the band-wise endmember extraction using multi-temporal data (BEEM).

5.3 Proposed Approach for Endmember Extraction

In this section, we discuss our approach for accurate estimation of the endmembers by making use of multitemporal data of the same scene. Since the dataset is acquired over the same area, we assume that the endmember matrix **M** remain same for the entire set of K data cubes, with the variations in the data $\mathbf{r}$ are due to the changes in their abundances. Using the LMM, the endmember values in each band together with the abundances across the bands at different pixel locations result in the data cube. We form an overdetermined set of equation to estimate the signatures of the spectrally distinct materials across the bands using the additional information present in the multi-temporal data, thereby improving the accuracy of endmember extraction. Here, the endmember matrix $\mathbf{M}$ is constant and abundances are varying with respect to time, i.e., they correspond to different fractions at a location in the datasets $\mathbf{N}_1, \mathbf{N}_2, ..., \mathbf{N}_K$, where, each $\mathbf{N}_i$ for $i = 1, 2, ..., K$ has the size of $l_1 \times l_2 \times W$. Considering a particular band, one may write the overdetermined set of equation as,

$$\mathbf{r_w} = \mathbf{A}\mathbf{m_w} + \mathbf{n}, \tag{5.2}$$

where $\mathbf{r_w}$ denotes $l_1 l_2 K \times 1$ vector corresponding to pixel values of the same band images. This vector is formed by lexicographically ordering of K data cubes and stacking them. Here, $l_1 \times l_2$ represents pixel values of a specific band and K is the number of images. $\mathbf{m_w}$ is a vector of size $e \times 1$ representing endmembers in that band. The matrix $\mathbf{A}$ has a size of $l_1 l_2 K \times e$ that has the abundances corresponding to different times. Finally, $\mathbf{n}$ is the additive white Gaussian noise vector of size $l_1 l_2 K \times 1$. Now, the endmembers $\mathbf{m_w}$ of size $e \times 1$ corresponding to a specific band are updated by using the following constrained minimization as,

$$\widehat{\mathbf{m}}_{\mathbf{w}} = \arg \min_{\forall \mathbf{m_w}} \|\mathbf{r_w} - \mathbf{A}\mathbf{m_w}\|_{\mathbf{2}}^{\mathbf{2}}, \forall W, \;\; \textbf{s.t.:} \;\; \widehat{m}_{i,j} \geq 0, \;\text{for } i = 1, ..., W \text{ and } j = 1, ..., e. \tag{5.3}$$

Minimization of equation (5.3) can be obtained by solving as nonnegative constraint least-squares (NCLS) as proposed in [202]. In this case the estimation $\widehat{m}_w$ is obtained by formulating the problem in the LS sense, thus considering the abundances as error-free. Note that the abundances being estimated using an algorithm can have errors. One may consider using TLS framework instead to take care of the possible errors in the abundnace matrix. However, in this approach we consider the abundances as error-free to estimate the endmembers. This process is *band-wise* carried out over the entire dataset, i.e., e endmembers are estimated using the same band-images from the dataset. For example, in order to obtain e endmember values for the third-band, we use K images of the third band among the K available data cubes. Thus an overdetermined system of equations are written for each band, where the abundance matrix $\mathbf{A}$ corresponds to abundances from each data and the vector $\mathbf{r_w}$ forms the reflectance at the same location in different bands. Now, the endmember matrix $\mathbf{M}$ is estimated by using the pixels values (reflectances) for each spectral band over the entire dataset. Thus, we call this approach as Band-wise

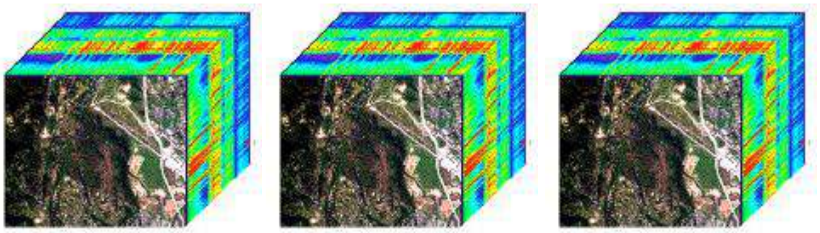

Data acquired on date “1”

Data acquired on date “2”

Data acquired on date “3”

Figure 5.1: An illustration of multiple hyperspectral measurements by an exemplary dataset.

Endmember Extraction using Multi-temporal data (BEEM). Although the signatures are spectrally overlapped, the endmember matrix represents the dominant reflectance by each material in each band (see equation (5.1)). We exploit the spatial and temporal variations in reflectance of the scene over each spectral band in order to obtain estimate of $\mathbf{M}$. This in turn makes the endmembers to satisfy a large number of linear equations as given in equation (5.3) and hence provides a better estimate of $\mathbf{M}$.

We now illustrate the BEEM using an example. Consider a multi-temporal data as shown in Figure 5.1. It has 3 hyperspectral measurements of the same scene, i.e. N_1, N_2 and N_3. Let each of the N_i have 224 bands, and a band-image in a N_i is of size 75×75 pixels. Given 3 endmembers over the scene, the resultant abundance maps for each N_i is $75 \times 75 \times 3$, i.e. a matrix of 5625×3 and hence the abundance matrix for the dataset ($\mathbf{A}$) is of size 16875×3. The size of endmember matrix to be recovered is 224×3. Corresponding to band-1 from N_1, N_2 and N_3, the system of linear equations is as under

$$\begin{bmatrix} r_{1,1} \\ r_{1,2} \\ \vdots \\ r_{1,5625} \\ r_{2,1} \\ r_{2,2} \\ \vdots \\ r_{2,5625} \\ r_{3,1} \\ r_{3,2} \\ \vdots \\ r_{3,5625} \end{bmatrix} = \begin{bmatrix} \alpha_{1,1} & \alpha_{2,1} & \alpha_{3,1} \\ \vdots & \vdots & \vdots \\ \alpha_{1,2} & \alpha_{2,2} & \alpha_{3,2} \\ \vdots & \vdots & \vdots \\ \alpha_{1,3} & \alpha_{2,3} & \alpha_{3,3} \\ \vdots & \vdots & \vdots \end{bmatrix} \times \begin{bmatrix} m_{1,1} \\ m_{1,2} \\ m_{1,3} \end{bmatrix}. \tag{5.4}$$

Here, $r_{i,1}, r_{i,2}, ..., r_{i,5625}$, for $i = 1, 2, 3$, represent the reflectance corresponding to 3 images of the band-1. The matrix of abundances has the abundances corresponding to the entire dataset, and $[m_{1,1}, m_{1,2}, m_{1,3}]^T$ represent the endmembers of the band-1. The equation (5.4) is used to formulate the NCLS minimization as given in equation (5.3) in order to solve for the $m_{1,1}, m_{1,2}, m_{1,3}$. This process is band-wise repeated over the 224 band images to recover the endmember matrix of size 224×3 as given in equation (5.3).

5.4 Experimental Analysis

In this section we demonstrate the efficacy of our approach for endmember extraction. Since the data corresponding to a real scene at different times was unavailable, we conducted experiments by simulating it using the real hyperspectral signatures. The Hyperspectral Data Retrieval and Analysis (HYDRA) Synthesis tool package [217] is used to generate the dataset for the experiments.

The spectral signatures of concrete-wtc01-37a.27883, cedar-gds357.27723 and board-gds362.29402 were selected as the signatures. These are contiguously spreaded in 2151 bands over the 400-2500 nm range. The endmembers are available at the USGS spectral library [85] and the HYDRA has incorporated them as a part of the package. The three abundance maps each of size 64×64 are generated using the spherical Gaussian field as available in the HYDRA package. The linear combinations of the signatures and the known abundance maps yield a hyperspectral data cube of size 64 × 64 × 2151 and it is denoted as data-1. In order to generate the data corresponding to different time instant, we use the same set of endmembers but with different abundances. Thus generating another cube of size 64 × 64 × 2151 and it is denoted as data-2. These datasets simulate the scenario of possible temporal variations in the scene occurred over the period. The abundance maps used to generate the data-1 are shown in Figure 5.2 (a), and Figure 5.2 (b) are the maps used to generate the data-2. Each abundance map is of size 64 × 64 pixels.

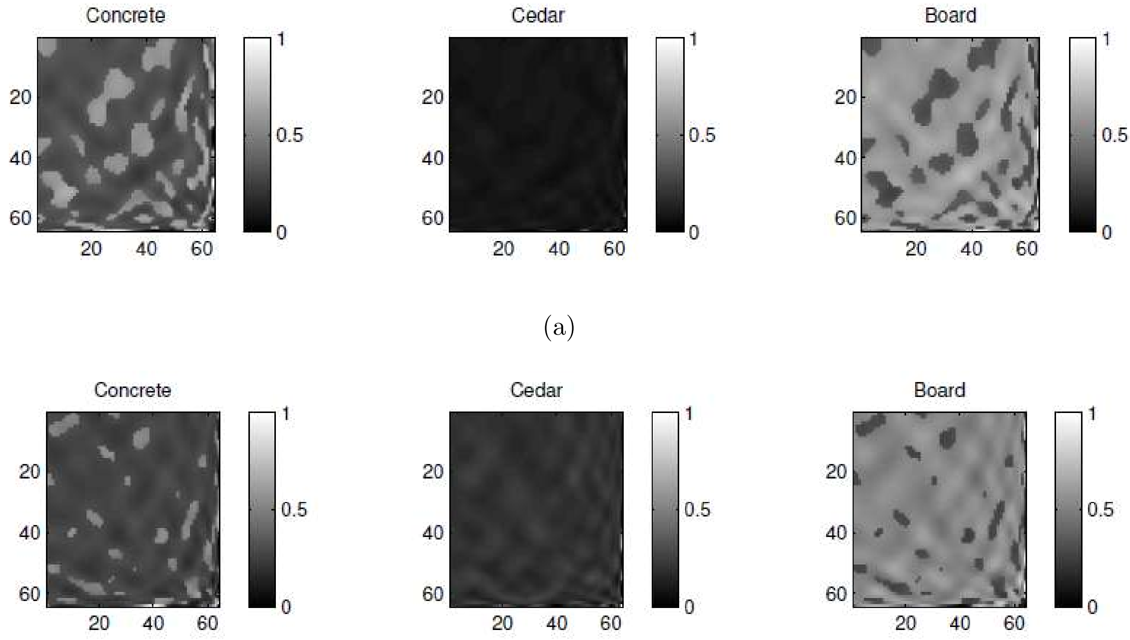

(a)

(b)

Figure 5.2: Ground truth abundance maps for the multi-temporal data: abundance maps for (a) data-1, and (b) data-2.

We conducted the experiments by adding different noise levels in the dataset and compared the performance with the state-of-art algorithms, i.e., VCA [102], MVC-NMF [111], and AGES [158] for extracting the spectral signatures constituting the estimated endmember matrix $\widehat{\mathbf{M}}$. We use the MATLAB implementations of the VCA available online in [218] while the MVC-NMF, and the AGES are implemented as per the descriptions of the algorithms with the recommended parameter settings in the literature.

For extracting the endmembers, the VCA works on convex geometry applying only in the spectral space of the data, and the MVC-NMF simultaneously solves for both endmembers and abundances in a regularization framework. The AGES starts with a random endmember matrix and estimate sum-to-one constrained abundances in the Langragian framework by dropping the nonnegativity constraint inherent to them. Then by using these partially constrained abundances, it estimates the endmembers in a greedy manner. Our proposed algorithm uses temporal changes in the reflectance in addition to the spatial/spectral information over a set of band in order to estimate endmember reflectance. Note that the VCA does not require abundances to estimate the endmembers while MVC-NMF approach jointly estimates the endmembers and abundances using a volume prior on the solution. On the other hand, AGES uses the initial abundances which are partially constrained wherein our approach make use of temporal data characteristic as well as fully-constrained abundances for estimating the endmembers.

In our experiments, endmembers are extracted by adding different levels of noise in the data, and the estimated endmembers are compared with the ground truth values as well as those estimated by using the other approaches. Figure 5.3 shows the ground truth signatures for the three endmembers along with the extracted spectra for noise variances σ^2 of 0.001 and 0.01, respectively. It can be observed from the graphs shown in Figure 5.3 that the proposed approach performs better when compared to the other approaches under the noisy conditions. This is due to the restriction imposed by using a large set of equations while estimating the endmembers. Similarly, Figure 5.4 shows the performance comparison of our approach with the other approaches for the data-2. Since the AGES method has comparable performance to the MVC-NMF approach, we have not displayed the results of this method in Figures 5.3 and 5.4.

In order to assess the performance of the proposed approach quantitatively, we used the following measures: root mean squared error (RMSE) [106], spectral angle mapper (SAM) [107] and spectral information divergence (SID) [108]. The quantitative comparison is shown separately for each data. Table 5.1 shows the performance using the data-1 while Table 5.2 is for the data-2. The error is calculated between the ground truth values and estimated values, and the average error is considered for each endmember separately as listed in the tables. It can be seen from the tables that the proposed approach performs better than the other approaches.

In our approach of endmember extraction, we use the entire dataset while the other approaches in the literature extract endmember matrix separately for each data cube.

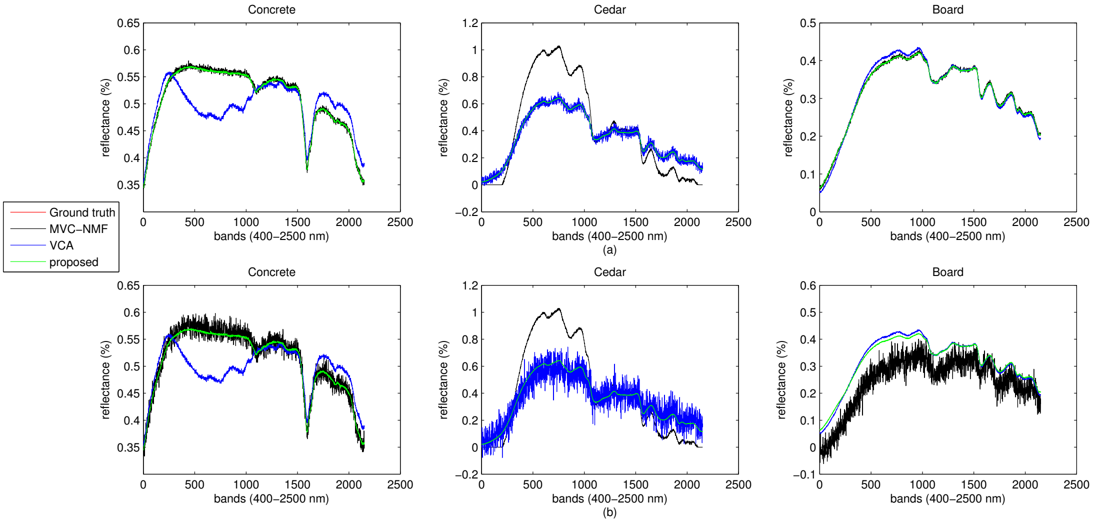

Figure 5.3: Plots of bands versus reflectance (spectral signatures) using different approaches on data-1 at noise levels of (a) $\sigma^2 = 0.001$, and (b) $\sigma^2 = 0.01$. Note that the endmembers extracted using the proposed approach are same for data-1 (Figure 5.3) and data-2 (Figure 5.4) since it uses band-wise information from both the datasets and abundances.

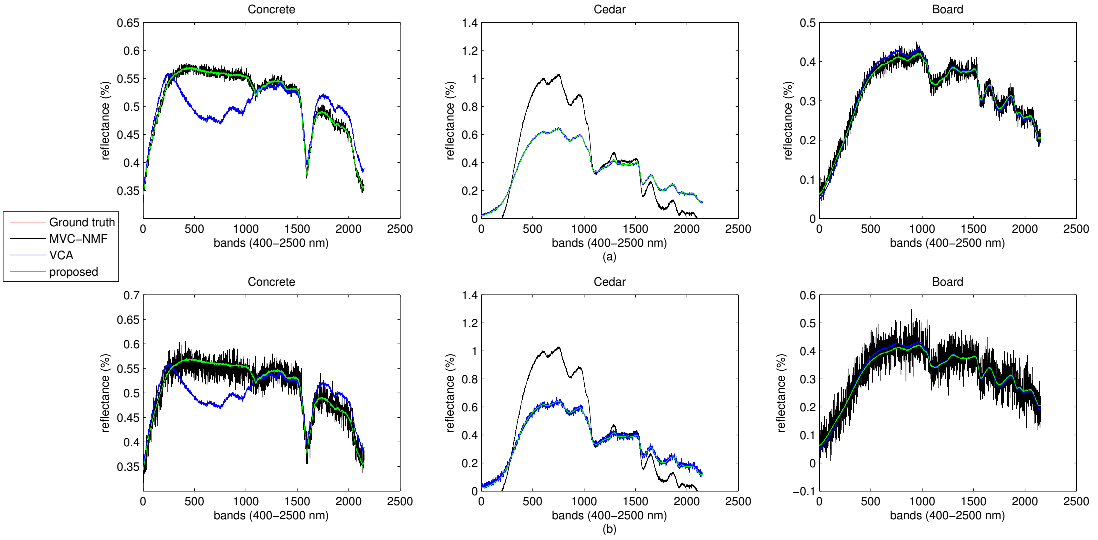

Figure 5.4: Plots of bands versus reflectance (spectral signatures) using different approaches on data-2 at noise levels of (a) $\sigma^2 = 0.001$, and (b) $\sigma^2 = 0.01$. Note that the endmembers extracted using the proposed approach are same for data-1 (Figure 5.3) and data-2 (Figure 5.4) since it uses band-wise information from both the datasets and abundances.

Hence, we now show the comparison when the entire dataset is used in these methods for extracting endmembers. We carry out an experiment wherein both the data cubes are combined and are used to estimate the endmembers in other approaches. Table 5.3 shows the comparison in terms of average error scores where the endmembers are estimated from a combined data, i.e., combining the data-1 and data-2. Our proposed algorithm better

Table 5.1: Average error scores for endmember extraction using the data-1 with additive Gaussian noise variance of $\sigma^2 = 0.01$.

Algorithm	$\widehat{\mathbf{M}}$		
	concrete	cedar	board
	RMSE [106]		
VCA [102]	0.0138	0.0700	0.0816
MVC-NMF [111]	0.0124	0.0637	0.0721
AGES [158]	0.0159	0.0737	0.0910
proposed	0.0112	0.0145	0.0026
	SAM [107]		
VCA [102]	1.3042	10.2068	9.3162
MVC-NMF [111]	1.2986	10.0700	9.6347
AGES [158]	2.9621	12.3054	11.4582
proposed	0.2162	4.1352	0.2155
	SID [108]		
VCA [102]	$5.2000e^{-06}$	$1.0147e^{-05}$	$1.9845e^{-05}$
MVC-NMF [111]	$5.3255e^{-06}$	$1.0053e^{-05}$	$1.4821e^{-05}$
AGES [158]	$7.2213e^{-06}$	$3.3324e^{-05}$	$2.8532e^{-05}$
proposed	$1.0264e^{-05}$	$1.8316e^{-05}$	$1.2187e^{-05}$

Table 5.2: Average error scores for endmember extraction using the data-2 with additive Gaussian noise variance of $\sigma^2 = 0.01$.

Algorithm	$\widehat{\mathbf{M}}$		
	concrete	cedar	board
	RMSE [106]		
VCA [102]	0.0163	0.0406	0.0131
MVC-NMF [111]	0.0188	0.0392	0.0102
AGES [158]	0.0241	0.0475	0.0221
proposed	0.0112	0.0145	0.0026
	SAM [107]		
VCA [102]	1.7454	7.0662	1.8764
MVC-NMF [111]	1.3280	6.7896	2.1832
AGES [158]	2.1456	8.3657	2.4216
proposed	0.2162	4.1352	0.2155
	SID [108]		
VCA [102]	$1.2207e^{-05}$	$3.4479e^{-05}$	$6.3064e^{-05}$
MVC-NMF [111]	$1.1004e^{-05}$	$2.1943e^{-05}$	$6.0291e^{-05}$
AGES [158]	$1.2312e^{-05}$	$3.9233e^{-05}$	$7.2041e^{-05}$
proposed	$0.0264e^{-05}$	$0.8316e^{-05}$	$1.2187e^{-05}$

restricts the solution space by utilizing the temporal characteristics along with the spatial and spectral information.

Finally, we reconstruct the datasets using respective ground truth abundances and the

Table 5.3: Average error scores for endmember extraction on the combined data with additive Gaussian noise $\sigma^2 = 0.01$.

Algorithm	$\widehat{\mathbf{M}}$		
	concrete	cedar	board
	RMSE [106]		
VCA [102]	0.0170	0.0410	0.0139
MVC-NMF [111]	0.0194	0.0421	0.0126
AGES [158]	0.0216	0.0512	0.0269
proposed	0.0112	0.0145	0.0026
	SAM [107]		
VCA [102]	1.2143	7.1322	1.9421
MVC-NMF [111]	1.3456	7.8063	2.2431
AGES [158]	2.3255	7.9982	3.7535
proposed	0.2162	4.1352	0.2155
	SID [108]		
VCA [102]	$2.02091e^{-05}$	$3.7479e^{-05}$	$6.6842e^{-05}$
MVC-NMF [111]	$2.4421e^{-05}$	$2.9342e^{-05}$	$6.9892e^{-05}$
AGES [158]	$3.4324e^{-05}$	$3.9342e^{-05}$	$8.9233e^{-05}$
proposed	$0.0264e^{-05}$	$0.8316e^{-05}$	$1.2187e^{-05}$

estimated endmembers as obtained from the different approaches, i.e., VCA, MVC-NMF, and AGES. The results are compared with the proposed approach. Figure 5.5 and Figure 5.6 show the DRE maps (in terms of RMSE) for the data-1 and the data-2, respectively, for noise variance of $\sigma^2 = 0.01$. The average errors and standard deviations are mentioned on the top of each figure. It can be observed that the average errors and their standard deviations using the proposed approach are less when compared to other approaches.

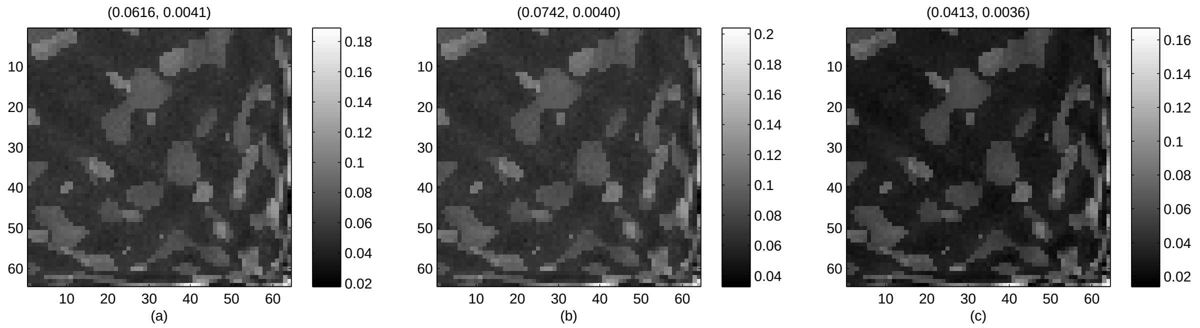

Figure 5.5: DRE maps (in terms of RMSE) for data-1 with $\sigma^2 = 0.01$: DRE map using (a) VCA [102], (b) MVC-NMF [111]/AGES [158], and (c) proposed approach.

Before we conclude, it may be of interest to know the reason for using the abundances for estimating the endmembers, although in general abundances are estimated by making

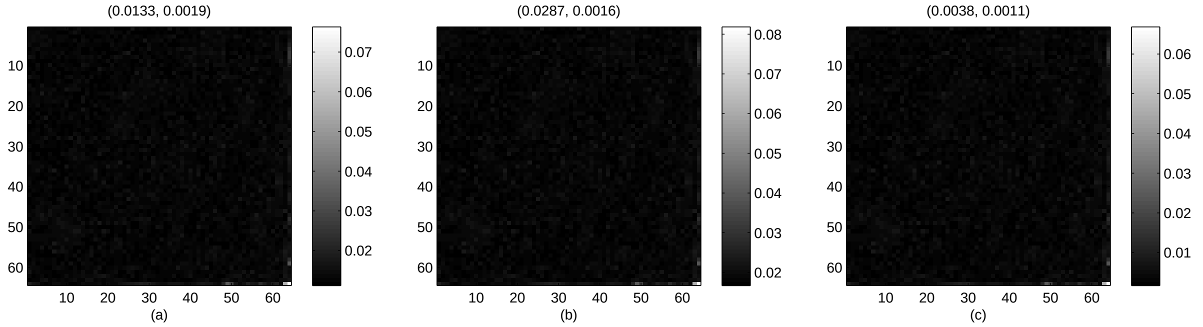

Figure 5.6: DRE maps (in terms of RMSE) for data-2 with $\sigma^2 = 0.01$: DRE map using (a) VCA [102], (b) MVC-NMF [111]/AGES [158], and (c) proposed approach.

use of known/estimated endmembers. Most of the approaches estimate the endmembers using only the data. One may view our algorithm as the one that can be used to improve the estimate of the endmembers obtained from the other approaches which do not make use of the abundances. Using a multi-temporal data, endmember matrix $\mathbf{M}$ and hence the abundances can be estimated using the state-of-art approaches. Now, using the dataset and the estimated abundances as done in our approach, the $\mathbf{M}$ matrix can be refined.

5.5 Conclusions

We presented a new algorithm for extracting the endmembers using the multi-temporal hyperspectral data of same scene. The knowledge of estimated abundance maps are utilized for constructing the set of overdetermined set of equations. Results of simulations conducted on synthetic dataset with different levels of additive white Gaussian noises demonstrated the effectiveness of the proposed algorithm when compared with the state-of-art approaches.

A limitation of the proposed algorithm is that it depends upon the availability of abundances of the scene. Secondly, the problem of identifying the number of endmembers in a scene is not yet discussed in the thesis. Both these problems are solved in the next chapter which gives us a complete solution, given the data. The proposed algorithm in this chapter will be used in the next chapter wherein we solve the complete spectral unmixing including estimation of the number of endmembers.

Chapter 6

Iterative Bootstrapping: A Unified Framework for Complete Spectral Unmixing of Hyperspectral Data

In this chapter, we propose a novel approach for simultaneous estimation of number of endmembers, their signatures and corresponding abundances, by exploring the spatial, spectral as well as temporal characteristics of the hyperspectral data over the same area. A linear mixing model (LMM) with the additive white Gaussian noise is considered as the data model. Our work is based on following observations: 1) endmembers together with their abundances form the hyperspectral data, and 2) temporal change in the pixel reflectance is due to variations in abundances over the period of time [8, 9, 11]. A bootstrapping technique inspired from the linear electronics theory is employed to iteratively improve the estimates of all the three entities within a two-stage framework. A rough estimate obtained in the fist stage works as an effective input to the second stage that improves the estimation by incorporating the appropriate constraints and prior information on the solution. Given the data, in stage one we obtain a set of initial endmembers using orthogonal subspace projection (OSP) incorporating the number of endmembers as the lower bound set by the principal eigen-vectors of the data covariance matrix. Assuming them as noisy estimates they are used to find initial abundances using the total least squares - Tikhonov (TLS-Tikhonov) regularization approach that considers the error in data as well as in endmembers. Second stage involves refinement of both the endmembers and abundances. Here, we first carry out band-wise endmember extraction using multi-temporal data (BEEM) using the initial abundances and obtain a constrained solution that gives improved endmembers. These are then incorporated in maximum *a posteriori* (MAP) with the *data-dependent* Huber - Markov random field (*d*HMRF) prior to further improve the abundances. Finally, the data reconstruction error (DRE) is used as a positive feedback to vary the number of endmembers. This feedback operation referred as *bootstrapping* is repeated on the two-stage operation until the DRE between the available and reconstructed reflectance is minimum. This process of iterative bootstrapping (IB) converges to an optimum solution (in the least-squares sense) for the complete spectral unmixing. We demonstrate the proposed work using multi-temporal datasets simulated using the real signatures of the USGS spectral library, and the results are compared with two standard hyperspectral unmixing processing chains. The proposed approach works as a self-regulatory mechanism for the complete spectral unmixing as well as serves as a basis to find the temporal changes in a hyperspectral scene based on changes in the abundances contributing to the scene reflectance over a period of time [10].

6.1 Introduction

Given the data, complete spectral unmixing solves for the three unknowns, i.e., it starts by identifying number of spectrally distinct materials in the data followed by extracting their spectral signatures called *endmembers* and finally estimating the corresponding ground cover fractions called *abundances*. The efficacy of the complete spectral unmixing can be assessed by checking the error between the available (or ground) reflectance and the reflectance reconstructed using the estimated unmixed components. Solving this inverse ill-posed problem using the mixing model poses major challenges due to the following factors: 1) variations in atmospheric conditions, sensor noise, material decomposition, location, and surrounding materials lead to inconsistent set of equations, 2) relatively larger IFOV and existence of mixed pixels due to altitude of the sensor makes the source separation difficult, and 3) the number of endmembers being significantly less than the available contiguous bands results in larger number of equations than the unknowns. Traditionally, the problem of linear spectral unmixing has been involved in estimating the three entities separately within a hyperspectral unmixing processing chain [5, 87, 86].

Recently, attempts have been made by the researchers on joint estimation of the number of endmembers and abundances [159], the endmembers and abundances [160, 111, 161], and a study on the impact of initial endmembers in searching the number of endmembers and their signatures [162]. It is interesting to note that many of the approaches proposed for spectral unmixing make use of a single hyperspectral data cube of the scene captured at a time [5, 87, 86]. On the other hand, multi-temporal data in the remote sensing area is investigated mainly for detecting changes in an area over a period of time [219, 220, 221, 222, 18, 223] in order to better understand the scene. In the proposed work we show that one can obtain the complete solution for spectral unmixing by using the hyperspectral data captured over the same area at different times.

Generally the scene change is due to variations in its contents, illumination angles, weather conditions, time of a day and/or date including seasonal effects. The important changes observed in hyperspectral data correspond to materials reflectance of the scene [10]. Since endmembers together with the abundances constitute the pixel reflectance (intensities) in a hyperspectral imagery, such changes can be either due to variations in the both or due to scene abundances. Hence, it is a challenge to perform complete spectral unmixing using multitemporal data [8]. Researchers have recommended to explore statistical methods and Markov random field (MRF) based prior information to account for no-change in the data at different times [8, 10]. In this paper, we consider a case wherein endmembers remain same and the changes in the scene are due to their abundances. This is a practical scenario which is observed due to repetitive data acquisition within a season of a year [8, 9, 11]. Our work includes the statistical/MRF based methods in addition to the least-squares based minimization in order to better constrain the solution.

For complete spectral unmixing, the first step is to find the number of endmembers which often requires the knowledge of experts and/or ground survey. The task becomes difficult for physically inaccessible areas on the earth. Comparing the hyperspectral imaging with the pigeon-hole principle, the number of endmembers (pigeons) is found to be significantly less than the available bands (pigeon-holes). Hence, in general, it is difficult to estimate the number of endmembers exactly and a reasonable estimate can be obtained based on trial-and-error criterion [77, 224]. The researchers have tried to determine the same by using the concept of virtual dimensionality (VD) of the data [79], in which a binary hypothesis is formulated by the eigenvalues of data correlations and covariance matrices. An eigen decomposition of estimated correlation matrices of the data and Gaussian noise for finding the number of endmembers is proposed in [80]. The method considers the noise covariance while estimating the number of spectrally distinct signatures. This method is well-known as HySime and it estimates the subspace of the data in the minimum mean-squared sense. In all the above approaches, the presence of noise in hyperspectral data affects the performance. In [159] a hierarchical Bayesian model is proposed in which the problem is formulated as constrained linear regression. Though the method simultaneously estimates the number of endmembers and abundances, it requires knowledge of endmembers. Recently, greedy algorithms have also been proposed using the sparse regression formulation [83, 84].

In many instances the signatures for the materials, i.e., endmember matrix elements, are available in a digital spectral library [85] or they can be extracted from the data using various algorithms [5, 86, 87, 109, 111]. The approaches for the endmember extraction are discussed in Chapter 5 that also introduced a new algorithm called BEEM. In most of these cases the number of endmembers is *a priori* known. Knowing the endmembers, unmixing can be done by estimating the corresponding abundances at each location. Since the abundances represent the fractions (weights) of the endmembers, they are required to satisfy nonnegativity constraint due to the passive remote sensing. Apart from this, the abundances must sum-to-one at each pixel location in the scene. Hence, it is difficult to solve this inverse problem and obtain a closed-form solution. Various *algorithms* for unmixing have been developed [117, 119, 74, 122, 126, 129, 130, 131, 132, 133, 134, 135, 157]. This is discussed in Chapter 3 that proposed TLS-Tikhonov approach [131], and the MAP-*d*HMRF approach [135, 157] proposed in Chapter 4 of this thesis.

In recent times, many researchers have started exploring multi-temporal unmixing of the hyperspectral data. An FCLS based unmixing is applied to multi-temporal hyperspectral data in [8] for the change detection. Their algorithm was tested on the data acquired using compact airborne spectrographic imager (CASI) in North Research Farm of Mississippi State University. An application of multi-temporal unmixing is shown in [9] for finding the vegetation index from the remotely sensed data. More recently, an unmixing analysis using nonnegativity constraint least-squares has been demonstrated in [11] for Hyperion images captured over Guanica dry forest in Puerto Rico. These approaches demonstrated results showing changes in the scene due to the variations in abundances over a period of time. But a limitation of these methods is that they require prior knowledge about the endmembers in a scene. An approach involving the spectral variability of the endmembers within the scenes while using the temporal data is proposed in [163]. However, no attempts have been made to use the multi-temporal data to solve for all the three entities in a single algorithm.

Few researchers have attempted the joint estimation of the endmembers and corresponding abundance maps. Such a joint estimation is formulated as a biconvex optimization problem in [160]. This is a heuristic algorithm based on alternatively updating endmember and abundance matrices via projected subgradients. To this end, fully Bayesian hierarchical algorithm is proposed in [161] which uses a computationally expensive generalized Gibbs sampler. The method illustrates the nonuniqueness of the solution while attempting the joint estimation.

In this chapter, by considering a linear data model for hyperspectral imagery we simultaneously solve for number of endmembers, their signatures and corresponding abundances. We consider a season of a year when the endmembers remain the same while changes in the scene reflectance are due to variations in their abundances. This is inspired from a real scenario recorded by the CASI over the North Research Farm of Mississippi State University from August to September in the year 2008 [8]. Our work uses an iterative bootstrapping approach as a positive feedback mechanism. Following are the salient features of the proposed IB approach, which distinguish it from the existing state-of-art algorithms, i) the method simultaneously estimates all the three unmixed components, ii) it considers the effects of noise by minimizing the data reconstruction error (DRE) iteratively in the least-squared sense for ensuring the correctness of the estimated number of endmembers, since the unmixing is carried out by satisfying both nonnegativity and sum-to-one constraints on the abundances [122, 99, 158], hence the reconstructed data points lie within the simplex form by the reconstructed data vectors, iii) the regularized TLS approach ensures a better initial estimate of abundances compared to the least-squares estimation when the endmembers are also perturbed along with the noise in the data, iv) band-wise endmember extraction performed using the temporal characteristics in addition to the spatial/spectral information over a set of data, acts as additional constraint on the endmembers, and v) the MAP-dHMRF method not only satisfy the fully constrained requirement but also incorporate appropriate prior on abundances in order to overcome the ill-posedness. Note that unlike the existing methods that solve for at most two entities, our algorithm simultaneously solves for all the three unknowns. This is a difficult problem and the novelty of our approach lies in the use of multi-temporal data including suitable prior information in the bootstrapping framework to improve the accuracy of estimation.

6.2 Overview of the proposed framework

In this section we briefly explain the proposed method for the complete spectral unmixing which is utilizing the temporal information of the data in addition to the spatial as well as spectral characteristics. We pose it as solving an inverse ill-posed problem involving overdetermined set of linear equations. For this purpose, we extend the linear mixing model (LMM) for the multi-temporal data, i.e., consider a set of spectrally distinct signatures (endmembers) undergo appropriate transformations represented by their abundances over a period of time. This process yields a set output vectors representing reflectance at different wavelengths over the scene. In our case, this transformation is equivalent to applying a linear operator on a vector to yield another vector in the same domain. Here, varying abundances at different locations represent the linear operators and the vector representing the endmembers is transformed to represent the resultant mixed reflectances within the IFOV of the sensor over the time.

In the LMM, the abundances are constrained by nonnegativity and sum-to-one at each pixel location. Hence, these can be conveniently represented by sample functions of Dirichlet process [136]. Further, generally the number of endmembers (e) present in a scene is significantly less than the total number of bands W. Therefore, the transformation matrix (linear operator at a pixel) representing the abundance fractions constitutes a sparse matrix $\mathbf{F}_{\boldsymbol{\alpha}}$ which has W number of rows that correspond to shifted versions of one of the sample functions of the Dirichlet process. The transformation matrix $\mathbf{F}_{\boldsymbol{\alpha}}$ can be represented as,

$$\mathbf{F}_{\boldsymbol{\alpha}} = \begin{pmatrix} \alpha_1 & \alpha_2 & \cdots & \alpha_e & 0 & 0 & 0 & 0 & 0 & 0 & \cdots & 0 & 0 \\ 0 & 0 & \cdots & 0 & \alpha_1 & \alpha_2 & \cdots & \alpha_e & 0 & 0 & \cdots & 0 & 0 \\ \vdots & \vdots & \vdots & \vdots & \vdots & \vdots & \vdots & \vdots & \ddots & \vdots & \vdots & \vdots & \vdots \\ 0 & 0 & \cdots & 0 & 0 & 0 & 0 & 0 & 0 & \alpha_1 & \alpha_2 & \cdots & \alpha_e \end{pmatrix}_{W \times We}$$

$$\textstyle\sum_{i=1}^{e} \alpha_i = 1 \text{ in each row, where } \alpha_i \in [0,1].$$

Here, $\alpha_1, \alpha_2, ..., \alpha_e$ represent the set of abundances corresponding to the column vectors $\mathbf{m_1}, \mathbf{m_2}, ..., \mathbf{m_e}$, of endmember matrix $\mathbf{M}$. Considering a hyperspectral data cube which has W number of spectral bands each of size $l_1 \times l_2$ pixels, one may write a linear system of equations at every location as,

$$\mathbf{r} = \mathbf{F}_{\boldsymbol{\alpha}}\mathbf{m}, \;\; \mathbf{F}_{\boldsymbol{\alpha}}\colon \mathbf{m}^{\mathbb{R}^+} \rightarrow \mathbf{r}^{\mathbb{R}^+} \tag{6.1}$$

where, $\mathbf{r}$ represents the data vector of size $W \times 1$, and $\mathbf{F}_{\boldsymbol{\alpha}}$ is the $W \times We$ sparse matrix. Here $\mathbf{m}$ is a vector of size $We \times 1$ representing lexicographically ordered rows of the endmember matrix of size $W \times e$. The input-output transformation given in equation (6.1) can be considered at every location to yield a reflectance data cube of size $l_1 \times l_2 \times W$. The endmember vector $\mathbf{m}$ combined with $\mathbf{F}_{\boldsymbol{\alpha}}$ at every pixel generate the corresponding output reflectance vectors forming a data cube. Let, $\mathcal{F}_{\boldsymbol{\alpha}-i}$ represents the abundance matrix considering all the locations at a given time. Thus applying different transformations $\mathcal{F}_{\boldsymbol{\alpha}-1}, \mathcal{F}_{\boldsymbol{\alpha}-2}, ..., \mathcal{F}_{\boldsymbol{\alpha}-K}$ on the endmembers $\mathbf{m_1}, \mathbf{m_2}, ..., \mathbf{m_e}$ we get $l_1 l_2 W$ reflectance vectors for each of the $\mathbf{N_1}, \mathbf{N_2}, ..., \mathbf{N_K}$ data cubes. This indicates that appropriate transformations on the same endmembers corresponding to a scene lead to different valued data cubes. We make use of these data cubes of the same scene which are acquired at different times in order to better constrain the endmember values while solving for them.

Now the complete spectral unmixing problem can be formulated as follows: given the K data cubes, find the number of endmembers, their signatures (i.e., endmember values in each band) and corresponding abundances at every location. By considering additive white Gaussian noise at each pixel location in a data cube, one can represent the linear mixing model (LMM) [38] as,

$$\mathbf{r} = \mathbf{M}\boldsymbol{\alpha} + \mathbf{n}, \tag{6.2}$$

where the spectral measurement $\mathbf{r}$ denotes a W-dimensional column vector same as in equation (6.1). Here, $\mathbf{M}$ represents the endmember signature matrix which has a size of $W \times e$. The weights for endmembers, i.e., the abundances can be represented by e-dimensional vector $\boldsymbol{\alpha} = [\alpha_1, \alpha_2, ..., \alpha_e]^T$, i.e. , α_i represents the fractional area covered by the i^{th} endmember. In equation (6.2), $\mathbf{n}$ corresponds to $W \times 1$ vector representing the white Gaussian noise of variance σ^2. Note that though equations (6.1) and (6.2) represent the same model, the endmember matrix $\mathbf{M}$ multiplies vector $\boldsymbol{\alpha}$ in (6.2) while in equation (6.1) an abundance matrix $(\mathbf{F}_{\boldsymbol{\alpha}})$ is multiplied with the vector representing endmember values.

In order to solve this inverse ill-posed problem, we incorporate the idea of bootstrapping from the field of electrical engineering. During the early days of research in linear electronics, a positive feedback process called bootstrapping technique was used for increasing the gain of an amplifier with a two-stage arrangement. It involves a feedback system in which a portion of an output from the second stage is fedback to the first stage (see Figure 6.2), that increases the input impedance of the circuit resulting in faithful amplification of the input signal. Thus, bootstrapping boosts the performance of the system without the need of external aids.

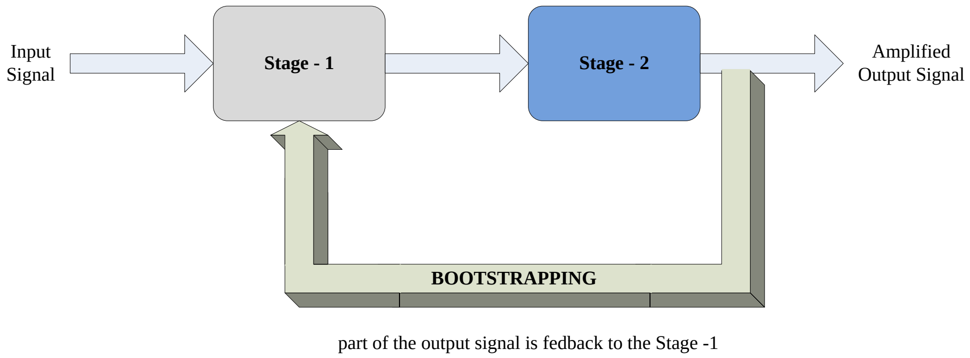

Figure 6.1: Bootstrapping: portion of the output signal is fedback to the Stage-1 increasing the gain of a two-stage amplifier.

In our approach, all the three entities to be estimated are utilized in bootstrapping in order to improve their estimation. A feedback in the form of error between the given reflectance (data) and the reflectance reconstructed using the estimated unmixed components is used to iteratively improve the solutions by changing the number of endmembers in every iteration. This feedback process repeats until the data reconstruction error (DRE) is minimum making it an iterative bootstrapping (IB) approach. In order to handle the severe ill-posedness in estimating the abundances, our approach uses TLS-Tikhonov approach for obtaining the initial abundance values. In the second stage, multi-temporal data are used to improve the estimation of endmember matrix using our band-wise endmember extraction using multi-temporal data (BEEM) algorithm. The improved endmembers are used to further enhance the abundances by using the MAP framework taking care of the ill-posedness in the unmixing. In our approach the first stage provides a rough estimate of the solution and works as an initial estimate for the second stage that uses additional constraints and appropriate prior on the entities to be estimated in order to enhance the accuracy of estimation.

In essence we use the multi-temporal data to estimate the endmembers, and the abundances are estimated at every pixel location. Advantages of the proposed approach are, 1) performs the blind decomposition of the given data under the well accepted linear mixing model, 2) carries out the complete spectral unmixing avoiding the necessity of one or more entity estimated from other approaches, 3) identifies number of endmembers without using *a priori* knowledge of scene-dependent parameters, and 4) the entire spectral unmixing process is carried out in a self-regulatory mechanism.

6.3 Proposed Method for Complete Spectral Unmixing

Figure 6.2 shows the complete block diagram of the proposed method. The input consists of K data cubes of the same scene acquired at different times. Using these, the proposed approach first computes an initial estimate for number of endmembers and their signatures. It is clear that since the data is contiguous in its spectral space, the column vectors of $\mathbf{M}$ may not be truly orthogonal, but one may assume linear independency of these vectors as they represent pure spectra of the constituent materials. This motivates us to use the principal component analysis (PCA) [50] on the data, wherein eigen-directions with significant eigen-values indicate the lower bound on the number of endmembers in the data. So to begin with, we apply the PCA on each data cube and select the initial estimate for number of endmembers. Since the hyperspectral data is highly correlated in the spectral space, we choose the eigen-vectors that correspond to 95% of total energy to decide on the number of principal components. This represents the lower bound on the number of endmembers and treated as an initial estimate $\hat{e}$.

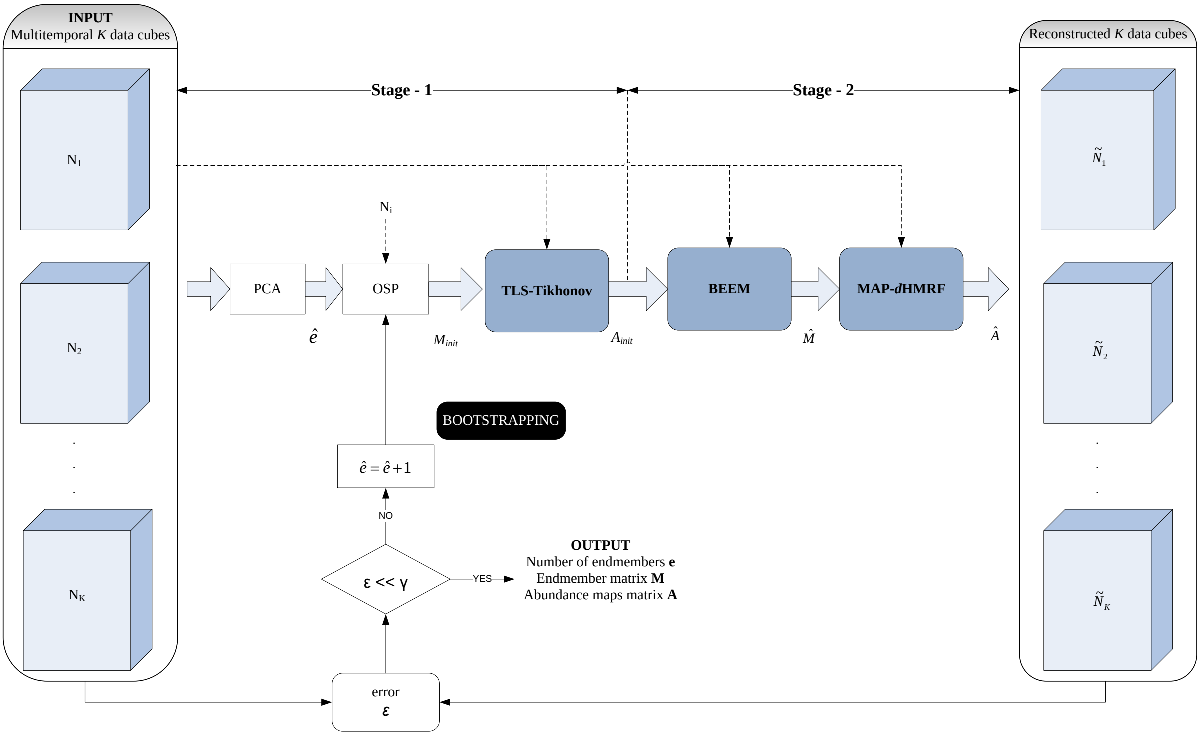

Figure 6.2: Block schematic of the proposed Iterative Bootstrapping (IB) method for complete spectral unmixing using multi-temporal hyperspectral data.

Once the initial number of endmembers is derived as $\hat{e}$, it is used in the OSP [96] algorithm to obtain an initial estimate of endmembers using the data cube having the smallest number of eigen-directions. It may be noted that one may use other state-of-art approaches like N-FINDR [98], AMEE [103] or VCA [102] to find the initial estimate for endmembers. Since OSP represents the pioneering approach among the existing state-of-art approaches, we resort to it for finding the initial endmembers. Using the available data and the number of endmembers, OSP proceeds by considering a pixel-vector having the largest norm as the first endmember from the data. The remaining endmembers are determined iteratively by exploiting orthogonality with respect to the available signatures within the data. However, this may result in poor estimate of endmembers under the noisy scenario [96]. Nevertheless, it gives us an initial set of signatures $\mathbf{M}_{init}$ which is then used in unmixing all the K data cubes that gives us the initial estimates of corresponding abundance maps. To do this, we consider perturbations in both the data and endmembers. Our TLS-Tikhonov regularization [131] approach is then applied to obtain the initial estimate of abundances at every pixel location in each data cube as,

$$\mathbf{A}_{init-i} = \left\{ \hat{\boldsymbol{\alpha}}_{init} = \arg\min_{\forall \boldsymbol{\alpha}} \|[\mathbf{M};\mathbf{r}] - [\mathbf{M}_{init};\mathbf{M}_{init}\boldsymbol{\alpha}]\|_F + \mu \left\|\mathbf{L}\boldsymbol{\alpha}_{(i,j)}\right\|_2, \forall\ l_1 \times l_2 \right\},\ \text{and } i = 1, 2, ...K \tag{6.3}$$

where, $\|.\|_F$ denotes the Frobenius norm of the matrix, μ is the regularization parameter, $\mathbf{L}$ is the matrix representation of the derivative operator, and $l_1 \times l_2$ denotes the number of pixel locations in the data cube. The physical constraints on the abundances are taken care of while minimizing the objective function given in (6.3). Further details are available in the Chapter 3. It can be seen that the minimization of equation (6.3) over the i^{th} data cube results in physically constrained abundances $\mathbf{A}_{init-i}$ by considering the noise in data as well as endmember signatures in the $\mathbf{M}_{init}$. We now have initial estimates for the endmembers ($\mathbf{M}_{init}$) of the scene and the abundances for each of the multi-temporal data cubes, i.e., K initial abundance cubes $\mathbf{A}_{init-1}, \mathbf{A}_{init-2}, ..., \mathbf{A}_{init-K}$, each having a size of $l_1 \times l_2 \times e$. Note that these cubes have the same set of abundances as those in $\mathcal{F}_{\boldsymbol{\alpha}-1}, \mathcal{F}_{\boldsymbol{\alpha}-2}, ..., \mathcal{F}_{\boldsymbol{\alpha}-K}$ matrices as already discussed in Section 6.2. We form the $\mathbf{A}_{init}$ matrix by first converting each of the $\mathbf{A}_{init-i}$ into a matrix of size $l_1 l_2 \times e$ and stacking all the resultant K abundance maps to form a matrix of size $l_1 l_2 K \times e$. This initial abundance matrix $\mathbf{A}_{init}$ which has the complete set of abundances of the multi-temporal data is utilized in obtaining an improved estimate of endmember matrix making use of the multi-temporal data. This approach to better estimate of endmembers is based on bandwise extraction.

Our algorithm of band-wise endmember extraction using multi-temporal data (BEEM) makes use of the entire K data cubes so that the changes occurred in the scene over the time period can be taken into consideration in order to improve the solution. The process of endmember extraction is carried out by assuming a linear mixing model (LMM) on the multi-temporal data. This is discussed in Chapter 5 of this thesis. One may note that $e << W$, so the the use of multi-temporal hyperspectral data better constrain the solution. This improves the estimates of endmembers even under the noisy conditions. The improved endmember matrix $\widehat{\mathbf{M}}$ is then used to further improve unmixing of all the data cubes, i.e., $\widehat{\mathbf{A}}$, using our MAP-dHMRF [157] approach at every pixel location in each data cube as,

$$\hat{\boldsymbol{\alpha}} = \begin{cases} \underset{\forall \boldsymbol{\alpha}}{\arg\min} \left[\dfrac{\left\| \mathbf{r} - \widehat{\mathbf{M}}\boldsymbol{\alpha} \right\|^2}{2\boldsymbol{\sigma}^2} + \lambda \displaystyle\sum_{i=0}^{e-1} \left| \alpha_i - \alpha_{(i+1 \ mod \ e)} \right|^2 \right], & \text{if } \alpha_d \leq \beta, \text{ and} \quad (6.4a) \\ \underset{\forall \boldsymbol{\alpha}}{\arg\min} \left[\dfrac{\left\| \mathbf{r} - \widehat{\mathbf{M}}\boldsymbol{\alpha} \right\|^2}{2\boldsymbol{\sigma}^2} + \lambda \displaystyle\sum_{i=0}^{e-1} \left(2 \left| \alpha_i - \alpha_{(i+1 \ mod \ e)} \right| \beta - \beta^2 \right) \right], & \text{if } \alpha_d > \beta \quad (6.4b) \end{cases}$$

$$\text{s.t.: } \textstyle\sum_{i=1}^{e} \hat{\alpha}_i = 1 \text{ and } \hat{\alpha}_i \in [0, 1].$$

$\forall \ l_1 \times l_2$ and for all data cubes.

Here $\alpha_d = \left| \alpha_i - \alpha_{(i+1 \ mod \ e)} \right|$ and β is a suitable threshold and λ are derived from the available data as discussed in our earlier work [157]. Carrying out the minimization of equations (6.4a) and (6.4b) yields $\widehat{\mathbf{A}}_\mathbf{1}$,$\widehat{\mathbf{A}}_\mathbf{2}$,...$\widehat{\mathbf{A}}_\mathbf{K}$, corresponding to $\mathbf{N_1}$,$\mathbf{N_2}$,...,$\mathbf{N_K}$, and collectively represented as $\widehat{\mathbf{A}}$ representing the estimated abundances for all the data cubes. Once the abundances are found, they along with the $\widehat{\mathbf{M}}$ are used to reconstruct the entire dataset, and the error (ϵ) is calculated between the reconstructed and the available reflectance in the K data cubes as

$$\epsilon = \frac{\mathbf{1}}{\mathbf{K}} \sum_{\mathbf{i=1}}^{\mathbf{l_1 l_2 K}} \left\| \mathbf{R_{Ni}} - \widetilde{\mathbf{R}}_{\mathbf{Ni}} \right\|_\mathbf{2} \quad (6.5)$$

where, $\mathbf{R_{Ni}}$ and $\widetilde{\mathbf{R}}_{\mathbf{Ni}}$ represent the available and the reconstructed data vectors at ith location. It is clear that a low value of the ϵ ensures the closeness of the $\widehat{\mathbf{M}}$ and $\widehat{\mathbf{A}}$, to their true ones, i.e., $\mathbf{M}$ and $\mathbf{A}$. A relatively high value of ϵ indicates a miss-fit for the model we have chosen. In our approach, $\widehat{\mathbf{M}}$ and $\widehat{\mathbf{A}}$ are estimated using appropriate constraints and the relevant additional information, hence according to the LMM, the possible reconstruction error could be due to use of incorrect number of endmembers, i.e., $\hat{e}$, [122, 99, 158]. Note that we have initialized the e with the least number of orthogonal directions, and hence this can be updated and the entire process of finding the endmembers and abundances can be repeated. This update is based on the data reconstruction error ϵ as in equation (6.5). This process of updating the number of endmembers and recalculating $\widehat{\mathbf{M}}$ and $\widehat{\mathbf{A}}$ iteratively involves a feedback called the *bootstrapping*. The entire procedure is repeated with the updated value of the $\hat{e}$ as $\hat{e} + 1$ till we obtain $\epsilon <<$

threshold γ ensuring the convergence in the least-squares sense [122]. This process is termed as iterative bootstrapping (IB). Since the minimization functions in the entire bootstrapping operation are quadratic, the convergence is guaranteed. We would like to mention here that since we employ regularization as well as additional constraints leading to a unique inverse mapping, the feedback mechanism used in the proposed IB technique works well avoiding the instability.

We now provide a geometric illustration for the working of the proposed IB approach using an exemplary data. For the sake of simplicity, we prefer to use a single data cube. Nevertheless, the explanation is equally applicable to the multi-temporal data. Figure 6.3 illustrates how the bootstrapping helps in gradually improving the solution.

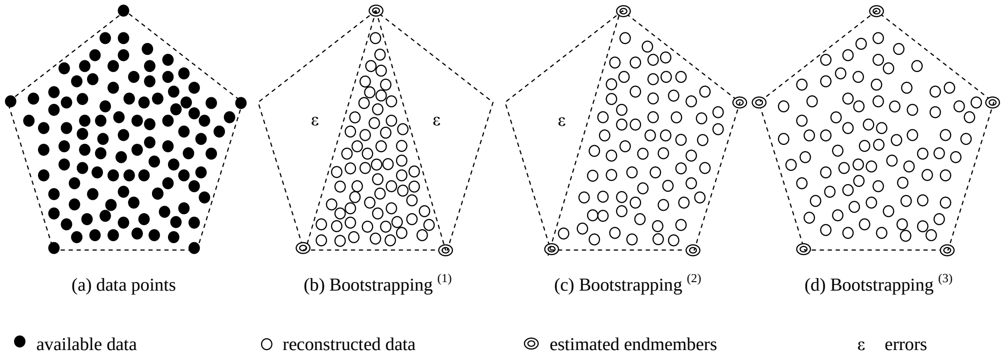

Figure 6.3: Geometric illustration of the proposed Iterative Bootstrapping (IB) approach for complete spectral unmixing: (a) data vectors represented as points in the W-dimensional Euclidean space with 5 endmembers shown as vertices of a polygon, and (b-d) bootstrapping with increasing number of endmembers to improve the solution.

Figure 6.3 (a) shows the remotely acquired hyperspectral measurements over the W contiguous bands and the data is represented as the points in the W-dimensional Euclidean space. We see that the use of linear mixing model (LMM) allows us to visualize the data in a convex cone formed by the endmembers. As shown in Figure 6.3 (a), there are 5 endmembers corresponding to spectrally distinct materials. Our algorithm is initialized by applying the PCA on this data and for the sake of illustration let us assume that there are 3 principal components. As discussed, the initial estimates of the endmembers and abundances are determined using the OSP and TLS-Tikhonov approach, respectively. This is followed by improved endmembers using the multi-temporal data (BEEM), and finally the abundances are recovered using the MAP-dHMRF. The entire data is reconstructed using these endmembers and abundances, and the data reconstruction error is calculated. This is depicted in Figure 6.3 (b) where it indicates that now the data has 3 endmembers with the corresponding improved estimates of abundances. It can be seen from the Figure 6.3 (b) that with the use of 3 endmembers, a significantly large error results in the data reconstruction. By using the iterative bootstrapping, the solution can be improved as illustrated in Figure 6.3 (c) and Figure 6.3 (d). Hence, the number of endmembers is increased by one, i.e., 4, and the entire process is repeated. Figure 6.3 (c) shows that the error is relatively reduced, but it is still significantly large. Once again $\hat{e}$ is increased by one and the bootstrapping is repeated. As shown in Figure 6.3 (d), the error in this case is significantly reduced resulting in improved endmembers and abundances.

6.4 Iterative Bootstrapping (IB) Algorithm

Here we give algorithmic steps involved in our method. Given the multi-temporal data, the proposed algorithm performs blind decomposition as illustrated by using Algorithm 1. The symbols $\hat{e}$, $\widehat{\mathbf{M}}$ and $\widehat{\mathbf{A}}$ are used to indicate estimated versions of number of endmembers, endmember matrix and abundance matrix of the data cubes, respectively. The symbol $\boldsymbol{\lambda}_W$ is used to indicate a W-dimensional vector of eigenvalues for a data cube, and $\widetilde{\mathbf{R}}_{\mathbf{N}}$ denotes a reconstructed data vector.

Algorithm 1 Iterative Bootstrapping

```
INPUT: Hyperspectral data cubes $\mathbf{N}_1, \mathbf{N}_2, ..., \mathbf{N}_K$.
OUTPUT: Number of endmembers $e$, endmember matrix $\mathbf{M}$ and abundance maps $\mathbf{A}_1, \mathbf{A}_2, ..., \mathbf{A}_K$.
 1: $\{\boldsymbol{\lambda}_W\}_{i=1}^{K} = \text{PCA}\left(\{\mathbf{N}_i\}_{i=1}^{K}\right)$.
 2: for $i = 1$ to $K$ do
 3:    set $\hat{e_i} = 0$.
 4:    for $j = 1$ to $W$ do
 5:       if $\boldsymbol{\lambda}_j \geq 0.95\left(\sum_{p=1}^{W} \lambda_p\right)$ then
            $\hat{e_i} = \hat{e_i} + 1$.
 6:       end if
 7:    end for
 8: end for
 9: $\hat{e} = \min(\hat{e_1}, \hat{e_2}, ....., \hat{e_K})$, and corresponding data cube is $\mathbf{N}$.
10: $\mathbf{M}_{init} = \text{OSP}\,(\mathbf{N}, \hat{e})$.
11: $[\mathbf{A}_{init-1}, \mathbf{A}_{init-2}, ..., \mathbf{A}_{init-K}] = \text{TLS-Tikhonov}\left(\{\mathbf{N}_i\}_{i=1}^{K}, \mathbf{M}_{init}\right)$.
12: Set $x = 1$.
13: for $n = 1$ to $K$ do
14:    for $i = 1$ to $l_1$ do
15:       for $j = 1$ to $l_2$ do
16:          $\mathbf{A}_{init}(x, :) = \mathbf{A}_{init-n}(i, j, :)$
17:          $x = x + 1$
18:       end for
19:    end for
20: end for
21: for $j = 1$ to $W$ do
22:    $\mathbf{R}_j(:, 1) = \{\mathbf{N}_i(:, :, j)\}_{i=1}^{K}$.
23:    $\widehat{\mathbf{m}}_{\mathbf{w}} = \arg\min_{\forall \mathbf{m}_{\mathbf{w}}} \|\mathbf{R}_{\mathbf{j}} - \mathbf{A}_{\mathbf{init}}\mathbf{m}_{\mathbf{w}}\|_{\mathbf{2}}$. s.t.: $\widehat{m}_{i,j} \geq 0$, for $i = 1, 2, ..., W$, and $j = 1, 2, ..., e$.
24:    $\widehat{\mathbf{M}}(j, :) = \widehat{\mathbf{m}}^{\mathbf{T}}$.
25: end for
26: $\left[\widehat{\mathbf{A}}_1, \widehat{\mathbf{A}}_2, ..., \widehat{\mathbf{A}}_K\right] = \text{MAP-}d\text{HMRF}\left(\{\mathbf{N}_i\}_{i=1}^{K}, \widehat{\mathbf{M}}\right)$.
27: for $n = 1$ to $K$ do
28:    for $i = 1$ to $l_1$ do
29:       for $j = 1$ to $l_2$ do
30:          $\widetilde{\mathbf{N}}_n(i, j, :) = \widehat{\mathbf{M}}\widehat{\mathbf{A}}_n(i, j, :)$
31:       end for
32:    end for
33: end for
34: for $i = 1$ to $l_1 l_2 K$ do
       $\epsilon \mathrel{+}= \frac{\mathbf{1}}{\mathbf{K}}\left\|\mathbf{R}_{\mathbf{Ni}} - \widetilde{\mathbf{R}}_{\mathbf{Ni}}\right\|_{\mathbf{2}}$
35: end for
36: if $\epsilon \ll \gamma$ then
       $e = \hat{e}$, $\mathbf{M} = \widehat{\mathbf{M}}$ and $\mathbf{A}_1 = \widehat{\mathbf{A}}_1, \mathbf{A}_2 = \widehat{\mathbf{A}}_2, ..., \mathbf{A}_K = \widehat{\mathbf{A}}_K$.
37: else
       $\hat{e} = \hat{e} + 1$ and go to step 10.
38: end if
STOP
```

6.5 Experimental Results

In this section we demonstrate the efficacy of our approach for simultaneous estimation of number of endmembers, their signatures and corresponding abundances. Due to unavailability of real data captured at different times, we experimented by simulating the dataset. The Hyperspectral Data Retrieval and Analysis (HYDRA) Synthesis tool package [217] is used to generate the dataset for the experiments. All the algorithms are run on a Desktop PC with Intel® Core$^{\text{TM}}$ i5-3210M CPU at 2.5 GHz with 4 GB of RAM.

Since the researchers have not attempted to solve for all the three entities using one algorithm, we compare our results with those spectral unmixing chains that combine the state-of-art algorithms for estimating the number of endmembers, their signatures and the corresponding abundances. These approaches include VD [79]+VCA [102]+FCLS [122] and HySime [80]+MVC-NMF [111]. We use the MATLAB implementations of the VCA and HySime algorithms available online in[218] and the VD implementation available in [225]. The FCLS and MVC-NMF are implemented as per the descriptions of the algorithms with the recommended parameter settings in the literature.

Though we are simulating the data, many physical models for understanding the materials based on the reflected energy have been developed [37]. The effects of the multi-temporal data acquisitions are modeled in [226, 10]. For our experiments, we considered seven endmembers namely Renyolds_tunnel_sludge, Green_slime, Cyanide_potassium_ferro, Plastic_grnhouse_roof, Montmorillonite_benzen, Cyanide_zinc, and Ammonium_chloride. These are contiguously spread over 480 bands in range of $400 - 2500$ nm. The signatures for the endmembers are available at the USGS spectral library [85] and the HYDRA has included them as a part of the package. Use of these seven spectral signatures gives us the endmember matrix $\mathbf{M}$ of size 480×7. By considering each band image of size 256×175 pixels, the abundance maps of the same size are generated using the spherical Gaussian field as available in the HYDRA package. The endmembers and the abundances are then combined using the LMM, i.e., $\mathbf{r} = \mathbf{M}\boldsymbol{\alpha}$, to generate the hyperspectral data cube of size $256 \times 175 \times 480$ and this is denoted as Data-1. In order to generate the data cube for the same scene at a different time instant, we keep the $\mathbf{M}$ constant but vary their abundances, thus generating another cube of size $256 \times 175 \times 480$ that is denoted as Data-2. These two data cubes simulate the scenario of temporal variations in the scene occurred within a season of a year. This is similar to a practical scenario found in the CASI data during the months of August and September 2008 [8]. In this period of time, the endmembers remain the same while changes in the scene are observed due to variations in their abundances. The experiments are conducted for the complete spectral unmixing by adding different levels of noise in the simulated dataset. Note that the data digital numbers are in the range of 0 to 1. The mean images having average reflectance at each pixel location for the Data-1 and Data-2 are shown in Figure 6.4 (a) and (b), respectively, with the endmembers marked in the respective scenes. Looking at the two images, we observe that the scene has undergone changes because the distribution of the endmembers has been changed. Table - 6.1 lists the locations of the endmembers in the multitemporal data. The ground truth endmembers are shown in Figure 6.5 in which we show the plots of bands versus the endmember reflectance. The ground truth abundance maps of the dataset are displayed in Figure 6.6 and Figure 6.7 for the Data-1 and Data-2, respectively. Each abundance map is of size 256 × 175 pixels which satisfy the nonnegativity and sum-to-one constraint at every location in the respective scene data.

Table 6.1: Locations of endmembers in the multitemporal data.

Endmembers	**Coordinates in Data - 1**	**Coordinates in Data - 2**
Renyolds_tunnel	(84, 49)	(5, 11)
Green_slime	(160, 29)	(164, 175)
Cyanide_potassium	(191, 17)	(2, 175)
Plastic_grnhouse	(128, 158)	(17, 17)
Montmorillonite_benzen	(240, 9)	(13, 31)
Cyanide_zinc	(26, 158)	(9, 63)
Ammonium_chloride	(225, 110)	(39, 125)

The result analysis and the performance comparisons are carried out as follows. We begin at gross-level analysis which includes finding data reconstruction error (DRE) maps for the data cubes, verification of number of endmembers in the scene, and time complexities of different algorithms. This is followed by a detailed performance comparison to assess the accuracy of extracted endmembers and abundances at different noise levels in the data. Finally an additional test is carried out to further validate the estimated unmixed components. This is done by adding both low variance ($\sigma^2 = 0.01$) and high variance ($\sigma^2 = 0.1$) noises to the data. In addition to this, noise sensitivity analysis is also carried out on different approaches by considering various noise levels.

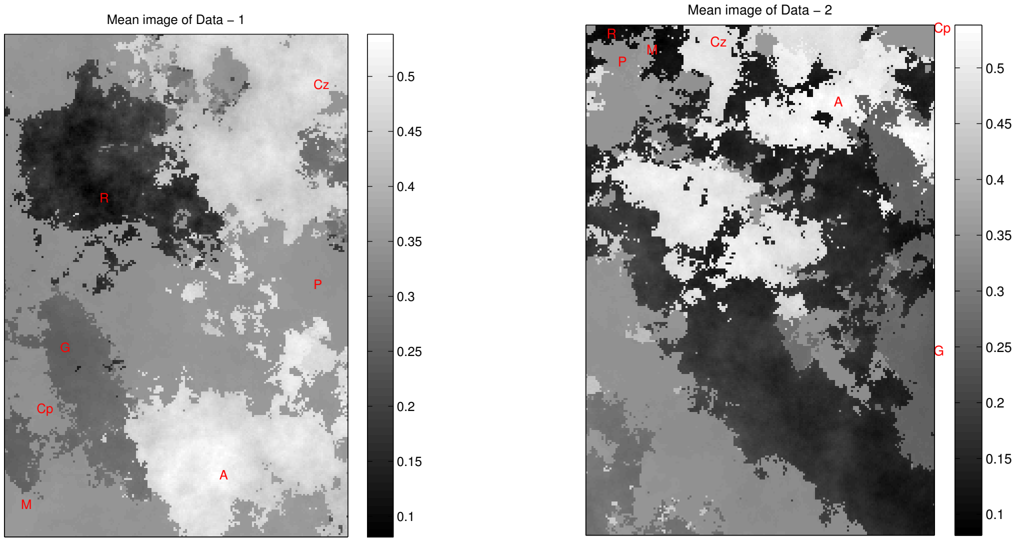

(a) (b)

Figure 6.4: Mean images of multitemporal data: mean image of (a) Data-1, and (b) Data-2. Here the mean is taken at each location across the spectral bands. The dataset has seven endmembers and their locations in the scenes are labeled as R: Renyolds_tunnel_sludge_sm93-15.29328, G: Green_slime_sm93-14a.28199, Cp: Cyanide_potassium_ferro.28065, P: Plastic_grnhouse_roof_gga-54.28462, M: Montmorillonite_benzen.28220, Cz: Cyanide_zinc_k_1.28013, and A: Ammonium_chloride_gds77.27373.

We begin by calculating data reconstruction error for both the data cubes using the unmixed components as obtained from the standard chains of complete spectral unmixing, i.e., VD [79]+VCA [102]+FCLS [122] and HySime [80]+MVC-NMF [111], and compare the same with the proposed approach. In order to do this, the RMSE [106] is calculated between the available and the reconstructed reflectance. Computing the RMSE at each pixel location gives us a DRE at that location. For an ith location it is given as

$$\mathrm{DRE}_i = \left\|\mathbf{R}_i - \widetilde{\mathbf{R}}_i\right\|^2, \forall\ i \in l_1 l_2, \tag{6.6}$$

where, $\mathbf{R}_i$ and $\widetilde{\mathbf{R}}_i$ denote true and reconstructed data vectors at the ith location. Therefore, $\{\mathrm{DRE}_i\}_{i=1}^{l_1 l_2}$ gives us a DRE map which has the same size as the image representing in a band. Figure 6.8 and 6.9 show the DRE maps for the Data-1 and the Data-2, respectively, considering a noise variance of $\sigma^2 = 0.1$ in the data. It can be observed from the figures that the DRE at each location as well as the average error and their standard deviation are drastically reduced using the proposed approach when compared

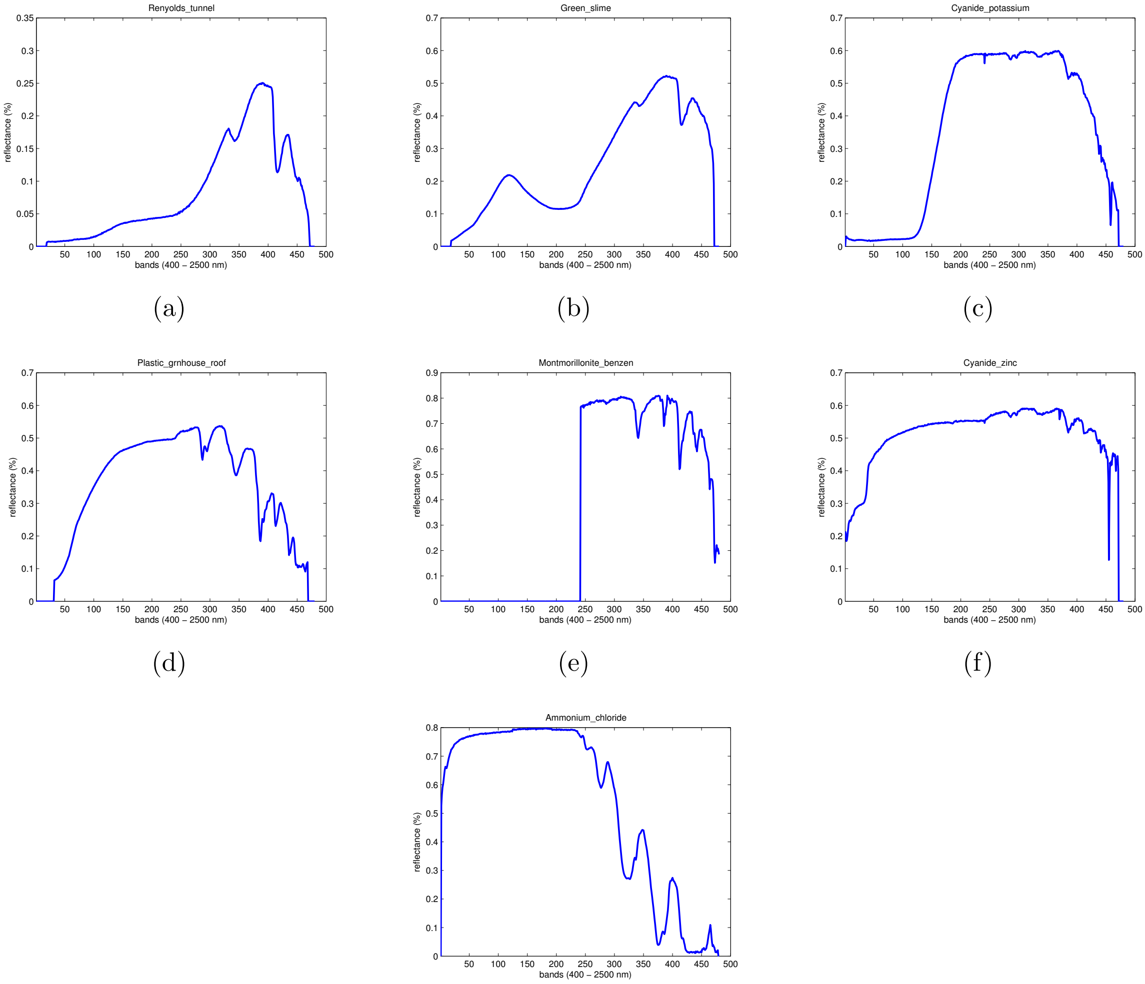

(a) (b) (c)

(d) (e) (f)

(g)

Figure 6.5: Plots showing the spectral bands versus ground truth endmembers reflectance: (a) Renyolds_tunnel_sludge_sm93-15.29328, (b) Green_slime_sm93-14a.28199, (c) Cyanide_potassium_ferro.28065, (d) Plastic_grnhouse_roof_gga-54.28462, (e) Montmorillonite_benzen.28220, (f) Cyanide_zinc_k_1.28013, and (g) Ammonium_chloride_gds77.27373.

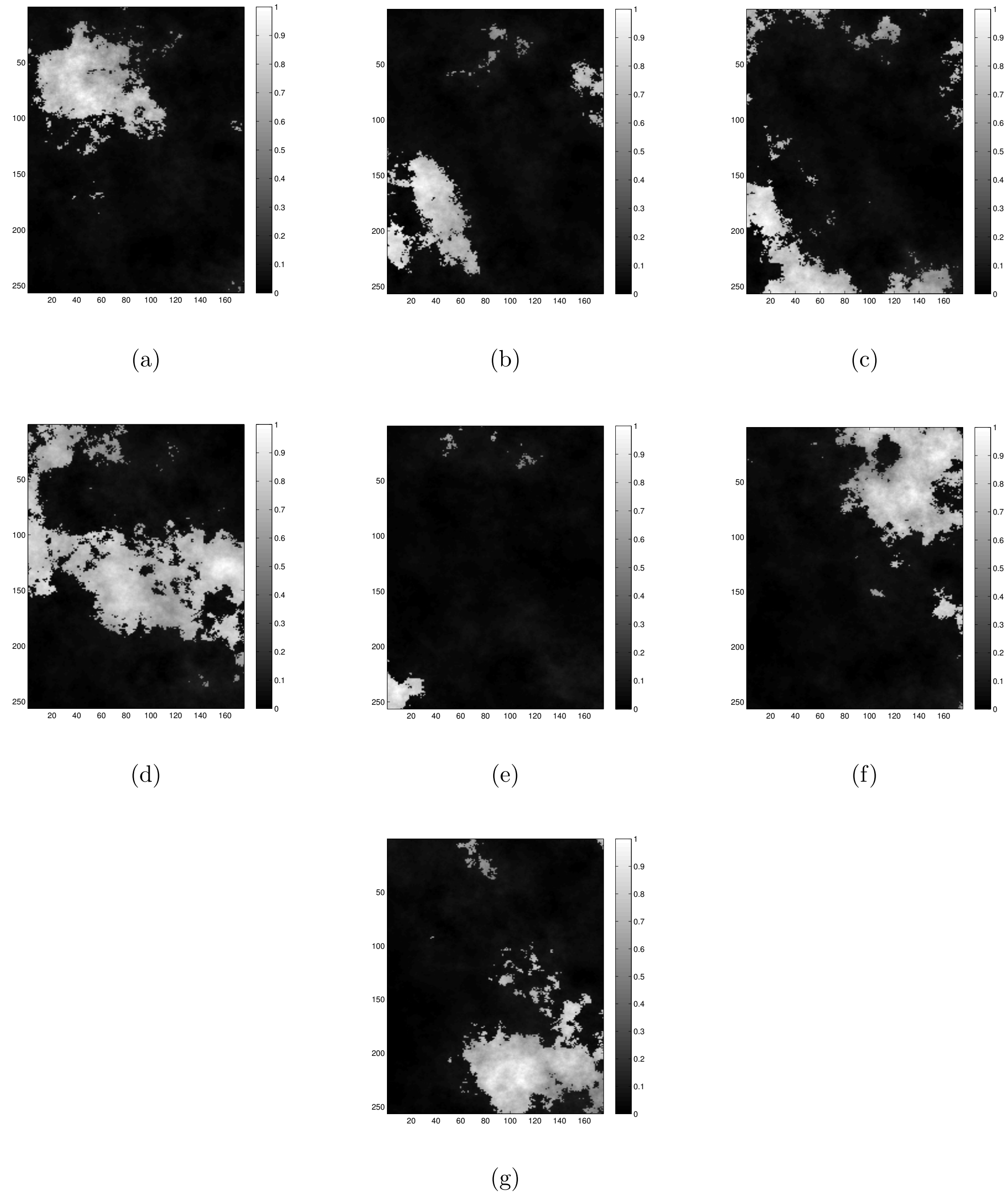

(a) (b) (c)

(d) (e) (f)

(g)

Figure 6.6: Ground truth abundances of Data-1. Abundance maps of (a) Renyolds_tunnel_sludge_sm93-15.29328, (b) Green_slime_sm93-14a.28199, (c) Cyanide_potassium_ferro.28065, (d) Plastic_grnhouse_roof_gga-54.28462, (e) Montmorillonite_benzen.28220, (f) Cyanide_zinc_k_1.28013, and (g) Ammonium_chloride_gds77.27373.

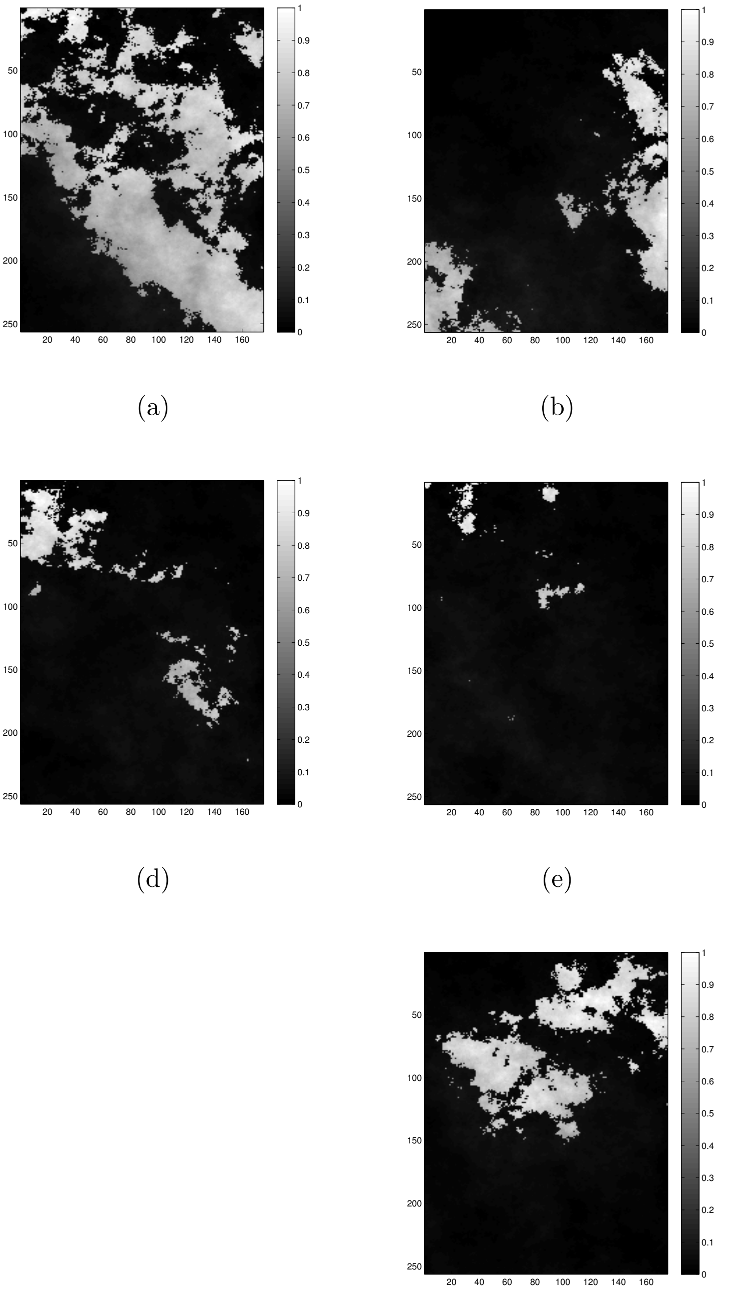

(a) (b) (c)

(d) (e) (f)

(g)

Figure 6.7: Ground truth abundances of Data-2. Abundance maps of (a) Renyolds_tunnel_sludge_sm93-15.29328, (b) Green_slime_sm93-14a.28199, (c) Cyanide_potassium_ferro.28065, (d) Plastic_grnhouse_roof_gga-54.28462, (e) Montmorillonite_benzen.28220, (f) Cyanide_zinc_k_1.28013, and (g) Ammonium_chloride_gds77.27373.

to the state-of-art approaches. Here the average errors and their standard deviations are computed from the respective DRE maps. This shows that our unified framework for complete spectral unmixing performs significantly better. These DRE calculations use the estimated number of endmembers in the scene which in our case is verified by carrying out a sensitivity analysis. The total error computed by using the DRE map is utilized as the feedback mechanism in our iterative bootstrapping approach.

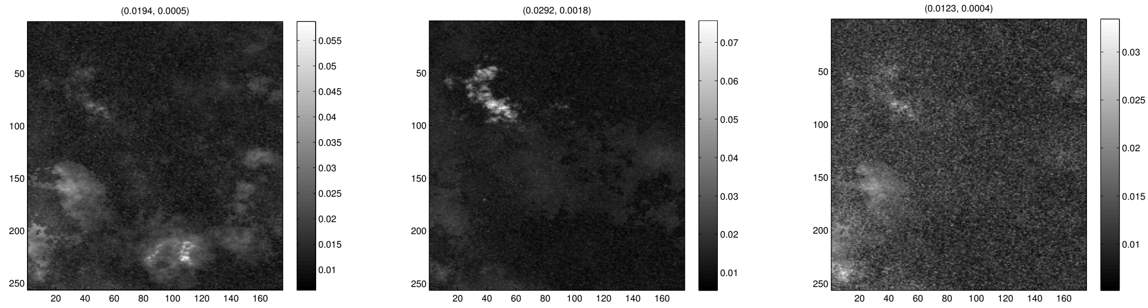

(a) (b) (c)

Figure 6.8: DRE maps for Data-1 at $\sigma^2 = 0.1$: (a) using VD [79]+VCA [102]+FCLS [122], (b) using HySime [80]+MVC-NMF [111], and (c) using the proposed IB approach. The average errors and standard deviations are mentioned on the top of each figure.

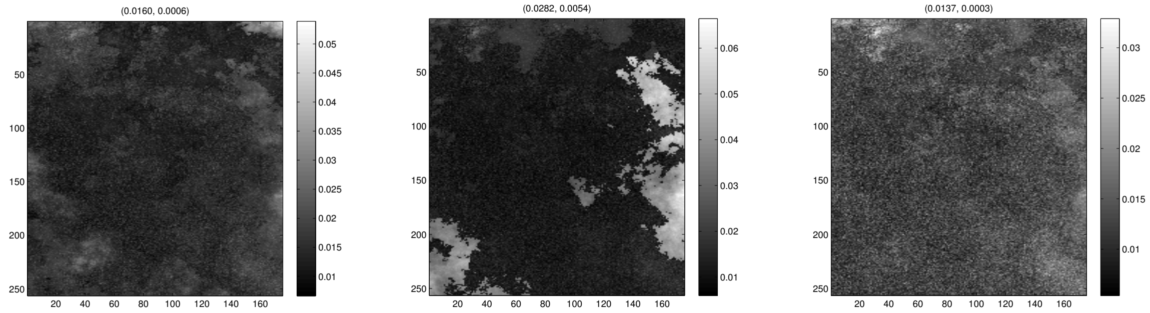

(a) (b) (c)

Figure 6.9: DRE maps for Data-2 at $\sigma^2 = 0.1$: (a) using VD [79]+VCA [102]+FCLS [122], (b) using HySime [80]+MVC-NMF [111], and (c) using the proposed IB approach. The average errors and standard deviations are mentioned on the top of each figure.

A crucial point in the spectral unmixing is to ensure the correct number of endmembers within the scene. Hence, to verify the performance of the proposed approach, we conducted the sensitivity analysis at different noise levels in the data and by increasing number of endmembers. This analysis tests the competence of our algorithm in obtaining accurate estimate of number of endmembers, i.e., $\hat{e}$. This is done by incrementing

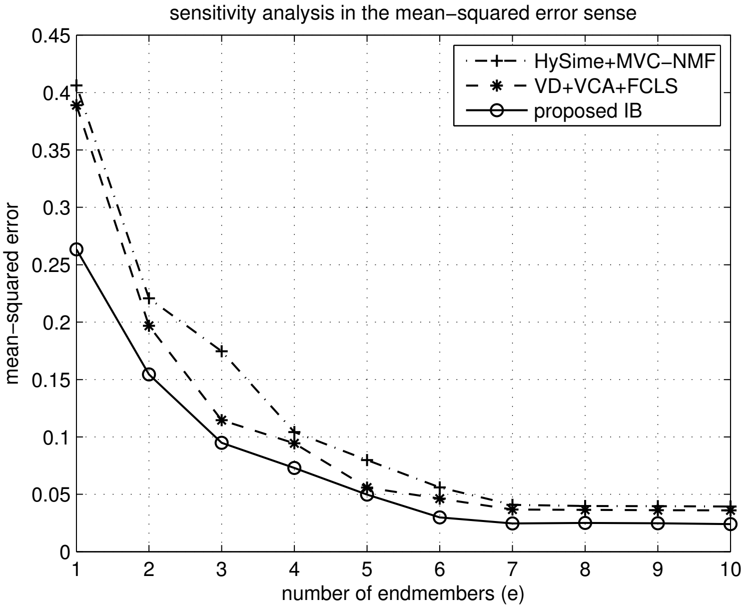

Figure 6.10: Sensitivity analysis for increasing number of endmembers at a noise level of $\sigma^2 = 0.1$: The plot showing the graph of number of endmembers versus average mean-squared error. Note that the errors for both the data cubes are combined and displayed in the same graph. A constant value of 0.0263 for $e \geq 7$ using the proposed approach indicates that there are seven endmembers in the dataset, that matches with the true value. The use of the state-of-art approaches also resulted in a similar trend though incur higher reconstruction error.

the number of endmembers e starting from a least number, i.e., 1, and measuring the mean-squared error between the true and reconstructed data using different approaches. In Figure 6.10 we display the plot of number of endmembers versus the average error for the two datasets at $\sigma^2 = 0.1$. Here the error is computed as mean of squared difference between the true and reconstructed data for each hyperspectral data cube and the two values are average out. It can be seen from the figure that for $e = 7$, the error has a minimum value of 0.0263 for the proposed method, and it remains constant there after indicating that there are seven spectrally distinct signatures present in the data. This number exactly matches with the ground truth validating the correctness of our approach in extracting the number of endmembers which is clearly evident from Figure 6.4. One may also observe that our approach has the least reconstruction error.

The execution time of an algorithm constitutes an important parameter in many of the remote sensing applications. Hence, the time complexity of the different algorithms are now compared in terms of the total processing time for the complete spectral unmixing. The individual execution times in the standard chains are added to compute their total time for complete unmixing. For the proposed IB approach time taken till the convergence represents the total time. In Table 6.2 we give the processing time expressed as the averages over processing times for Data-1 and Data-2 for different approaches. We observe that the time complexity of the proposed approach is almost similar to the approaches based on the standard chains. However, the advantage of the proposed approach lies in blind decomposition of the data with a greater accuracy using only the hyperspectral data captured at different times. The proposed unified framework can easily be implemented on a GPU based hardware using the data-partitioning strategies [165] in order to speed-up the computations.

Table 6.2: Processing Time for Complete Spectral Unmixing of the Data-1 and Data-2 Averaged over different noise levels. Algorithms are run on a Desktop PC with Intel® Core^{TM} i5-3210M CPU at 2.5 GHz with 4 GB of RAM.

Algorithms	Time (in minutes)
VD [79]+VCA [102]+FCLS [122]	5.0020
HySime [80]+MVC-NMF [111]	6.4780
proposed IB	6.9142

After completing the coarse level analysis, we now turn to more refined analysis of results in terms of accuracy in estimating individual unmixed components which include endmembers and abundances. In order to do the same we again consider data with different noise levels. We first compare the performance of various methods on endmember extraction followed by their abundance estimation which is done by comparing them with their ground truths. Figure 6.11 shows the plots of the spectral bands versus ground truth as well as estimated endmember values using different approaches by considering a noise variance of 0.1 in the data. From the plots shown, it is clear that the estimated endmembers differ from their true values. However, a close examination reveals two important distinctions between the estimated endmembers of the proposed and other approaches. Firstly, one may notice that the plots of ground truth and that of estimated by using the MVC-NMF approach differ significantly. This is clearly visible in Figure 6.11 (a) for an endmember plot of Renyolds_tunnel. Secondly, even though the result due to VCA closely follows the ground truth, the plots of proposed approach are almost overlaid on the ground truth, indicating that the proposed approach outperforms other methods in estimating the endmembers. This is due to the fact that the proposed approach restricts the solution space of the endmembers by making use of the same scene data captured at different times. This together with the better estimates of abundances by using bootstrapping results in better estimate of endmember values. Note that the results shown in Figure 6.11 are derived using the Data-1 for VCA as well as MVC-NMF, but, the proposed approach results are due to the usage of both Data-1 and Data-2. Similar results were obtained while using the Data-2 for the other methods which are not shown here.

Next we compare our results for the accuracy of estimated abundances. The abundance maps estimated using different approaches are shown in Figure 6.12 and 13 for the same noise variance of 0.1. Since the MVC-NMF approach uses the FCLS method to estimate the abundances, we display the same set of abundances for both these approaches for Data-1 in Figure 6.12 (a) to Figure 6.12 (g), and for Data-2 in Figure 6.13 (a) to Figure 6.13 (g). The abundances estimated using the proposed method are shown in Figure 6.12 (h) to Figure 6.12 (n), and Figure 6.13 (h) to Figure 6.13 (n) for the two datasets. The maps shown using our approach indicate that their spatial distribution is consistent and closer to the the respective ground truth abundance maps (see Figure 6.6 and Figure 6.7) when compared to the other approaches. This is because the proposed approach uses the MAP approach combined with IB that makes it to better handle the ill-posedness in the problem.

Our results on the endmember extraction and abundance estimation are now compared with the other approaches using different quantitative measures. For this the following quantitative measures: root mean squared error (RMSE) [106], spectral angle mapper (SAM) [107] and spectral information divergence (SID) [108] are used. The results on estimated number of endmembers $\hat{e}$ are compared with VD [79] and HySime [80] methods. The comparison of the proposed approach for estimated endmembers $\widehat{\mathbf{M}}$ are shown with the VCA [102] and MVC-NMF [111] approaches while FCLS [122] and MVC-NMF [111] approaches are used in comparing the results of abundance estimation $\widehat{\mathbf{A}}$. Errors are computed between the ground truths and the estimated values using the different approaches. Lower values for all the measures indicate better performance. We would like to mention here that the quantitative comparisons are carried out separately for each data cube at increasing noise levels. Due to limited space the comparison is shown for only two noise levels. For a noise variance of $\sigma^2 = 0.01$, these measures are

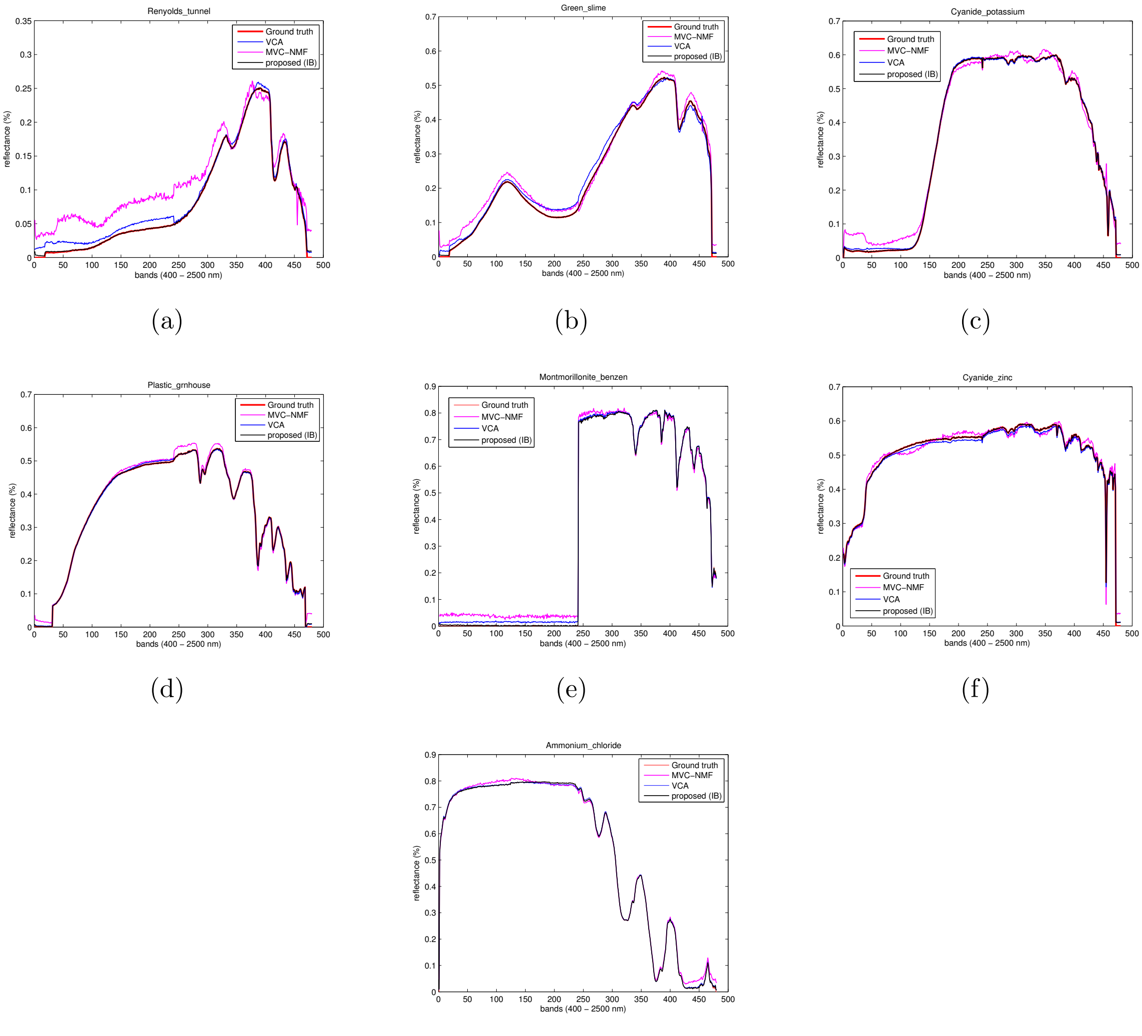

(a) (b) (c)

(d) (e) (f)

(g)

Figure 6.11: Plots showing spectral bands versus estimated endmember reflectance for Data-1 with the noise variance of $\sigma^2 = 0.1$. Estimated endmember signature of (a) Renyolds_tunnel_sludge_sm93-15.29328, (b) Green_slime_sm93-14a.28199, (c) Cyanide_potassium_ferro.28065, (d) Plastic_grnhouse_roof_gga-54.28462, (e) Montmorillonite_benzen.28220, (f) Cyanide_zinc_k_1.28013, and (g) Ammonium_chloride_gds77.27373. Note that the results are derived using the Data-1 for VCA as well as for MVC-NMF. The figure also has the plots of ground truth signatures for the comparison purpose. One can see that plots of the proposed method almost coincide with the corresponding ground truth plots.

tabulated in Tables 6.3 and 6.4 for Data-1 and Data-2, respectively. Similarly for a noise variance of $\sigma^2 = 0.1$, they are listed in Tables 6.5 and 6.6 for the two datasets. Observe that the quantitative measures in Tables 6.3 and 6.4 for endmembers $\widehat{\mathbf{M}}$ are the same for the proposed approach. This is because our approach uses both the datasets for estimating the endmembers. This is equally applicable to Tables 6.5 and 6.6 for the results on endmember extraction. Note that the scores are averaged over the pixel locations of

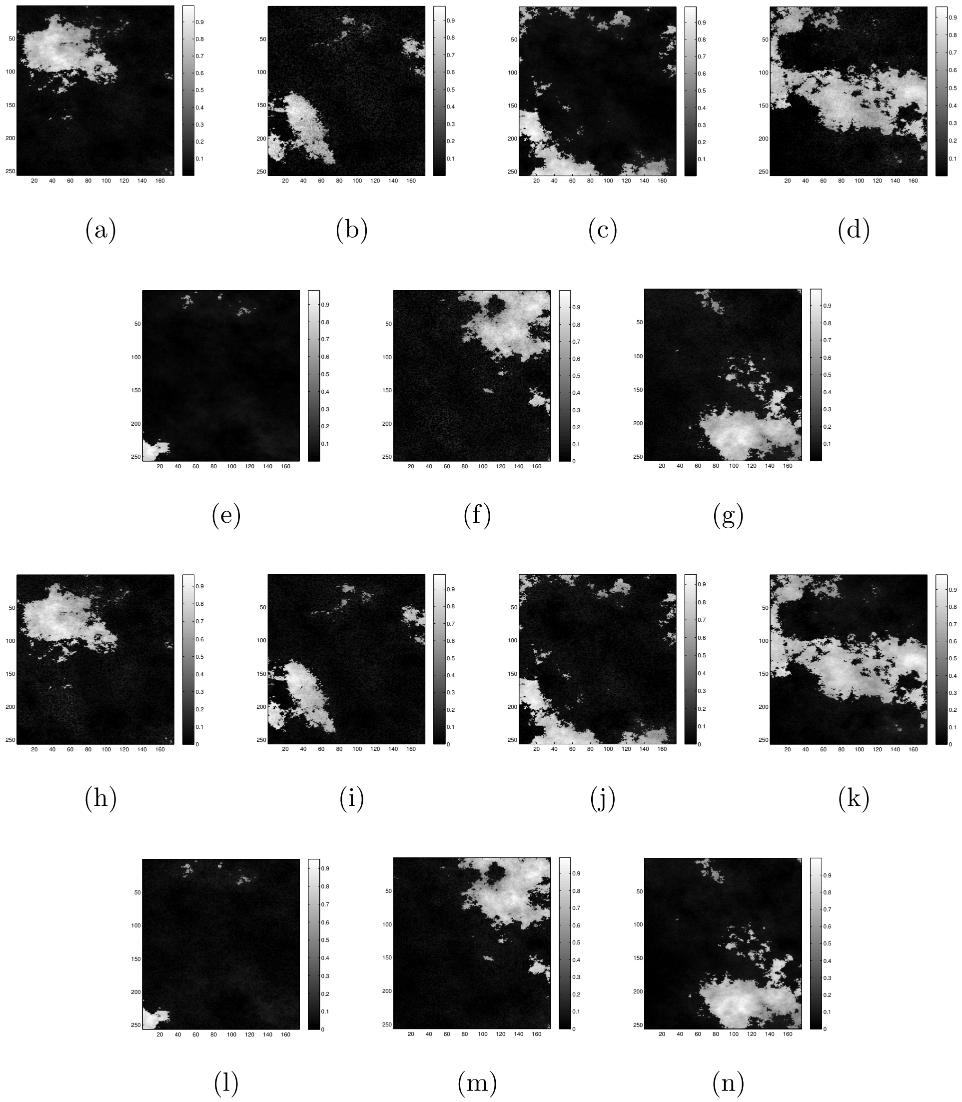
(a) (b) (c) (d)

(e) (f) (g)

(h) (i) (j) (k)

(l) (m) (n)

Figure 6.12: Abundance maps estimated using different approaches at a noise level of $\sigma^2 = 0.1$ in the Data-1: Abundance maps estimated using (a-g) FCLS [122]/MVC-NMF [111] approaches, and (h-n) proposed IB approach. These abundances correspond to the endmembers of Renyolds_tunnel_sludge_sm93-15.29328 (a,h), Green_slime_sm93-14a.28199 (b,i), Cyanide_potassium_ferro.28065 (c,j), Plastic_grnhouse_roof_gga-54.28462 (d,k), Montmorillonite_benzen.28220 (e,l), Cyanide_zinc_k_1.28013 (f,m), and Ammonium_chloride_gds77.27373 (g,n). Visual inspection of the maps indicate that the abundances estimated using the proposed approach are consistent and closer to the ground truth maps (see Figure 6.6) when compared to the other approaches.

the data, for the abundances corresponding to each endmember. For instance, for Renyolds_tunnel, the RMSE is calculated at each pixel location between its ground truth and the estimated abundances using different approaches, and the average value is obtained using these. From the tables one can see that the proposed approach improves the complete spectral unmixing of the data when compared to the other approaches. We see that

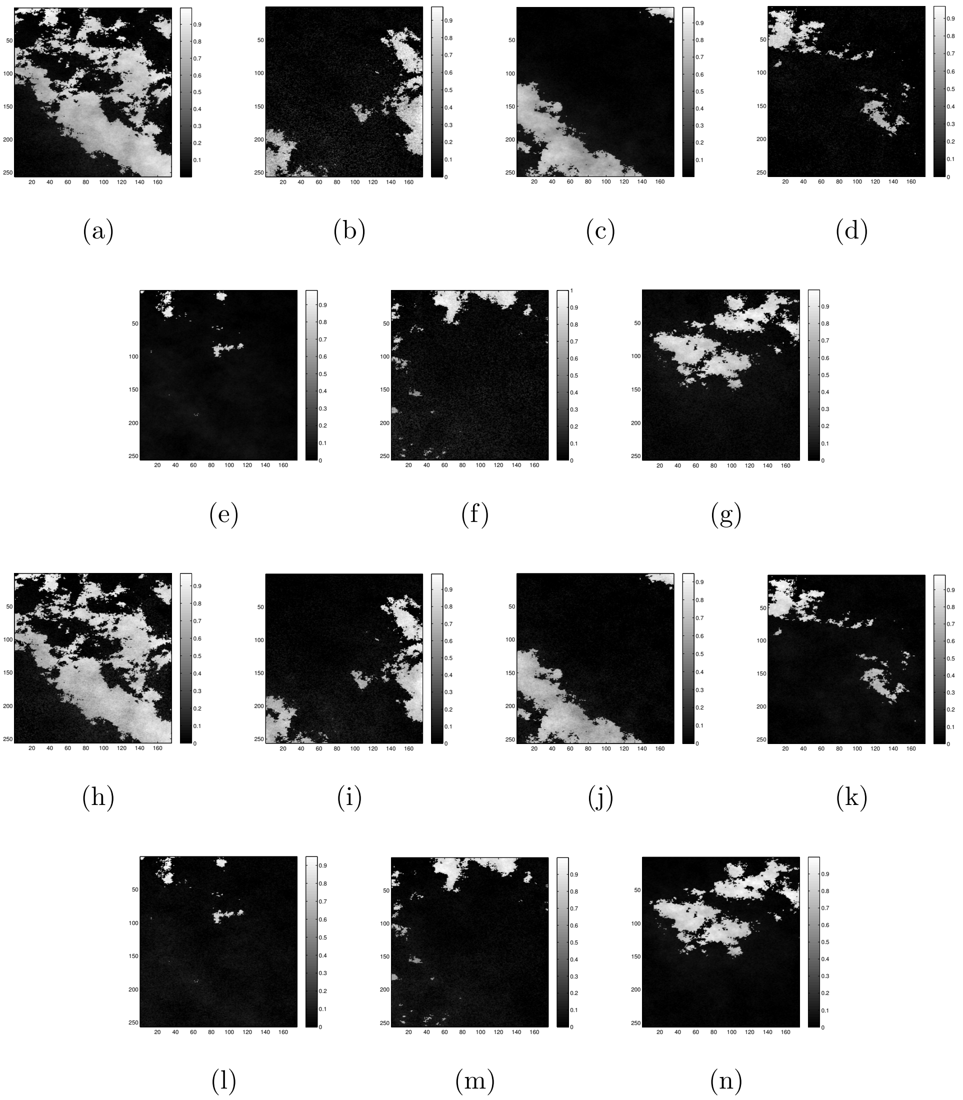

(a) (b) (c) (d)

(e) (f) (g)

(h) (i) (j) (k)

(l) (m) (n)

Figure 6.13: Abundance maps estimated using different approaches at a noise level of $\sigma^2 = 0.1$ in the Data-2: Abundance maps estimated using (a-g) FCLS [122]/MVC-NMF [111] approaches, and (h-n) proposed IB approach. These abundances correspond to the endmembers of Renyolds_tunnel_sludge_sm93-15.29328 (a,h), Green_slime_sm93-14a.28199 (b,i), Cyanide_potassium_ferro.28065 (c,j), Plastic_grnhouse_roof_gga-54.28462 (d,k), Montmorillonite_benzen.28220 (e,l), Cyanide_zinc_k_1.28013 (f,m), and Ammonium_chloride_gds77.27373 (g,n). Visual inspection of the maps indicate that the abundances estimated using the proposed approach are consistent and closer to the ground truth maps (see Figure 6.7) when compared to the other approaches.

the $\hat{e}$ is correct for all the approaches as shown in the tables. However the performances of the different approaches differ for endmembers and abundances estimation. As far as the endmember extraction is concerened, the proposed iterative approach outperforms the existing algorithms in terms of RMSE, SAM as well as SID. The errors in the abundance estimation are also greatly reduced due to the improved estimation of endmembers in our approach. The better $\widehat{\mathbf{M}}$ and $\widehat{\mathbf{A}}$ result in significant error reduction in RMSE as seen from the tables.

In our approach of endmember extraction, we use the entire dataset while the other approaches in the literature extract endmember matrix separately for each data cube. Hence, we now show the comparison when the entire dataset is used in these methods for extracting endmembers. We carry out an experiment wherein both the data cubes are combined and are used to estimate the endmembers in other approaches. Table 6.7 shows the comparison in terms of average error scores where the endmembers are estimated from a combined data, i.e., combining the Data-1 and Data-2. Our proposed algorithm better restricts the solution space by utilizing the temporal characteristics along with the spatial and spectral information.

Finally, an additional cross-check is done on the accuracy of estimated unmixed components. For this purpose, we compute relative power of the components which are orthogonal to the identified endmembers [80]. The calculations are carried out using the obtained value of $e = 7$. To do this, we evaluate $\left\|\widehat{\mathbf{M}}_{\underset{e}{\perp}}\tilde{\mathbf{r}}\right\|^2 / \|\tilde{\mathbf{r}}\|^2, \forall\tilde{\mathbf{r}}$, where, $\widehat{\mathbf{M}}_{\underset{e}{\perp}}$ has the columns orthogonal to the $\widehat{\mathbf{M}}$, and $\tilde{\mathbf{r}}$ is the reconstructed data vector from the entities estimated using different approaches. For a noise variance of $\sigma^2 = 0.1$ in Data-1, the relative power maps for VCA [102]+FCLS [122], MVC-NMF [111] and for the proposed approach are shown in Figure 6.14 (a), (b) and (c), respectively, and the same are displayed in Figure 6.15 for the Data-2. Since the power is computed at each pixel, the size of these maps are same as size of each band-image, i.e., 256 × 175 pixels. Since the relative powers in this case indicate incoherence between $\widehat{\mathbf{M}}$ and $\tilde{\mathbf{r}}$, we expect the resultant maps differ significantly from the scene data. It can be seen from the Figure 6.14 and Figure 6.15 that the maps do not show the scene details ensuring the correctness of the identified endmember matrices by our approach as well as by the other approaches.

6.6 Conclusions

We presented a novel algorithm for simultaneously solving for the three mixing components of a hyperspectral data. The number of endmembers is found by initializing it with a lower bound provided by the orthogonal decomposition of data covariance matrix, and increasing it until to satisfy the least-squared error criterion. The data reconstruction

Table 6.3: Quantitative measures for the estimated endmembers and abundances of Data-1 with an additive Gaussian noise $\sigma^2 = 0.01$.

Measure	Algorithm	$\#\hat{e}$	Endmembers $\widehat{\mathbf{M}}$							Abundances $\widehat{\mathbf{A}}$						
			Renyolds tunnel	Green slime	Cyanide potassium	Plastic grnhouse	Montmorillonite benzen	Cyanide zinc	Ammonium chloride	Renyolds tunnel	Green slime	Cyanide potassium	Plastic grnhouse	Montmorillonite benzen	Cyanide zinc	Ammonium chloride
RMSE [106]	VD+VCA+FCLS	7	0.0126	0.0173	0.0103	0.0097	0.0164	0.0075	0.0058	0.0275	0.0318	0.0183	0.0304	0.0186	0.0284	0.0117
	HySime+MVC-NMF	7	0.0975	0.0682	0.1002	0.0682	0.1205	0.0895	0.0751	0.2214	0.2436	0.1941	0.1857	0.1143	0.1729	0.1103
	proposed IB	7	0.0021	0.0005	0.0009	0.0006	0.0031	0.0004	0.0001	0.0045	0.0062	0.0026	0.0090	0.0084	0.0016	0.0052
SAM [107]	VD+VCA+FCLS	7	8.2315	3.2157	1.1215	1.1156	2.7634	1.0932	1.0072	7.3256	15.1345	6.9843	5.1943	10.2476	9.7436	4.8764
	HySime+MVC-NMF	7	10.1264	14.2945	9.3281	8.5234	13.1208	9.2134	8.1238	12.1265	19.3281	10.2124	9.0981	20.0214	12.3621	9.0091
	proposed IB	7	1.8214	0.1805	0.2165	0.8632	0.9214	0.3526	0.3271	3.6432	9.8462	2.9261	2.8364	6.0073	4.9562	1.3241
SID [108]	VD+VCA+FCLS	7	$5.3643e^{-05}$	$6.1121e^{-05}$	$4.1392e^{-05}$	$3.3815e^{-05}$	$5.1265e^{-05}$	$3.1414e^{-05}$	$2.1836e^{-05}$	$2.1386e^{-05}$	$1.3695e^{-05}$	$1.0832e^{-05}$	$3.1904e^{-06}$	$1.8324e^{-05}$	$1.1645e^{-05}$	$3.5478e^{-06}$
	HySime+MVC-NMF	7	0.1125	0.6537	0.5642	0.5438	0.2100	0.8921	0.0288	0.3436	0.7446	0.6865	0.0162	0.7390	0.5261	0.4256
	proposed IB	7	$2.1438e^{-07}$	$1.3398e^{-07}$	$1.5678e^{-07}$	$1.4382e^{-07}$	$2.5368e^{-07}$	$1.0028e^{-07}$	$1.0009e^{-07}$	$3.3748e^{-07}$	$2.1254e^{-07}$	$2.6821e^{-07}$	$3.5621e^{-07}$	$4.2536e^{-07}$	$5.8462e^{-07}$	$4.9461e^{-07}$

Table 6.4: Quantitative measures for the estimated endmembers and abundances of Data-2 with an additive Gaussian noise $\sigma^2 = 0.01$.

Measure	Algorithm	$\#\hat{e}$	Endmembers $\widehat{\mathbf{M}}$							Abundances $\widehat{\mathbf{A}}$						
			Renyolds tunnel	Green slime	Cyanide potassium	Plastic grnhouse	Montmorillonite benzen	Cyanide zinc	Ammonium chloride	Renyolds tunnel	Green slime	Cyanide potassium	Plastic grnhouse	Montmorillonite benzen	Cyanide zinc	Ammonium chloride
RMSE [106]	VD+VCA+FCLS	7	0.0146	0.0182	0.0067	0.0116	0.0136	0.0082	0.0037	0.0238	0.0261	0.0572	0.0258	0.0132	0.0164	0.0193
	HySime+MVC-NMF	7	0.1102	0.1024	0.0195	0.1049	0.1563	0.2072	0.1162	0.2374	0.2842	0.2104	0.2097	0.1256	0.1943	0.0938
	proposed IB	7	0.0021	0.0005	0.0009	0.0006	0.0031	0.0004	0.0001	0.0072	0.0085	0.0063	0.0054	0.0019	0.0097	0.0033
SAM [107]	VD+VCA+FCLS	7	9.2354	3.8932	2.0921	1.0094	2.2193	1.9872	1.0987	11.9832	11.0214	12.9543	3.1975	11.7654	5.9763	3.4532
	HySime+MVC-NMF	7	10.1243	12.9871	11.8721	10.2130	11.1092	9.9213	7.9821	12.1243	12.1817	15.2831	6.9832	11.9835	6.9873	5.8321
	proposed IB	7	1.8214	0.1805	0.2165	0.8632	0.9214	0.3526	0.3271	4.1263	10.9214	3.8253	3.2716	7.0342	3.1253	2.7629
SID [108]	VD+VCA+FCLS	7	$3.2840e^{-05}$	$3.2941e^{-05}$	$9.5637e^{-05}$	$8.4536e^{-05}$	$7.4672e^{-05}$	$5.2528e^{-05}$	$4.3829e^{-05}$	$7.4672e^{-05}$	$2.4759e^{-05}$	$1.4682e^{-05}$	$1.8446e^{-05}$	$4.3361e^{-05}$	$1.3648e^{-05}$	$1.9332e^{-05}$
	HySime+MVC-NMF	7	0.1276	0.5873	0.1103	0.1439	0.2376	0.7932	0.2641	0.6125	0.6921	0.8073	0.7024	0.0197	0.0487	0.1482
	proposed IB	7	$2.1438e^{-07}$	$1.3398e^{-07}$	$1.5678e^{-07}$	$1.4382e^{-07}$	$2.5368e^{-07}$	$1.0028e^{-07}$	$1.0009e^{-07}$	$2.4739e^{-07}$	$1.1238e^{-07}$	$1.3256e^{-07}$	$2.9362e^{-07}$	$3.9625e^{-07}$	$2.1745e^{-07}$	$2.1649e^{-07}$

$\#\hat{e}$ is the estimated number of endmembers while the $\widehat{\mathbf{M}}$ and $\widehat{\mathbf{A}}$ are the estimated endmember matrix and abundance maps, respectively. The scores are calculated between the ground truth and the estimated values using different approaches. The scores for $\widehat{\mathbf{A}}$ are averaged for each abundance map corresponding to an endmember. Note that the endmembers $\widehat{\mathbf{M}}$ in the Table 6.3 and 6.4 are the same for the proposed approach.

Table 6.5: Quantitative measures for the estimated endmembers and abundances of Data-1 with an additive Gaussian noise $\sigma^2 = 0.1$.

Measure	Algorithm	$\#\hat{e}$	Endmembers $\widehat{\mathbf{M}}$							Abundances $\widehat{\mathbf{A}}$						
			Renyolds tunnel	Green slime	Cyanide potassium	Plastic grnhouse	Montmorillonite benzen	Cyanide zinc	Ammonium chloride	Renyolds tunnel	Green slime	Cyanide potassium	Plastic grnhouse	Montmorillonite benzen	Cyanide zinc	Ammonium chloride
RMSE[106]	VD+VCA+FCLS	7	0.0240	0.0268	0.0136	0.0119	0.0285	0.0116	0.0118	0.0489	0.0681	0.0367	0.0510	0.0243	0.0548	0.0271
	HySime+MVC-NMF	7	0.1369	0.1420	0.1198	0.1036	0.2025	0.1008	0.1027	0.3521	0.3998	0.2691	0.2558	0.1396	0.2277	0.1398
	proposed IB	7	0.0118	0.0093	0.0097	0.0086	0.0162	0.0058	0.0071	0.0379	0.0586	0.0322	0.0474	0.0233	0.0496	0.0266
SAM[107]	VD+VCA+FCLS	7	11.9056	4.9679	1.8154	1.4414	3.1583	1.2269	1.0788	9.6981	16.2107	7.7490	6.3964	12.1564	10.2074	5.3147
	HySime+MVC-NMF	7	12.1520	17.3652	11.7698	10.6735	19.3384	10.9837	10.9365	15.3628	22.3698	11.3112	10.9217	24.3005	15.3818	10.1005
	proposed IB	7	5.9822	1.8220	1.3004	1.2745	1.8016	0.6345	0.6441	7.9055	14.0120	6.8797	6.2877	11.6940	9.2836	5.2959
SID[108]	VD+VCA+FCLS	7	$8.4627e^{-03}$	$9.4628e^{-03}$	$8.4672e^{-03}$	$8.6729e^{-03}$	$8.4681e^{-03}$	$3.1272e^{-03}$	$6.7738e^{-03}$	$2.6534e^{-03}$	2.4610	$1.1642e^{-03}$	$7.8904e^{-03}$	$2.5111e^{-03}$	$5.0610e^{-03}$	$2.4994e^{-03}$
	HySime+MVC-NMF	7	0.3376	0.9812	0.8314	0.7618	0.3256	0.9819	0.0360	0.3912	0.7684	0.9598	0.0226	0.9987	0.7314	0.8542
	proposed IB	7	$3.2612e^{-06}$	$2.1849e^{-06}$	$2.1749e^{-06}$	$2.3749e^{-06}$	$5.7873e^{-06}$	$2.7688e^{-06}$	$2{,}1945e^{-06}$	$4.8499e^{-06}$	$2.1648e^{-06}$	$1.2123e^{-06}$	$1.1889e^{-06}$	$5.2822e^{-06}$	$7.8532e^{-06}$	$3.6191e^{-06}$

Table 6.6: Quantitative measures for the estimated endmembers and abundances of Data-2 with an additive Gaussian noise $\sigma^2 = 0.1$.

Measure	Algorithm	$\#\hat{e}$	Endmembers $\widehat{\mathbf{M}}$							Abundances $\widehat{\mathbf{A}}$						
			Renyolds tunnel	Green slime	Cyanide potassium	Plastic grnhouse	Montmorillonite benzen	Cyanide zinc	Ammonium chloride	Renyolds tunnel	Green slime	Cyanide potassium	Plastic grnhouse	Montmorillonite benzen	Cyanide zinc	Ammonium chloride
RMSE [106]	VD+VCA+FCLS	7	0.0217	0.0260	0.0199	0.0131	0.0317	0.0195	0.0143	0.0478	0.0485	0.0759	0.0426	0.0273	0.0331	0.0276
	HySime+MVC-NMF	7	0.1259	0.1365	0.1029	0.1157	0.1935	0.2133	0.1358	0.2973	0.3167	0.2556	0.2362	0.1534	0.2067	0.1038
	proposed IB	7	0.0118	0.0093	0.0097	0.0086	0.0162	0.0058	0.0071	0.0393	0.0375	0.0593	0.0377	0.0229	0.0275	0.0193
SAM [107]	VD+VCA+FCLS	7	11.2949	4.7812	2.6525	1.5536	3.5313	2.1625	1.3243	13.0446	12.9937	15.5577	4.4938	13.2668	6.5595	4.8517
	HySime+MVC-NMF	7	13.3052	16.1258	12.1027	11.3036	13.2697	10.3521	9.0035	16.3518	15.1927	20.1356	8.8316	14.5369	8.9931	7.5620
	proposed IB	7	5.9822	1.8220	1.3004	1.2745	1.8016	0.6345	0.6441	10.5112	9.5263	12.1508	4.3820	11.5886	5.3355	3.3788
SID [108]	VD+VCA+FCLS	7	$5.4892e^{-03}$	$5.4782e^{-03}$	$9.6573e^{-03}$	$3.2850e^{-03}$	$3.2758e^{-03}$	$5.7927e^{-03}$	$3.5311e^{-03}$	$3.2729e^{-03}$	$5.8532e^{-03}$	$4.5749e^{-03}$	$1.8446e^{-03}$	$4.3361e^{-03}$	$2.4639e^{-03}$	$1.9332e^{-03}$
	HySime+MVC-NMF	7	0.2159	0.7860	0.1542	0.1986	0.3481	0.9567	0.5264	0.8936	0.9526	0.9916	0.8095	0.0236	0.0936	0.3652
	proposed IB	7	$3.2612e^{-06}$	$2.1849e^{-06}$	$2.1749e^{-06}$	$2.3749e^{-06}$	$5.7873e^{-06}$	$2.7688e^{-06}$	$2{,}1945e^{-06}$	$4.5839e^{-06}$	$4.3739e^{-06}$	$5.4829e^{-06}$	$4.3819e^{-06}$	$2.3222e^{-06}$	$3.4562e^{-06}$	$1.0929e^{-06}$

$\#\hat{e}$ is the estimated number of endmembers while the $\widehat{\mathbf{M}}$ and $\widehat{\mathbf{A}}$ are the estimated endmember matrix and abundance maps, respectively. The scores are calculated between the ground truth and the estimated values using different approaches. The scores for $\widehat{\mathbf{A}}$ are averaged for each abundance map corresponding to an endmember. Note that the endmembers $\widehat{\mathbf{M}}$ in the Table 6.5 and 6.6 are the same for the proposed approach.

Table 6.7: Average error scores for endmember extraction on the combined data with additive Gaussian noise $\sigma^2 = 0.1$.

Algorithm	Endmembers $\widehat{\mathbf{M}}$						
	Renyolds tunnel	Green slime	Cyanide potassium	Plastic grnhouse	Montmorillonite benzen	Cyanide zinc	Ammonium chloride
	RMSE [106]						
VCA [102]	0.9451	1.4144	1.5470	1.4013	1.4948	1.5328	1.8532
MVC-NMF [111]	1.8432	2.4324	2.4324	2.6553	3.4347	2.7058	2.5649
proposed	0.0118	0.0093	0.0097	0.0086	0.0162	0.0058	0.0071
	SAM [107]						
VCA [102]	7.1542	3.4387	3.3245	3.3591	3.4591	2.4325	2.4501
MVC-NMF [111]	9.3212	4.0324	5.5435	6.4545	5.3543	3.4513	3.3455
proposed	5.9822	1.8220	1.3004	1.2745	1.8016	0.6345	0.6441
	SID [108]						
VCA [102]	$3.1244e^{-05}$	$2.2324e^{-05}$	$2.3535e^{-05}$	$2.4561e^{-05}$	$5.2356e^{-05}$	$2.5951e^{-05}$	$2.3539e^{-05}$
MVC-NMF [111]	$4.2201e^{-03}$	$3.0942e^{-03}$	$4.2234e^{-03}$	$4.2234e^{-03}$	$6.3434e^{-03}$	$3.4532e^{-03}$	$4.3659e^{-03}$
proposed	$3.2612e^{-06}$	$2.1849e^{-06}$	$2.1749e^{-06}$	$2.3749e^{-06}$	$5.7873e^{-06}$	$2.7688e^{-06}$	$2.1945e^{-06}$

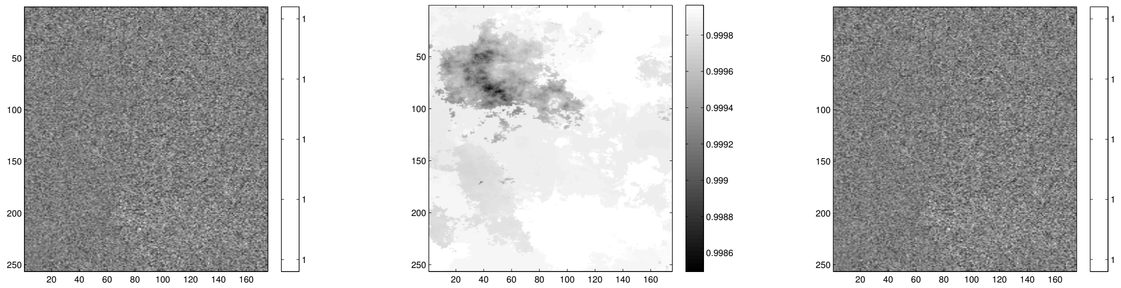

(a) (b) (c)

Figure 6.14: Relative power maps for Data-1 at $\sigma^2 = 0.1$ using (a) VCA [102]+FCLS [122], (b) MVC-NMF [111], and (c) proposed IB.

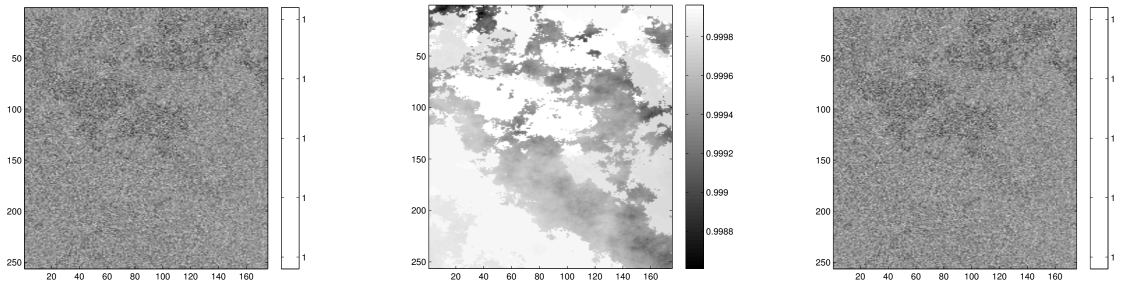

(a) (b) (c)

Figure 6.15: Relative power maps for Data-2 at $\sigma^2 = 0.1$ using (a) VCA [102]+FCLS [122], (b) MVC-NMF [111], and (c) proposed IB.

error is used in iterative bootstrapping framework resulting in optimal spectral unmixing of the given dataset. Simulation results conducted on synthetic dataset constructed using the real hyperspectral signatures and using different levels of additive white Gaussian noise in the dataset demonstrate the effectiveness of the proposed algorithm when compared to the standard processing chain incorporating the state-of-art approaches. The proposed methodology has an additional advantage of performing the spectral unmixing of multi-temporal data in a single chain of processing as well as serves as a basis for change detection in a hyperspectral scene based on the variations in the estimated abundances over a period of time. Future work involves further testing the proposed algorithm on real multitemporal hyperspectral datasets as well as implementing on the graphical processing unit (GPU) for real-time applications.

Chapter 7

Conclusions and Future Research

The spectral unmixing is the decomposition of the hyperspectral data into its constituents, i.e., number of endmembers, their signatures and corresponding abundances. In this thesis, we have proposed new approaches for abundance estimation, i.e., unmixing, endmember extraction and the complete spectral unmixing that includes estimation of all the three entities. We use a linear mixing model for representing the hyperspectral data. Our work introduced novel methodologies to perform the unmixing by considering the error in both the data and endmembers under the TLS-Tikhonov regularization framework. We next proposed an MAP-*d*HMRF approach in order to accurately estimate the abundances and to overcome the ill-posedness in the unmixing. We then presented a novel algorithm for band-wise endmember extraction which is fast and provides an accurate solution for endmembers. Finally, a unified methodology for the complete spectral unmixing is proposed. Here, we make use of our band-wise endmember extraction algorithm and the concept of bootstrapping. The theoretical analysis and the geometric illustrations are provided to show the effectiveness of the proposed approaches. The methods are validated by conducting experiments on the synthetic data as well as real data captured using satellite sensors. The unmixing approaches are tested on real AVIRIS Cuprite and AVIRIS Indian Pines data, and the complete spectral unmixing is tested on the synthetically generated data constructed using the real hyperspectral signatures available at the USGS spectral library. Our sensitivity analysis validates the performance of the proposed approaches under different parameter setting.

Following are the major observations drawn from this work.

1. Regularization framework is an effective way to perform the unmixing. In this case, suitable priors can be chosen to improve the solution when the data is noisy.

2. Knowing the endmembers, solving for the abundances is an ill-posed problem due to noise and outliers in the data, ill-conditioning of the endmember matrix and variations among the abundances. One may use the Bayesian framework in order to make the problem better-posed.

3. Random field based modeling of the abundances across the spectral range of the data gives greater flexibility to capture the underlying variations in the mixing proportions at each location of the scene, i.e., within an IFOV of the sensor. One of the approaches for estimating the model parameters can be of using an initial estimate from the data.

4. Endmembers can be effectively extracted using information present in the corresponding bands of the data. Integrating the temporal characteristics with the spatial and spectral information in the data increases the accuracy of the endmember extraction.

5. Additional information provided by the multi-temporal data can be used to simultaneously solve for identifying number of endmembers, their signatures and corresponding abundances. The bootstrapping mechanism with the positive feedback in terms of the data reconstruction error can be used to iteratively obtain the simultaneous solution in a single algorithm.

Future research lines

Although our work introduces many new approaches for hyperspectral data decomposition, one may consider the following future directions for further improvements.

- In our work, we have considered homogeneity and heterogeneity of abundances across the spectral space of the data. One can consider the same over the spatial locations as well. It would also be of interest to consider small regions in a scene for estimating the endmembers and abundances.

- Our work on the band-wise endmember extraction can be more generalized to account for variability in the endmembers as may happen over relatively long period of time.

- The proposed iterative bootstrapping algorithm can be further validated on real multi-temporal datasets acquired over a period of time across the same region.
- Most of the mixing models use the independent and identically distributed (IID) Gaussian noise. In practice, the noise may be dependent on many other factors such as atmospheric conditions, etc. Use of non-Gaussian noise may be of interest to be included while modeling the hyperspectral data.
- A better model represents the pixel intensities based on the flight parameters, sensor view, reflectance properties of the objects such as albedo can be considered in the image formation model to better characterize spectral properties of the materials.
- Generalize the proposed spectral unmixing approaches to include the possible nonlinearities in the mixing. Nonlinear mixing models with model parameter estimation by considering the non-Gaussian noise would also be of interest. It is a challenge to model the nonlinear mixing phenomenon, estimate their model parameters and obtain faster solutions.
- Many of the approaches used in the unmixing are iterative. A real-time implementation of the complete spectral unmixing would be useful in many of the applications. The hardware implementation of the proposed approaches is an interesting avenue, particularly on the graphical processing unit (GPU) which are used in the space applications.

Bibliography

[1] A. F. H. Goetz and et. al., “Imaging spectrometry for earth remote sensing,” *Science*, vol. 228, no. 4704, pp. 1147–1153, 1985.

[2] R. N. Clark, G. Swayze, K. Livo, P. F. Kokaly, S. J. Sutely, J. B. Dalton, R. R. McDougal, and C. A. Gent, “Imaging spectroscopy: Earth and planetary remote sensing with the usgs tetracorder and expert systems,” *Journal of Geophysical Research: Planets (1991-2012)*, vol. 108, no. E12, pp. 5–1 to 5–44, 2003.

[3] M. E. Schaepman, S. L. Ustin, A. Plaza, T. H. Painter, J. Verrelst, and S. Liang, “Earth system science related imaging spectroscopy - an assessment,” *Remote Sens. Environ.*, vol. 113, no. Supplement 1, pp. S123–S137, 2009. [Online]. Available: http://linkinghub.elsevier.com/retrieve/pii/S0034425709000819

[4] N. Keshava and J. Mustard, “Spectral unmixing,” *IEEE Siganl Processing Magazine*, vol. 19, no. 1, pp. 44 –57, Jan 2002.

[5] J. Bioucas-Dias and et al., “Hyperspectral unmixing overview: Geometrical, statistical, and sparse regression-based approaches,” *IEEE J. Sel. Topics Appl. Earth Observ.*, vol. 5, no. 2, pp. 354 –379, 2012.

[6] A. Villa, J. Chanussot, J. Benediktsson, and C. Jutten, “Spectal unmixing for the classification of hyperspectral images at a finer spatial resolution,” *IEEE J. Sel. Topics Signal Process.*, vol. 5, no. 3, pp. 521–533, 2011.

[7] I. Dopido, A. Villa, A. Plaza, and P. Gamba, “A quantitative and comparative assessment of unmixing-based feature extraction techniques for hyperspectral image classification,” *IEEE J. Sel. Topics Appl. Earth Observ.*, vol. 5, no. 2, pp. 421 –435, april 2012.

[8] Q. Du, L. Wasson, and R. King, “Unsupervised linear unmixing for change detection in multitemporal airborne hyperspectral imagery,” in *IGARSS*, pp. 136 - 140, 2005.

[9] G. Okin, “Relative spectral mixture analysis - a multitemporal index of total vegetation cover,” *Remote Sens. Environ.*, vol. 106, pp. 467–479, 2006.

[10] J. Meola and et al., “Detecting changes in hyperspectral imagery using a model-based approach,” *IEEE Trans. Geosci. Remote Sens.*, vol. 49, no. 7, pp. 2647–2661, 2011.

[11] M. A. Goenaga and et al., “Unmixing analysis of a time series of hyperion images over the guanica dry forest in puerto rico,” *IEEE J. Sel. Topics Appl. Earth Observ.*, vol. 6, no. 2, pp. 329–338, 2013.

[12] M. K. Arora and K. Tiwari, “Subpixel target enhancement in hyperspectral images,” *Defence Science Journal*, vol. 63, no. 1, pp. 63 – 68, 2013.

[13] A. J. Plaza, “Content-based hyperspectral image retrieval using spectral unmixing,” *Proc. SPIE 8180, Image and Signal Processing for Remote Sensing XVII, 81800O*, pp. 81 800O1–8, 2011.

[14] M. A. Veganzones and M. Grana, “A spectral/spatial cbir system for hyperspectral images,” *IEEE J. Sel. Topics Appl. Earth Observ.*, vol. 5, no. 2, pp. 488–500, 2012.

[15] G. P. Asner and D. B. Lobell, “A biogeophysical approach for automated swir unmixing of soils and vegetation,” *Remote Sens. Environ.*, vol. 74, pp. 99–112, 2000.

[16] C. Yang, J. H. Everitt, and Q. Du, “Applying linear spectral unmixing to airborne hyperspectral imagery for mapping yield variability in grain sorghum and cotton fields,” *SPIE Journal of Applied Remote Sensing*, vol. 4, p. 041887, 2010.

[17] F. Uhl, N. Oppelt, and I. Bartsch, “Spectral mixture of intertidal marine macroalgae around the island of helgoland (germany, north sea),” *Aquatic Botany*, vol. 111, pp. 112 – 124, 2013.

[18] N. Oppelt and W. Mauser, "Hyperspectral remote sensing for the monitoring of plant parameters of maize (zea mays)," *Proc. of SPIE, Remote Sensing for Agriculture, Ecosystems, and Hydrology IV*, vol. 4879, pp. 13 – 24, 2003.

[19] R. O. Green, M. L. Eastwood, C. M. Sarture, T. G. Chrien, M. Aronsson, B. J. Chippendale, J. A. Faust, B. E. Pavri, C. J. Chovit, M. Solis, and et al., "Imaging spectroscopy and the airborne visible infrared imaging spectrometer (aviris)," *Remote Sens. Environ.*, vol. 65, no. 3, no. 3, pp. 227–248, 1998.

[20] L. Rickard, R. Basedow, E. Zalewski, P. Silvergate, and M. Landers, "Hydice: An airborne system for hyperspectral imaging," *Proc. of SPIE*, vol. 1937, pp. 173–179, 1993.

[21] J. Pearlman, C. Segal, L. Liao, S. Carman, M. Folkman, B. Browne, L. Ong, and S. Ungar, "The hymap airborne hyperspectral sensor: The system, calibration and performance," in *Proc. of the 1st EARSEL Workshop on Imaging Spectroscopy*, 1998.

[22] Anon, "Design and development of airborne imaging spectrometer," SAC/EOSDG/AIS/09/93, Space Applications Centre, Ahmedabad, India., Tech. Rep., 1993.

[23] J. Levesque and K. Staenz, "A method for monitoring mine tailings revegation using hyperspectral remote sensing," in *Proc. of the IEEE International Geoscience and Remote Sensing Symposium*, vol. 1, 2004.

[24] S. Ungar, J. S. Pearlman, J. Mendenhall, and D. Reuter, "Overview of the earth observing one (eo-1) mission," *IEEE Trans. Geosci. Remote Sens.*, vol. 41, no. 6-1, pp. 1149–1159, 2003.

[25] M. J. Barnsley, J. J. Settle, M. A. Cutter, D. R. Lobb, and F. Teston, "The proba/chris mission: A low-cost smallsat for hyperspectral multiangle observations of the earth surface and atmosphere," *IEEE Trans. Geosci. Remote Sens.*, vol. 42, no. 7, pp. 1512–1520, 2004.

[26] A. S. K. Kumar and A. R. Chowdhury, "Hyper-spectral imager in visible and near-infrared band for lunar compositional mapping," *Journal of Earth System Science*, vol. 114, no. 6, pp. 721–724, 2005.

[27] [Online]. Available: http://spiedigitallibrary.org/

[28] G. Hughes, "On the mean accuracy of statistical pattern recognizers," *IEEE Trans. Inf. Theory*, vol. Vol. 14, No. 1, pp. 55–63, January 1968.

[29] [Online]. Available: http://personalpages.manschester.ac.uk/staff/d.h.foster/

[30] [Online]. Available: http://aviris.jpl.nasa.gov/data/free_data.html

[31] [Online]. Available: www.esa.int/Our_Activities/Observing_the_Earth/Proba-1/Going_hyperspectral

[32] [Online]. Available: www.isro.org/chandrayaan/htmls/ImageMoon.htm

[33] W.-K. Ma and et al., "A signal processing perspective on hyperspectral unmixing: Insights from remote sensing," *IEEE Signal Process. Mag.*, pp. 67–81, 2014.

[34] N. Dobigeon, J.-Y. Tourneret, C. Richard, J. Bermudez, S. Mclaughlin, and A. Hero, "Nonlinear unmixing of hyperspectral images," *IEEE Signal Process. Mag.*, vol. 31, no. 1, pp. 82 – 94, 2014.

[35] B. Hapke, "Bidirectional reflectance spectroscopy 1. theory," *Journal of Geophysical Research*, vol. Vol. 86, No. B4, pp. 3039–3054, April 10, 1981.

[36] G. Shaw and D. Manolakis, "Signal processing for hyperspectral image exploitation," *IEEE Signal Process. Mag.*, vol. 19, no. 1, pp. 12–16, 2002.

[37] J. Kerekes and J. Baum, "Hyperspectral imaging system modeling," *Lincoln Laboratory Journal*, vol. 14, no. 1, pp. 117–130, 2003.

[38] J. Boardman, "Analysis, understanding and visualization of hyperspectral data as convex sets in n-space," *Proc. SPIE*, vol. 2480, pp. 23–36, 1995.

[39] B.-C. Gao and et al., "Atmospheric correction algorithms for hyperspectral remote sensing data of land and ocean," *Remote Sens. Environ.*, vol. 113, pp. S17 – S24, 2009.

[40] A. P. Cracknell, "Synergy in remote sensing - what's in a pixel?" *Int. J. Remote Sens.*, vol. 19, no. 11, pp. 2025–2047, 1998.

[41] C. W. Groetsch, *Inverse Problems in the Mathematical Sciences.* Vieweg, 1993.

[42] M. Bertero and P. Bocacci, *Introduction to inverse problems in imaging.* IOS Press: Bristol and Philadelphia, 1997.

[43] C. R. Vogel, *Computational methods for inverse problems.* SIAM, 2002.

[44] M. Banham and A. Katsaggelos, "Digital image restoration," *IEEE Signal Process. Mag.*, vol. 14, no. 2, pp. 24 – 41, 1997.

[45] D. Kundur and D. Hatzinakos, "Blind image deconvolution," *IEEE Signal Process. Mag.*, vol. 13, no. 3, pp. 43 – 64, 1996.

[46] T. Moon, "The expectation-maximization algorithm," *IEEE Signal Process. Mag.*, vol. 13, no. 6, pp. 47 – 60, 1996.

[47] J. Hadamard, "Sur les problemes aux derivees partielles et leur signification physique," in *Princeton University Bulletin*, pp. 49-52, 1902.

[48] E. T. Jaynes, "The well-posed problem," *Foundations of Physics*, vol. 3, pp. 477 – 493, 1973.

[49] G. Strang, *Linear Algebra and its Applications.* Harcourt, Brace, Jovanovich, San Diego, 1988.

[50] R. Johnson and D. Wichern, *Applied Multivariate Statistical Analysis.* Prentice Hall, N.J., 4th ed., 1998.

[51] H. S. S. Andrew Gelman, John B Carlin and D. B. Rubin, *Bayesian Data Analysis.* Chapman & Hall/CRC, 2004.

[52] A. Papoulis and U. S. Pillai, *Probability, Random Variables and Stochastic Processes.* Tata McGraw-Hill, 2009.

[53] Q. Du and A. Plaza, "A tutorial on recent advances in spectral unmixing of hyperspectral data," in *IEEE International Geoscience and Remote Sensing Symposium (IGARSS)*, 2010.

[54] P. Common, "Independent component analysis: A new concept," *Signal Processing*, vol. 36, pp. 287 – 314, 1994.

[55] J. Bayliss, J. Gualtieri, and R. Cromp, "Analyzing hyperspectral data with independent component analysis," *Proc. SPIE*, vol. 3240, pp. 133–143, 1997.

[56] E. Moulines, J.-F. Cardoso, and E. Gassiat, "Maximum likelihood for blind separation and deconvolution of noisy signals using mixture models," in *Proc. of the IEEE International Conference on Acoustics, Speech, and Signal Processing*, vol. 5, pp. 3617-3620, 1997.

[57] H. Attias, "Independent factor analysis," *Neural Computation*, vol. 11, no. 4, pp. 803 – 851, 1999.

[58] A. Belouchrani, K. Abed-Meraim, J.-F. Cardoso, and E. Moulines, "A blind source separation technique using second-order statistics," *IEEE Trans. Signal Process.*, vol. 45, no. 2, pp. 434 – 444, 2002.

[59] C. Shah, M. K. Arora, and P. K. Varshney, "Ica mixture model for unsupervised classification of non-gaussian classes in multi/hyperspectral imagery," *Proc. of SPIE, Algorithms and Technologies for Multispectral, Hyperspectral, and Ultraspectral Imagery IX*, vol. 5093, pp. 569 – 580, 2003.

[60] J. Nascimento and J. Bioucas-Dias, "Does independent component analysis play a role in unmixing hyperspectral data?" *IEEE Trans. Geosci. Remote Sens.*, vol. 43, no. 1, pp. 175 – 187, 2005.

[61] ——, "Dependent component analysis: A hyperspectral unmixing algorithm," *Pattern Recognition and Image Analysis, Lecture Notes in Computer Science*, vol. 4478, pp. 612 – 619, 2007.

[62] R. B. Singer and T. B. McCord, "Mars: Large scale mixing of bright and dark surface materials and implications for analysis spectral reflectance," *in Proc. 10th Lunar Planatery Science Conference*, pp. 1835 – 1848, 1979.

[63] R. Heylen, M. Parente, and P. Gader, "A review of nonlinear hyperspectral unmixing methods," *IEEE J. Sel. Topics Appl. Earth Observ.*, vol. 7, no. 6, pp. 1844 – 1868, 2014.

[64] J. M. Nascimento and J. M. Bioucas-Dias, "Nonlinear mixture model for hyperspectral unmixing," *Proc. SPIE 7477, Image and Signal Processing for Remote Sensing XV, 7477OI*, pp. 7477OI1–8, 2009.

[65] N. Dobigeon, L. Tits, B. Somers, Y. Altmann, and P. Coppin, "A comparison of nonlinear mixing models for vegetated areas using simulated and real hyperspectral data," *IEEE Jouranl of Selected Topics in Applied Earth Observations and Remote Sensing*, vol. 7, no. 6, pp. 1869 – 1878, 2014.

[66] B. Somers, L. Tits, and P. Coppin, "Quntifying nonlinear spectral mixing in vegetated areas: Computer simulation model validation and first results," *IEEE Jouranl of Selected Topics in Applied Earth Observations and Remote Sensing*, vol. 7, no. 6, pp. 1956 – 1965, 2014.

[67] R. Heylen and P. Scheunders, "A distance geometric framework for nonlinear hyperspectral unmixing," *IEEE Jouranl of Selected Topics in Applied Earth Observations and Remote Sensing*, vol. 7, no. 6, pp. 1879 – 1888, 2014.

[68] P. Johnson, M. Smith, S. Taylor-George, and J. Adams, "A semiempirical method for analysis of the reflectance spectra of binary mineral mixtures," *Journal of Geophysical Research*, vol. 88, pp. 3557 – 3561, 1983.

[69] M. O. J. P. E. Adams, J. B.; Smith, "Spectral mixture modeling - a new analysis of rock and soil types at the viking lander 1 site," *Journal of Geophysical Research*, vol. vol. 91, pp. pp. 8098–8112, 1986.

[70] A. D. Stocker and A. P. Schaum, "Application of stochastic mixing models to hyperspectral detection problems," *Proc. SPIE*, vol. 3071, pp. 47–60, 1997.

[71] M. T. Eismann and R. C. Hardie, "Initialization and convergence of the stochastic mixing model," *Proc. SPIE, Imaging Spectrometry IX*, vol. 5159, pp. 307–318, 2003.

[72] C.-I. Chang, Ed., *Hyperspectral Data Exploitation: Theory and Applications.* Wiley-Interscience, John Wiley & Sons, pp. 107-148, 2007.

[73] N. Keshava, J. Kerekes, D. Manolakis, and et al., "Algorithm taxonomy for hyperspectral unmixing," *Proc. of SPIE*, vol. 4049, pp. 42 – 63, 2000.

[74] N. Keshava, “A survey of spectral unmixing algorithms,” *Lincoln Laboratory Journal*, vol. 14, no. 1, pp. 55–78, 2003.

[75] ——, “Distance metrics and band selection in hyperspectral processing with applications to material identification and spectral libraries,” *IEEE Trans. Geosci. Remote Sens.*, vol. 42, no. 7, pp. 1552–1565, 2004.

[76] H. Van Trees, *Optimum Array Processing: Part IV of Detection, Estimation, and Modulation Theory.* Hoboken, NJ: John Wiley & Sons, Inc., 2002.

[77] C.-I. Chang, *Hyperspectra Data Processing Algorithm Design and Analysis.* Willey-Blackwell, 2013.

[78] P. K. Varshney and M. K. Arora, *Advanced Image Processing Techniques for Remotely Sensed Hyperspectral Data.* Springer, 2004.

[79] C.-I. Chang and Q. Du, “Estimation of number of spectrally distinct signal sources in hyperspectral imagery,” *IEEE Trans. Geosci. Remote Sens.*, vol. 42, no. 3, pp. 608–619, 2004.

[80] J. M. Bioucas-Dias and J. M. P. Nascimento, “Hyperspectral subspace identification,” *IEEE Trans. Geosci. Remote Sens.*, vol. 46, no. 8, pp. 2435–2445, 2008.

[81] C.-I. Chang, W. Xiong, W. Liu, M.-L. Chang, C.-C. Wu, and C. C.-C. Chen, “Linear spectral mixture analysis based approaches to estimation of virtual dimensionality in hyperspectral imagery,” *IEEE Trans. Geosci. Remote Sens.*, vol. 48, no. 11, pp. 3960–3979, 2010.

[82] C.-I. Chang and et al., “Maximum orthogonal subspace projection approach to estimating the number of spectral signal sources in hyperspectral imagery,” *IEEE J. Sel. Topics Signal Process.*, vol. 5, no. 3, pp. 504–520, 2011.

[83] A. Ambikapathi and et al., “Hyperspectral data geometry-based estimation of number of endmembers using p-norm-based pure pixel identification algorithm,” *IEEE Trans. Geosci. Remote Sens.*, vol. 51, no. 5, pp. 2753 – 2769, 2013.

[84] X. Fu, W.-K. Ma, T.-H. Chan, and J. Bioucas-Dias, “Self-dictionary sparse regression for hyperspectral unmixing: Greedy pursuit and pure pixel search are related,” pp. 1–27, arXiv: 1409.4320v1, 2014.

[85] [Online]. Available: http://speclab.cr.usgs.gov/spectral-lib.html

[86] A. Plaza, G. Mart, J. Plaza, M. Zortea, and S. Sergio, “Recent developments in endmember extraction and spectral unmixing,” *Optical Remote Sensing Advances in Signal Processing and Exploitation Techniques*, pp. 1–33, 2010.

[87] A. Plaza, J. A. Benediktsson, J. W. Boardman, J. Brazile, L. Bruzzone, G. Camps-Valls, J. Chanussot, M. Fauvel, P. Gamba, A. Gualtieri, and et al., “Recent advances in techniques for hyperspectral image processing,” *Remote Sens. Environ.*, vol. 113, no. Supplement 1, pp. S110–S122, 2009.

[88] M. A. Veganzones and M. Grana, “Endmember extraction methods: A short review,” *Lecture Notes in Artificial Intelligence*, vol. 5179, Part III, pp. 400–407, 2008.

[89] Q. Du, N. Raksuntorn, N. Younan, and R. King, “End-member extraction for hyperspectral image analysis,” *Applied Optics*, vol. 47, no. 28, pp. F77–F84, 2008.

[90] U. Araujo, B. Saldanha, R. Galvao, T. Yoneyama, H. Chame, and V. Visani, “The successive projections algorithm for variable selection in spectroscopic multicomponent analysis,” *Chemometrics and Intelligent Laboratory Systems*, vol. 57, no. 2, pp. 65 – 73, 2001.

[91] H. Ren and C.-I. Chang, “Automatic spectral target recognition in hyperspectral imagery,” *IEEE Transactions on Aerospace and Electronic Systems*, vol. 39, no. 4, pp. 1232 – 1249, oct. 2003.

[92] J. Boardman, “Automating spectral unmixing of aviris data using convex geometry concepts,” *in Summaries of 4th annual JPL Airborne Geoscience Workshop*, vol. 1, pp. 11–14, 1993.

[93] C.-I. Chang and A. Plaza, “A fast iterative algorithm for implementation of pixel purity index,” *IEEE Geosci. Remote Sens. Lett.*, vol. 3, pp. 63 – 67, 2006.

[94] C.-I. Chang, C.-C. Wu, and H.-M. Chen, “Random pixel purity index,” *IEEE Geosci. Remote Sens. Lett.*, vol. 7, no. 2, pp. 324 –328, april 2010.

[95] M. D. Craig, “Minimum-volume transforms for remotely sensed data,” *IEEE Trans. Geosci. Remote Sens.*, vol. 32, no. 3, pp. 542 – 552, 1994.

[96] J. Harsanyi and C.-I. Chang, “Hyperspectral image classification and dimensionality reduction: an orthogonal subspace projection approach,” *IEEE Trans. Geosci. Remote Sens.*, vol. 32, no. 4, pp. 779 –785, 1994.

[97] C.-I. Chang, “Orthogonal subspace projection (osp) revisited: a comprehensive study and analysis,” *Geoscience and Remote Sensing, IEEE Transactions on*, vol. 43, no. 3, pp. 502 – 518, march 2005.

[98] M. E. Winter, “N-findr: an algorithm for fast autonomous spectral end-member determination in hyperspectral data,” in *Proc. SPIE, vol. 3753, pp. 266-277*, 1999.

[99] M. Berman, H. Kiiveri, R. Lagerstrom, A. Ernst, R. Dunne, and J. Huntington, “Ice: A statistical approach to identifying endmembers in hyperspectral images,” *IEEE Trans. Geosci. Remote Sens.*, vol. 42, no. 10, pp. 2085–2095, 2004.

[100] G. H. Golub and C. Van Loan, *Matrix Computations.* JHU Press, 1996.

[101] C.-C. Wu, S. Chu, and C.-I. Chang, “Sequential n-findr algorithms,” *Proc. SPIE*, vol. 7086, p. 70860C, 2008.

[102] J. Nascimento and J. Dias, “Vertex component analysis: a fast algorithm to unmix hyperspectral data,” *IEEE Trans. Geosci. Remote Sens.*, vol. 43, no. 4, pp. 898 – 910, 2005.

[103] A. Plaza and et al., “Spatial/spectral endmember extraction by multidimensional morphological operations,” *IEEE Trans. Geosci. Remote Sens.*, vol. 40, no. 9, pp. 2025–2041, 2002.

[104] D. Rogge and et al., “Integration of spatial-spectral information for the improved extraction of endmembers,” *Remote Sens. Environ.*, vol. 110, no. 3, pp. 287–303, 2007.

[105] M. Zortea and A. Plaza, “Spatial preprocessing for endmember extraction,” *IEEE Trans. Geosci. Remote Sens.*, vol. 47, pp. 2679–2693, 2009.

[106] Z. Wang and A. C. Bovik, “Mean squared error: Love it or leave it? a new look at signal fidelity measures,” *IEEE Signal Process. Mag.*, vol. 26, pp. 98–117, 2009.

[107] R. Yuhans, A. Goetz, and J. Boardman, “Discrmination among semi-arid landscape endmembers using the spectral angle mapper (sam) algorithm,” in *Proc. Summaries 3rd Annu. JPL Airborne Geoscience Workshop, R.O. Green, Ed.*, vol. 1, 1992, pp. 147–149.

[108] C.-I. Chang, “An information-theoretic approach to spectral variability, similarity, and discrimination for hyperspectral image analysis,” *IEEE Trans. Inf. Theory*, vol. 46, no. 5, pp. 1927 –1932, 2000.

[109] J. Plaza and et al., “On endmember identification in hyperspectral images without pure pixels: A comparison of algorithms,” *J. Math. Imaging Vis.*, vol. 42, no. 2-3, pp. 163–175, 2012.

[110] L. Parra, P. Sajda, and D. S., “Recovery of constituent spectra using non-negative matrix factorization,” *Proc. SPIE*, vol. 5207, no. 1, pp. 321 – 331, 2003.

[111] L. Miao and H. Qi, “Endmember extraction from highly mixed data using minimum volume constrained nonnegative matrix factorization,” *IEEE Trans. Geosci. Remote Sens.*, vol. 45, no. 3, pp. 765–777, 2007.

[112] T.-H. Chan and et al., “A convex analysis based minimum-volume enclosing simplex algorithm for hyperspectral unmixing,” *IEEE Trans. Signal Process.*, vol. 57, no. 11, pp. 4418 – 4432, 2009.

[113] T.-H. Chan, A. A. Ma, Wing-Kin, and Chi, “A simplex volume maximization framework for hyperspectral endmember extraction,” *IEEE Trans. Geosci. Remote Sens.*, vol. 49, no. 11, pp. 4177 – 4193, 2011.

[114] N. Gillis and S. A. Vavasis, “Fast and robust recursive algorithms for separable nonnegative matrix factorization,” *IEEE Transactions on Pattern Analysis and Machine Intelligence*, vol. 36, no. 4, pp. 698 – 714, 2014.

[115] A. Zare and P. Gader, "Endmember detection using the dirichlet process," in *19th International Conference on Pattern Recognition, ICPR*, 2008, pp. 1 –4.

[116] M. Smith, P. Johnson, and J. Adams, "Quantitative determination of mineral types and abundances from reflectance spectral using principal component analysis," *Journal of Geophysical Research*, vol. 90, no. B2, pp. C797 – C804, 1985.

[117] C.-I. Chang, *Hyperspectral imaging: Techniques for Spectral Detection and Classification.* New York: Kluwer Academic/Plenum Publishers, 2003.

[118] C. Kwan, B. Ayhan, G. Chen, J. Wang, B. Ji, and C.-I. Chang, "A novel approach for spectral unmixing, classification, and concentration estimation of chemical and biological agents," *IEEE Trans. Geosci. Remote Sens.*, vol. 44, no. 2, pp. 409 – 419, feb. 2006.

[119] L. Parra, K.-R. Mueller, C. Spence, A. Ziehe, and P. Sajda, "Unmixing hyperspectral data," *Proc. Advanced Neural Information Processes Systems (NIPS)*, vol. 12, pp. 942–948, 2000.

[120] J. Settle and N. Drake, "Linear mixing and the estimation of ground cover proportions," *Int. J. Remote Sens.*, vol. 14, no. 6, pp. 1159 – 1177, 1993.

[121] A. Barducci and A. Mecocci, "Theoritical and experimental assessment of noise effects on least-squares spectral unmixing of hyperspectral images," *Optical Engineering*, vol. 44, pp. 100–108, 2005.

[122] D. Heinz and C.-I. Chang, "Fully constrained least squares linear spectral mixture analysis method for material quantification in hyperspectral imagery," *IEEE Trans. Geosci. Remote Sens.*, vol. 39, no. 3, pp. 529 –545, 2001.

[123] R. Heylen, D. Burazerovic, and P. Scheunders, "Fully constrained least squares spectral unmixing by simplex projection," *IEEE Trans. Geosci. Remote Sens.*, vol. 49, no. 11, pp. 4112 –4122, 2011.

[124] S. Chettri and N. S. Netanyahu, "Spectral unmixing of remotely sensed imagery using maximum entropy," in *Proc. SPIE*, 1997.

[125] L. Miao, H. Qi, and H. Szu, “Unsupervised decomposition of mixed pixels using the maximum entropy principle,” in *18th International Conference on Pattern Recognition*, vol. 1, 2006, pp. 1067 –1070.

[126] ——, “A maximum entropy approach to unsupervised mixed-pixel decomposition,” *IEEE Trans. Image Process.*, vol. 16, no. 4, pp. 1008 –1021, 2007.

[127] M. Arngren, M. Schmidt, and J. Larsen, “Unmixing of hyperspectral images using bayesian nonnegative matrix factorization with volume prior,” *Journal of Signal Processing Systems*, vol. 65, no. 3, pp. 479–496, 2011.

[128] A. C. Bateson, G. P. Asner, and C. A. Wessman, “Endmember bundles: A new approach to incorporating endmember variability into spectral mixture analysis,” *IEEE Trans. Geosci. Remote Sens.*, vol. 38, no. 2, pp. 1083–1094, 2000.

[129] Y. Hu, H. Lee, and F. Scarpace, “Optimal linear spectral unmixing,” *IEEE Trans. Geosci. Remote Sens.*, vol. 37, pp. 639–644, 1999.

[130] B. Sirkeci, D. Brady, and J. Burman, “Restricted total least squares solutions for hyperspectral imagery,” in *IEEE International Conference on Acoustics, Speech, and Signal Processing, ICASSP ’00 Proc.*, vol. 1, 2000, pp. 624 –627.

[131] J. S. Bhatt, M. V. Joshi, and M. S. Raval, “A regularization based method for spectral unmixing of imaging spectrometer data,” *Proc. SPIE*, vol. 8537, pp. 85 370J1–7, 2012.

[132] J. Kent and K. Mardia, “Spatial classification using fuzzy membership models,” *IEEE Transactions on Pattern Analysis and Machine Intelligence*, vol. 10, no. 5, pp. 659 –671, 1988.

[133] R. Rand and D. Keenan, “A spectral mixture process conditioned by gibbs-based partitioning,” *IEEE Trans. Geosci. Remote Sens.*, vol. 39, no. 7, pp. 1421 –1434, 2001.

[134] O. Eches, N. Dobigeon, and J.-Y. Tourneret, “Enhancing hyperspectral image unmixing with spatial correlations,” *IEEE Trans. Geosci. Remote Sens.*, vol. 49, no. 11, pp. 4239 –4247, 2011.

[135] J. S. Bhatt, M. V. Joshi, and M. S. Raval, “A parametric statistical model over spectral space for the unmixing of imaging spectrometer data,” *Proc. SPIE*, vol. 8537, pp. 85 371J1–7, 2012.

[136] A. Ranganathan, “The dirichlet process mixture (dpm) model,” MIT, Tech. Rep., 2006.

[137] T. P. Minka, “Estimating a dirichlet distribution,” M.I.T., Tech. Rep., 2000, revised 2003, 2009.

[138] J. M. Bioucas-Dias and J. Nascimento, “Hyperspectral unmixing based on mixtures of dirichlet components,” *IEEE Trans. Geosci. Remote Sens.*, vol. 50, no. 3, pp. 863–878, 2012.

[139] M.-D. Iordache, L. Tits, J. Bioucas-Dias, A. Plaza, and B. Somers, “A dynamic unmixing framework for plant production system monitoring,” *IEEE J. Sel. Topics Appl. Earth Observ.*, vol. 7, no. 6, pp. 2016 – 2034, 2014.

[140] J. Plaza, A. Plaza, R. Perez, and P. Martinez, “On the use of small training sets for neural network-based characterization of mixed pixels in remotely sensed hyperspectral images,” *Pattern Recognition*, vol. 42, pp. 3032 – 3045, 2009.

[141] G. Licciardi and F. Del Frate, “Pixel unmixing in hyperspectral data by means of neural networks,” *IEEE Trans. Geosci. Remote Sens.*, vol. 49, no. 11, pp. 4163–4172, 2011.

[142] H. M. Mei, S., Z. Wang, and D. D. Feng, “Unsupervised spectral mixture analysis of highly mixed data with hopfield neural network,” *IEEE Jouranl of Selected Topics in Applied Earth Observations and Remote Sensing*, vol. 7, no. 6, pp. 1922 – 1935, 2014.

[143] M. Grana, I. Villaverde, J. Maldonado, and C. Hernandez, “Two lattice computing approaches for the unsupervised segmentation of hyperspectral images,” *Neuralcomputing*, vol. 72, pp. 2111–2120, 2009.

[144] E. Candes, J. Romberg, and T. Tao, “Robust uncertainty principles: Exact signal reconstruction from highly incomplete frequency information,” *IEEE Trans. Inf. Theory*, vol. 52, no. 2, pp. 489 – 509, 2006.

[145] D. Donoho, “Compressed sensing,” *IEEE Trans. Inf. Theory*, vol. 52, no. 4, pp. 1289 – 1306, 2006.

[146] A. Zare and P. Gader, “Sparsity promoting iterated constrained endmember detection for hyperspectral imagery,” *IEEE Geosci. Remote Sens. Lett.*, vol. 4, no. 3, pp. 446 – 450, 2007.

[147] ——, “Robust endmember detection using l1 norm factorization,” in *Proc. of IGARSS*, pp. 971 - 974, 2010.

[148] Y. Qian, S. Jia, J. Zhou, and A. Robles-Kelly, “Hyperspectra unmixing via l1/2 sparsity-constrained nonnegative matrix factorization,” *IEEE Trans. Geosci. Remote Sens.*, vol. 49, no. 11, pp. 4282 – 4297, 2011.

[149] M.-D. Iordache, J. Bioucas-Dias, and A. Plaza, “Sparse unmixing of hyperspectral data,” *IEEE Trans. Geosci. Remote Sens.*, vol. 49, no. 6, pp. 2014 – 2039, 2011.

[150] J. Greer, “Sparse demixing of hyperspectral images,” *IEEE Trans. Image Process.*, vol. 21, no. 1, pp. 219 – 228, 2012.

[151] M.-D. Iordache, J. Bioucas-Dias, and A. Plaza, “Collaborative sparse regression for hyperspectral unmixing,” *IEEE Trans. Geosci. Remote Sens.*, vol. 52, no. 1, pp. 341 – 354, 2014.

[152] B. A. Olshausen and D. Field, “Emergence of simple-cell receptive field properties by learning a sparse code for natural images,” *Nature*, vol. 381, pp. 607 – 609, 1996.

[153] A. S. Charles, B. A. Olshausen, and C. Rozell, “Learning sparse codes for hyperspectral imagery,” *IEEE J. Sel. Topics Signal Process.*, vol. 5, no. 5, pp. 963–978, 2011.

[154] A. Castrodad, Z. Xing, J. Greer, E. Bosch, L. Carin, and G. Sapiro, “Learning discriminative sparse representations for modeling, source separation, and mapping of hyperspectral imagery,” *IEEE Trans. Geosci. Remote Sens.*, vol. 49, no. 11, pp. 4263 – 4281, 2011.

[155] P. Hsu, “Feature extraction of hyperspectral images using wavelet and matching pursuit,” *ISPRS Journal of Photogrammetry and Remote Sensing*, vol. Volume: 62, Issue: 2, pp. 78–92, 2007.

[156] M.-D. Iordache, J. M. Bioucas-Dias, and A. Plaza, “Total variation spatial regularization for sparse hyperspectral unmixing,” *IEEE Trans. Geosci. Remote Sens.*, vol. 50, no. 11, pp. 4484 – 4502, 2012.

[157] J. S. Bhatt, M. V. Joshi, and M. S. Raval, “A data-driven stochastic approach for unmixing hyperspectral imagery,” *IEEE J. Sel. Topics Appl. Earth Observ.*, vol. 7, no. 6, pp. 1936–1946, 2014.

[158] S. Dowler and M. Andrews, “Abundance guided endmember selection: An algorithm for unmixing hyperspectral data,” *17th IEEE ICIP*, pp. 2649–2652, 2010.

[159] N. Dobigeon and et al., “Semi-supervised linear spectal unmixing using a hierarchical bayesian model for hyperspectral imagery,” *IEEE Trans. Signal Process.*, vol. 56, no. 7, pp. 2684–2695, 2008.

[160] A. Zymnis and et al., “Hyperspectral image unmixing via alternating projected subgradients,” in *Forty-first ACSSC*, pp. 1164-1168, 2007.

[161] N. Dobigeon and et al., “Joint bayesian endmember extraction and linear unmixing for hyperspectral imagery,” *IEEE Trans. Signal Process.*, vol. 57, no. 11, pp. 4355–4368, 2009.

[162] A. Plaza and C.-I. Chang, “Impact of initialization on design of endmember extraction algorithms,” *IEEE Trans. Geosci. Remote Sens.*, vol. 44, no. 11, pp. 3397–3407, 2006.

[163] S. Hemissi, I. R. Farah, K. S. Ettabaa, and B. Solaiman, “Multi-spectro-temporal analysis of hyperspectral imagery based on 3-d spectral modeling and multilinear algebra,” *IEEE Trans. Geosci. Remote Sens.*, vol. 51, no. 1, pp. 199–216, 2013.

[164] A. Plaza and C.-I. Chang, *High performance computing in remote sensing.* Taylor & Francis: Boca Raton, FL, 2007.

[165] A. Plaza, J. Plaza, A. Paz, and S. Sanchez, "Parallel hyperspectral image and signal processing," *IEEE Signal Process. Mag.*, vol. 28, no. 3, pp. 119–126, 2011.

[166] C. Gonzalez, D. Mozos, J. Resano, and A. Plaza, "Fpga implementation of the n-findr algorithm for remotely sensed hyperspectral image analysis," *IEEE Trans. Geosci. Remote Sens.*, vol. 50, no. 2, pp. 374 – 388, 2012.

[167] S. Sanchez, A. Paz, G. Martin, and A. Plaza, "Parallel unmixing of remotely sensed hyperspectral images on commodity graphics processing units," *Concurrency and Computation: Practice and Experience*, vol. 23, no. 13, pp. 1538 – 1557, 2011.

[168] J. Settle, "On the effect of variable endmember spectra in the linear mixture model," *IEEE Trans. Geosci. Remote Sens.*, vol. 44, pp. 389–396, 2006.

[169] D. Burazerovic, R. Heylen, B. Greens, S. Sterckx, and P. Scheunders, "Detecting the adjacency effect in hyperspectral imagery with spectral unmixing techniques," *IEEE J. Sel. Topics Signal Process.*, vol. 6, no. 3, pp. 1070–1078, 2013.

[170] S. Moussaoui, C. Carteret, C. Brie, and A. Mohammad-Djafari, "Bayesian analysis of spectral mixture data using markov chain monte carlo methods," *Chemometrics and Intelligent Laboratory Systems*, vol. 81, no. 2, pp. 137–148, 2006.

[171] N. Dobigeon, S. Moussaoui, J.-Y. Tourneret, and C. Carteret, "Bayesian separation of spectral sources under non-negativity and full additivity constraints," *Signal Processing*, vol. 89, no. 12, pp. 2657–2669, 2009.

[172] F. Schmidt, A. Schmidt, E. Treguier, M. Guiheneuf, S. Moussaoui, and N. Dobigeon, "Implementation strategies for hyperspectral unmixing using bayesian source separation," *IEEE Trans. Geosci. Remote Sens.*, vol. 48, no. 11, pp. 4000–4013, 2010.

[173] L. Zhang and et al., "A graph and simplex regularized nonnegative matrix factorization for hyperspectral unmixing," in *XXII International Society for Photogrammetry & Remote Sensing (ISPRS) Congress*, 2012.

[174] R. Zdunek, "Regularized nonnegative matrix factorization: Geometrical intepretation and application to spectral unmixing," *International Journal of Applied Mathematics and Computer Science*, vol. 24, no. 2, pp. 233–247, 2014.

[175] S. M. Kay, *Fundamentals of Statistical Signal Processing, Volume I: Estimation Theory.* Prentice Hall, 2001.

[176] S. Mei, M. He, Z. Wang, and D. Feng, “Mixture analysis by multichannel hopfield neural network,” *IEEE Geosci. Remote Sens. Lett.*, vol. 7, no. 3, pp. 455–459, 2010.

[177] D. Manolakis and G. Shaw, “Detection algorithms for hyperspectral imaging applications,” *IEEE Signal Process. Mag.*, vol. 19, no. 1, pp. 29 –43, Jan 2002.

[178] C.-I. Chang and S.-S. Chiang, “Anomaly detection and classfication for hyperspectral imagery,” *IEEE Transations on Geoscience and Remote Sensing*, vol. 40, no. 6, pp. 1314 – 1325, 2002.

[179] M. T. Eismann, J. Meola, A. Stocker, S. Beaven, and A. P. Schaum, “Airborne hyperspectral detection of small targets,” *Applied Optics*, vol. vol. 47, no. 28, p. F27 F45, Oct. 2008.

[180] G. H. Golub and C. F. van Loan, “An analysis of the total least squares problem,” *SIAM Journal on Numerical Analysis*, vol. 17, no. 6, pp. 883–893, 1980.

[181] E. Dowling and R. DeGroat, “The equivalence of the total least squares and minimum norm methods,” *IEEE Trans. Signal Process.*, vol. 39, no. 8, pp. 1891 –1892, 1991.

[182] R. D. Fierro, G. H. Golub, P. C. Hansen, and D. P. O’Leary, “Regularization by truncated total least squares,” *SIAM Journal on Scientific Computing*, vol. 18, no. 4, pp. 1223–1241, 1997.

[183] B. Shahraray and D. Anderson, “Optimal estimation of contour properties by cross-validated regularization,” *IEEE Transactions on Pattern Analysis and Machine Intelligence*, vol. 11, no. 6, pp. 600–610, 1989.

[184] [Online]. Available: http://dynamo.ecm.purdue.edu/biehl/MultiSpec

[185] R. Streit, M. Graham, and M. Walsh, “Tracking in hyper-spectral data,” *In Proc. of 5th International Conference on Information and Fusion*, vol. 2, pp. 852–859, 2002.

[186] J. Blackburn, M. Mendenhall, R. A., P. Shelnutt, N. Soliman, and J. Vasquez, "Feature aided tracking with hyperspectral imagery," *Proc. of SPIE*, vol. vol. 6699, pp. 66 990S–166 990S–12, 2007.

[187] A. Plaza, P. Martinez, R. Perez, and J. Plaza, "A new method for target detection in hyperspectral imagery based on extended morphological profiles," in *IEEE IGARSS Symposium*, 2003.

[188] G. Licciardi, A. Villa, M. Khan, and J. Chanussot, "Image fusion and spectral unmixing of hyperspectral images for spatial improvement of classification maps," in *IEEE IGARSS Symposium*, pp. 7290-7293, 2012.

[189] P. Masson and W. Pieczynski, "Sem algorithm and unsupervised statistical segmentation of satellite images," *IEEE Trans. Geosci. Remote Sens.*, vol. 31, no. 3, pp. 618–633, 1993.

[190] M. T. Eismann and R. C. Hardie, "Stochastic spectral unmixing with enhanced endmember class separation," *Applied Optics*, vol. 43, no. 36, pp. 6596–6608, 2004.

[191] P. J. Huber, "Robust estimation of a location parameter," *The Annals of Mathematical Statistics*, vol. 35, no. 1, pp. pp. 73–101, 1964.

[192] D. O. North, "An analysis of the factors which determine signal/noise discrimination in pulsed carrier systems," *Proc. IEEE*, vol. 51, no. 7, pp. 1016–1027, 1963.

[193] J. Chen and I. Reed, "A detection algorithm for optical targets in clutter," *IEEE Transactions on Aerospace and Electronic Systems*, vol. AES-23, no. 1, pp. 46–59, 1987.

[194] A. P. Schaum and A. D. Stocker, "Subpixel detection methods: spectral unmixing, correlation processing and when they are appropriate," in *Proc. of International Symposium on Spectral Sensing Research*, 1994.

[195] J. W. Boardman and F. A. Kruse, "Analysis of imaging spectrometer data using n-dimensional geometry and a mixture-tuned matched filtering approach," *IEEE Trans. Geosci. Remote Sens.*, vol. 49, no. 11, pp. 4138–4152, 2011.

[196] P. C. Mahalanobis, “On the generalised distance in statistics,” *In Proceedings of the National Institute of Sciences of India*, vol. 2, pp. 49–55, 1936.

[197] J. Kennedy and R. Eberhart, “Particle swarm optimization,” *In Proc. of IEEE International Conference on Neural Networks*, vol. 4, pp. 1942–1948, 1995.

[198] B. Zhang, X. Sun, L. Gao, and L. Yang, “Endmember extraction of hyperspectral remote sensing images based on the discrete particle swarm optimization algorithm,” *IEEE Trans. Geosci. Remote Sens.*, vol. 49, no. 11, pp. 4173–4176, 2011.

[199] H. Yang, Q. Du, and G. Chen, “Particle swarm optimization-based hyperspectral dimensionality reduction for urban land cover classification,” *IEEE J. Sel. Topics Appl. Earth Observ.*, vol. 5, no. 2, no. 2, pp. 544 –554, april 2012.

[200] R. Bro and S. Jong, “A fast non-negativity constrained least squares algorithm,” *Journal of Chemometrics*, vol. 11, pp. 393–401, 1997.

[201] [Online]. Available: http://aviris.jpl.nasa.gov/data/free_data.html

[202] C. L. Lawson and R. J. Hanson, *Solving Least Squares Problems.* SIAM, 1995.

[203] A. Plaza and J. Plaza, “Parallel implementation of linear and nonlinear spectral unmixing of remotely sensed hyperspectral images,” *Proc. SPIE 8183, High-Performance Computing in Remote Sensing, 81830D*, 2011.

[204] [Online]. Available: http://www.lx.it.pt/~bioucas/code/unmixing_overview.zip

[205] G. Swayze, R. N. Clark, S. J. Sutely, and A. Gallagher, “Ground-truthing aviris mineral mapping at cuprite, nevada,” *Summaries of the Third Annual JPL Airborne Geosciences Workshop*, vol. 1, pp. 47–49, 1992.

[206] G. Swayze, “The hydrothermal and structural history of the cuprite mining district, southwestern nevada: An integrated geological and gepphysical approach,” Ph.D. dissertation, University of Colorado, Boulder, 1997.

[207] A. Zare and K. Ho, “Endmember variability in hyperspectral analysis,” *IEEE Signal Process. Mag.*, vol. 31, no. 1, pp. 95 – 104, 2014.

[208] L. Alparone, B. Alazzi, S. Barnoti, A. Garzelli, F. Nenclni, and M. Selva, "Multispectral and panchromatic data fusion assessment without reference," *Photogrammetric Engineering and Remote Sensing*, vol. 74, no. 2, pp. 193 – 200, 2008.

[209] M. Khan, J. Chanussot, and L. Alparone, "Hyperspectral pansharpening using qnr optimization constraint," *Hyperspectral Image and Signal Processing: Evolution in Remote Sensing (WHISPERS)*, pp. 1–4, 2009.

[210] Z. Wang and A. C. Bovik, "A universal image quality index," *IEEE Signal Processing Letters*, vol. 9, no. 3, pp. 81–84, 2002.

[211] I. C. Trelea, "The particle swarm optimization algorithm: convergence analysis and parameter selection," *Information Processing Letters*, vol. 85, no. 6, pp. 317–325, 2003.

[212] L.-P. Zhang, H.-J. Yu, and S.-X. Hu, "Optimal choice of parameters for particle swarm optimization," *Journal of Zhejiang University Science A*, vol. 6, no. 6, pp. 528–534, 2005.

[213] M. E. H. Pedersen, "Good parameters for particle swarm optimization," Hvass Laboratory, Copenhagen, Denmark, Tech. Rep., 2010.

[214] D. Hamby, "A review of techniques for parameter sensitivity analysis of enviornment models," *Environmental Monitoring and Assessment*, vol. 32, no. 2, pp. 135–154, 1994.

[215] Q. Du and et al., "Variants of n-findr algorithm for endmember extraction," *Proc. SPIE*, vol. 7109, pp. 71 090G7–G8, 2008.

[216] A. Zare and P. Gader, "Hyperspectral band selection and endmember detection using sparsity promoting priors," *IEEE Geosci. Remote Sens. Lett.*, vol. 5, no. 2, pp. 256–260, 2008.

[217] [Online]. Available: http://www.ehu.es/computationalintelligence

[218] [Online]. Available: http://www.lx.it.pt/~bioucas/code.htm

[219] R. J. Radke, S. Andra, O. Al-Kofahi, and B. Roysam, "Image change detection algorithms: A systematic survey," *IEEE Trans. Image Process.*, vol. 14, no. 3, p. 294307, Mar. 2005.

[220] L. Bruzzone and S. B. Serpico, "An iterative technique for the detection of land-cover transitions in multitemporal remote-sensing images," *IEEE Trans. Geosci. Remote Sens.*, vol. 35, no. 4, pp. 858–867, 1997.

[221] H. M. Chen, P. K. Varshney, and M. K. Arora, "Performance of mututal information similarity measure for registration of multitemporal remote sensing images," *IEEE Trans. Geosci. Remote Sens.*, vol. 41, no. 11, pp. 2445–2454, 2003.

[222] A. Jalobeanu, A. M. Kim, S. C. Runyon, R. C. Olsen, and F. A. Kruse, "Uncertainty assessment and probabilistic change detection using terrestrial and airborne lidar," *Proc. of SPIE, Laser Radar Technology and Applications XIX; and Atmospheric Propagation XI*, vol. 9080, pp. 90 800S1–19, 2014.

[223] N. Oppelt and W. Mauser, "Three generations of the airborne imaging spectrometer avis: expectations, applications, results," *Proc. of SPIE, Optical Sensing II*, vol. 6189, pp. 618 911 – 9, 2006.

[224] S. Chaudhuri and K. Kotwal, *Hyperspectral Image Fusion.* Springer, 2013.

[225] [Online]. Available: http://alweb.ehu.es/ccwinto/index.php/Endmember_Induction_algorithms

[226] M. T. Eismann, J. Meola, A. Stocker, S. Beaven, and A. P. Schaum, "Hyperspectral change detection in the presence of diurnal and seasonal variations," *IEEE Trans. Geosci. Remote Sens.*, vol. 46, no. 1, pp. 237–249, 2008.

List of Publications

Book

- Jignesh S. Bhatt and Manjunath V. Joshi, "Regularization in Hyperspectral Unmixing", eBook in Spotlight Author Series on Digital Photography, *SPIE Press*, [Synopsis accepted, full-draft under review], 2015.

Journal

- Jignesh S. Bhatt, Manjunath V. Joshi, and Mehul S. Raval, "A data-driven stochastic approach for unmixing hyperspectral imagery", *IEEE Journal of Selected Topics in Applied Earth Observations and Remote Sensing*, vol. 7, no. 6, pp. 1936 - 1946, 2014.
- Jignesh S. Bhatt and Manjunath V. Joshi, "A use of multitemporal hyperspectral imagery for spectral unmixing," *IEEE Journal of Selected Topics in Applied Earth Observations and Remote Sensing*, [Manuscript submitted], 2015.

International Conference Proceedings

- Jignesh S. Bhatt, Manjunath V. Joshi, and Mehul S. Raval, "A regularization based method for spectral unmixing of imaging spectrometer data," *Proc. SPIE, Image and Signal Processing for Remote Sensing XVIII*, vol. 8537, pp. 85370J1-7, 2012.
- Jignesh S. Bhatt, Manjunath V. Joshi, and Mehul S. Raval, "A parametric statistical model over spectral space for the unmixing of imaging spectrometer data," *Proc. SPIE, Image and Signal Processing for Remote Sensing XVIII*, vol. 8537, pp. 85371J1-7, 2012.

Achievements

- **August 2012**

  International Student Travel Grant & Full Conference Registration fees waiver: **USD 1100.00 by SPIE (Europe)**

- **October 2012**

  Student Travel Grant: **INR 25000.00 by DA-IICT (India)**

- **since June 2013**

  Reviewer in IEEE Journal of Selected Topics in Applied Earth Observations and Remote Sensing (Invited by IEEE Geoscience & Remote Sensing Society).

- **September 2014**

  Invited Speaker in “National Seminar on Computer Vision and Image Processing (NaSCoVIP) 2014” by the IEEE Gujarat Section (Region - 10).

- **since March 2015**

  Reviewer in SPIE Journal of Applied Remote Sensing (Invited by SPIE Remote Sensing Society).